2D MoO_3 synthesis and its application in electronic devices

A thesis submitted in fulfilment of the requirements for the degree of Doctor of Philosophy

Fahmida Rahman

M. Phil, Bangladesh University of Engineering and Technology, Dhaka, Bangladesh

School of Engineering

College of Science, Engineering and Health

RMIT University

December 2018

Declaration

I certify that except where due acknowledgement has been made, the work is that of the author alone; the work has not been submitted previously, in whole or in part, to qualify for any other academic award; the content of the thesis is the result of work which has been carried out since the official commencement date of the approved research program; any editorial work, paid or unpaid, carried out by a third party is acknowledged; and, ethics procedures and guidelines have been followed. I acknowledge the support I have received for my research through the provision of an Australian Government Research Training Program Scholarship.

Fahmida Rahman

December 2018

Acknowledgements

My deepest gratitude and thanks for my supervisors Dr. Sivacarendran Balendhran, Assoc. Prof. Dr. Madhu Bhaskaran and Assoc. Prof. Dr. Sharath Sriram for their continuous encouragement, support, technical advice and valuable suggestions. Dr. Balendhran's exceptional motivational abilities, support and encouragement as a supervisor have been invaluable in helping me throughout my research. Dr. Madhu Bhaskaran, has been a constant source of support and guidance in all aspects of my Ph.D. candidature, and I am very grateful for all of her assistance. The supervisory support and guidelines of Dr. Sharath Sriram, have been valuable in realising the goals of this research.

I would like to thank Dr. Sumeet Walia for his wide-ranging support throughout my research program. I'd also like to take this opportunity to thank my colleagues, Dr. Taimur Ahmed, Mr. Aram Arash, Mr. Ataur Rahman, Mr. Rajour Tanyi Ako, Ms. Shruti Nirantar, Ms. Sruthi Kuriakose, Ms. Vaishnavi Krishnamurthi, and Mr. Mohammad Yousef O Taha. They have been wonderful sources of continuous support, motivation and encouragement over the past years at RMIT University.

None of this research could have been conducted without access to the world-class equipment and support of the expert staffs of the RMIT Microscopy and Microanalysis Facility (RMMF) and the Micro Nano Research Facility (MNRF). I take immense pleasure having worked in such facilities. I want to thank RMIT for giving me the opportunity to pursue my PhD and provide such a wonderful environment to carry out this research.

Finally, I would like to thank my two wonderful kids, who were always my source of inspiration, my husband for being extremely supportive, patient and understanding. I am also grateful to my parents for their endless love and support.

Table of Contents

List of Figures

List of Tables

List of Abbreviations and Acronyms

2D	Two dimensional
MoO_3	Molybdenum Oxide
MoS_2	Molybdenum Sulphide
FETs	Field effect transistors
CVD	Chemical Vapour Deposition
PDMS	Polydimethylsiloxane
KOH	Potassium Hydroxide
H_2SO_4	Sulphuric acid
AFM	Atomic Force Microscopy
XRD	X-ray diffractometer
SEM	Scanning Electron Microscopy
TEM	Transmission Electron Microscopy
HRTEM	High resolution transmission electron microscopy
XPS	X-ray Photoemission Spectroscopy
SAED	Selected area electron diffraction
EDS	Energy Dispersive X-ray Spectroscopy

FFT	Fast Fourier Transform
HRS	High Resistive State
LRS	Low Resistive State
SCLC	Space Charge Limited Conduction
SiO_2	Silicon Dioxide
Si	Silicon
CO	Carbon Monoxide
NO_2	Nitrogen Oxide
H_2	Hydrogen
H_2S	Hydrogen Sulphide
CMOS	Complementary metal oxide semiconductor

List of Symbols

k	Dielectric constant
C	Capacitance
l	Length
w	Width
V_{GS}	Gate-Source Voltage
I_{GS}	Gate-Source Current
V_{DS}	Drain-source Voltage
I-V	Current-Voltage

Abstract

Two-dimensional (2D) materials have significant technological importance due to their exceptional electronic and mechanical properties, which stem from the quantum confinement of charge carriers along a single plane. Their thin atomic nature and large surface-to-volume ratio offer an opportunity to tailor their properties, making them suitable candidates for next-generation electronic devices.

Molybdenum trioxide (MoO_3) is a wide bandgap and high dielectric material that can be obtained in 2D structure. The bandgap of the material can be readily tuned using ion intercalation method. Consequently, carrier mobility can be enhanced by increasing the charge carriers' density near the Fermi level. As such, reliable production of few atoms thick 2D material is essential for translating their properties into electronic applications. However, obtaining the desired thickness of uniform 2D MoO_3 crystal is challenging, as the existing exfoliation technique do not produce crystals of uniform thickness efficiently. A new chemical route has been developed to thin down bulk crystals of MoO_3 in order to obtain them in 2D form. The viability and reliability of the etching process has been established via detail characterisation of the material pre- and post-etching. The electrical characterisation of the 2D MoO_3 crystals based field effect transistors show high switching ratios.

Non-volatile resistive memory devices are theorised to be the most promising pathway towards analogue memory and neuromorphic computing. Metal oxides are widely used as channel material in such memory devices. High dielectric constant and thermal stability of

MoO_3 renders it ideal for resistive memory applications as high dielectric nature suppresses the undesirable parasitic effects during resistive switching performance. The reversible and non-volatile resistive switching behaviour of planar MoO_3 crystals has been investigated. The room temperature memory retention shows high on/off ratio of $>10^3$ for 10^4 s duration and endurance of > 6,000 cycles, and low power consumption. This study demonstrates the viability of MoO_3 as a resistive memory element and paves the way for future 2D resistive memory technologies.

Furthermore, conductometric gas sensors have been developed based on the 2D crystals of non-stoichiometric MoO_3. Thermodynamically stable MoO_3 shows excellent electron affinity towards various gaseous elements. In addition, 2D structure endows them with an ultrahigh surface area that contains an extremely large proportion of surface atoms. These surface atoms serve as active sites to effectively react with gas molecules for gas sensing applications. Detail characterisations of the sensors show excellent selectivity and high sensitivity towards toxic and health hazard gases such as, H_2S and NO_2. The cyclic repeatability shows a negligible variation in sensitivity that establishes the viability of a high responsive gas sensor based on 2D MoO_3.

Hence, thermally stable and high dielectric 2D MoO_3 has the potential to offer a new-generation of nano-electronic applications with excellent performance.

Chapter 1 : INTRODUCTION

1.1 Motivation

In the current digital era, smart devices demand efficient and high-density electronics. Existing silicon-based technology is unable to provide such efficiency, as it has reached its theoretical and physical limitations.[1] Consequently, new materials compatible with the existing silicon-based technology in the field of electronics are being investigated as an alternative. The isolation of the graphene monolayer in 2004 by the mechanical exfoliation of bulk graphite unfolded a new era in the field of electronics, as well as in the realm of two-dimensional (2D) materials.[2-3] Since then, it has been the most investigated 2D material due to its excellent physical and electronic properties.[4-9] The unique electronic properties of 2D materials compared to their bulk counterparts arise from the quantum confinement of charge carriers, as the bulk materials are scaled down to monolayers.[10-11] Additionaly, the surface effect of the single/few atomic layer thicknesses of 2D materials favours the fabrication of flexible electronic/optoelectronic devices.[12] However, graphene lacks an energy bandgap, which has hindered its widespread deployment in nano-electronic applications.[13] This has initiated extensive research to explore other 2D materials, such as molybdenum dichalcogenides and oxide, hexagonal boron-nitride (h-BN), black phosphorous or phosphorene. Among them, molybdenum trioxide (MoO_3) is a potential transition metal oxide abundant in nature. MoO_3 has a wide band gap (~3.2 eV), a high dielectric constant (k) and is a thermodynamically stable, layered semiconducting material. It can be obtained in multiple stable states based on the oxidation level in the crystals. It shows enhanced

electronic transport properties, as its bandgap can be easily tuned via the manipulation of its stoichiometry.[14] Ion intercalation is a method to tune the bandgap of the material by introducing oxygen vacancies in the crystal lattice, which results in increasing charge carriers near the Fermi level.[11, 15] In 2D form, a large number of atoms is exposed due to the large area-to-volume ratio, which enhances the reaction sites.[16-17] As a result, 2D MoO_3 has been used as a functional material in a wide range of promising nano-electronic applications, such as in photochromic devices, field effect transistors (FETs),[11, 14, 18] resistive memories[19] and gas sensors.[20-21]

The reliable production of atomically thin and uniform 2D crystals is essential for translating their electronic properties into applications.[22-23] Two-dimensional MoO_3 crystals can be achieved via both top-down and bottom-up synthesis methods. The existing top down exfoliation techniques of obtaining 2D crystals of MoO_3 do not produce pure 2D crystals simultaneously and efficiently.[24] Mechanical exfoliation is a top-down method, and it is a simple and easy way to obtain pure crystals for scientific research. However, the randomness in the lateral size and thickness of the exfoliated crystals makes it challenging to obtain single crystals with required thicknesses.[3, 24] To manage this issue, post-deposition wet chemical etching of the multi-layered crystals is a promising route towards the sustainable production of 2D crystals with desired thicknesses. Several reports on the chemical etching of MoS_2 crystals show the viability of the method, but there is no report on the controllable etching of MoO_3 crystals.[24-28] As such, a new route of controllable chemical etching to obtain 2D MoO_3 crystals would add new knowledge to the field. Furthermore, electronic charaterisation of such 2D crystals via field effect transistors (FETs) would be benefit the field of nano-electronics.

The potential production of MoO_3 with large area coverage in the millimetre range and their

viable electronic applications are crucial areas of research that requires investigation.. Chemical vapour deposition (CVD) has been found to be a valuable bottom-up synthesis process that provides the scalable and controllable growth of high quality and large-area 2D crystals of graphene and molybdenum dichalcogenides.[29-33] Despite the successful and controllable growth of large-area dichalcogenides, the synthesis of MoO_3 via CVD has received little attention.[34-35] As such, developing a viable synthesis technique to grow large-area MoO_3 would be valuable to the study in electronic applications and areas such as resistive memory. Reversible resistive memories or memristors are potential candidates for future storage and neuromorphic computing technologies. They possess excellent characteristics, including scalability, multiple switching states, fast switching speeds, high cyclic endurance as well as CMOS compatibility.[36-37] A large variety of metal oxides have been widely used as channel material in resistive memory applications that shows non-volatile memory performances.[38-39] However, they are still in their infancy and do not meet the criteria for the real data storage technology in modern electronics.[40-41] Thus, investigation of novel electronically active 2D materials as active switching layers for high-performance resistive memory devices is required. However, 2D crystals are rarely studied for resistive memory applications, due to lack of large area synthesis technique.[42] MoO_3 is a versatile metal oxide with high dielectric value, that can be obtained in various oxidation states via CVD synthesis technique and has the potential for resistive memory applications.[43] Furthermore, investigation in memory characteristics of such MoO_3 crystals would enrich the field of planar memory.

In modern society, continuous development of industry and agriculture requires continuous and ever-increasing production that results in the emission of toxic and greenhouse gases in the environment. Thus, detecting traces of toxic gases and monitoring air quality are important to environmental safety and the quality of human life. Metal oxides are often used

as sensitive layers in gas sensing technologies.[44] However, most metal-oxide based gas sensors work at high temperature accompanied with increased power consumption.[45-46] Hence, incorporation of 2D material in gas sensing devices are gaining attention to study as an alternative, as atomically thin 2D layers of sensing material allow achieving higher sensitivity and faster response. The large surface-to-volume ratio of 2D crystals provides a significant number of surface atoms as reaction sites, which cannot be achieved in their bulk counterparts and is favourable for gas-sensing applications.[13,17, 47] Graphene and graphene oxide have been widely employed in the gas-sensing field due to a high specific surface area, fast electron transport and high conductivity.[17, 47] Furthermore, a variety of 2D dichalcogenides also have shown superior sensing capability.[48] Though MoO_3 thin films shows excellent gas-sensing properties, as a sensor material 2D MoO_3 has not been studied extensively.[49-52] The existence of oxygen vacancy in MoO_3 provides a large charge carrier concentrations and referred to as non-stoichiometric MoO_3/(MoO_{3-x}) which further enhances the electronic properties of the material. Thus, research on the gas-sensing performance of non-stoichiometric 2D MoO_3 crystals would enable highly selective and high-performance sensing applications in comparison to the existing thin film-based sensors.

Given the research gaps outlined above, the primary aims of this research are as follows,

a) To investigate a new synthesis technique to obtain 2D MoO_3 crystals and characterise their electronic performance in FETs,

b) To investigate the resistive memory behaviour in large-area MoO_3 crystals and

c) To investigate the sensing performance of highly toxic NO_2 and H_2S gases in non-stoichiometric 2D α-MoO_3-based devices.

1.2 Objectives

The research work in this PhD dissertation can be briefly classified under the following objectives:

(a) To develop an easily deployable chemical etching route in order to obtain pure 2D MoO_3 crystals and to study their electrical performance as a channel material in FETs,

(b) To characterise the resistive memory behaviour in large area MoO_3 crystals.

(c) To study the gas sensing characteristics of non-stoichiometric 2D α-MoO_3 based sensors.

1.3 Original Contributions

In this research, the following novel methods, which represent original contributions to the field, will be adopted:

1.3.1 Investigation of a novel synthesis technique to obtain 2D crystals of MoO_3

A novel chemical thinning route is developed in order to obtain 2D α-MoO_3 crystals of desired thicknesses controllably and reliably. Furthermore, the thinned down 2D crystals is employed in FETs applications to characterise the electrical performance. Full details of the method to achieve this objective of the research will be described in chapter 3.

1.3.2 Investigation of resistive memory behavior in large area MoO_3

The reversible resistive switching behavior of large area MoO_3 is characterised via cyclic repeatability, data retention and cyclic endurance capabilities. Detail characterisation on the pristine and electroformed cells is studied to understand switching mechanism in the memory cells. Full details of the methods used to achieve this objective and the experimental results will be described in Chapter 4.

1.3.3 Investigation of gas sensing characteristics of non-stoichiometric 2D α-MoO_3

This section of the PhD research is focused on gas sensing characterisation of non-stoichiometric 2D α-MoO_3. It is demonstrated that gas sensors based on non-stoichiometric 2D α-MoO_3 has the potential to offer high sensing performance. The successful application of the concept will be explained in detail in Chapter 5.

1.4 Thesis organisation

In Chapter 2, a comprehensive literature review regarding the synthesis process and applications based on 2D MoO_3 is presented. This chapter describes the different techniques that are available to obtain bulk MoO_3 crystals in a 2D structure. Furthermore, a detailed perspective on the existing memory and gas sensing applications based on 2D MoO_3 is presented.

In Chapter 3, a controllable and repeatable chemical thinning process of obtaining 2D MoO_3 will be discussed and incorporation of such 2D crystals into FETs will be studied. A thorough

characterisation of the pre- and post-etching crystals will be performed in order to establish the viability of the etching process.

To understand the non-volatile memory behaviour of 2D MoO_3 crystals, a detail characterisation will be performed. The reversible resistive behaviour of the material along with details of the switching mechanism will be presented in Chapter 4.

In Chapter 5, gas-sensing characterisation of non-stoichiometric 2D MoO_3 will be presented. A detail methodology to perform the characterisation and gas sensing mechanism will be discussed.

Finally, Chapter 6 will discuss the overall conclusions of this PhD research and possible future directions.

1.5 Publications

1.5.1 First author

- **F. Rahman**, T. Ahmed, S. Walia, E. Mayes, S. Sriram, M. Bhaskaran and S. Balendhran,“ Reversible resistive switching behaviour in layered MoO_x”, Nanoscale, 2018, 10, 19711 .

- **F. Rahman**, T. Ahmed, S. Walia, E. Mayes, S. Sriram, M. Bhaskaran and S. Balendhran “Two-dimensional MoO_3 via a top-down chemical thinning route”, 2D Materials, 2017, 4, 035008.

1.5.2 Co-author

- A. Arash, T. Ahmed, A. G. Rajan, S. Walia, **F. Rahman**, A. Mazumder, R. Ramanathan, S. Sriram, M. Bhaskaran, E. H. Mayes, M. Strano and S. Balendhran "Large-area synthesis of two-dimensional MoO_{3-x} for enhanced optoelectronic applications", 2D Materials, 2019.

- S. Walia, S. Balendhran, T. Ahmed, M. Singh, C. El-Badawi, M. D. Brennan, P. Weerathunge, Md. N. Karim, **F. Rahman**, A. Rassell, J. Duckworth, R. Ramanathan, G. E. Collis, C. J. Lobo, M. Toth, J. C. Kotsakidis, B. Weber, M. Fuhrer, J. M. Dominguez-Vera, M. J. S. Spencer, I. Aharonovich, S. Sriram, M. Bhaskaran, and V. Bansal "Ambient protection of few-layer black phosphorus via sequestration of reactive oxygen species", Advanced materials, 2017, 29, 1700152.

1.5.3 In progress

- **F. Rahman,** Md. A. Rahman, S. Walia, S. Sriram, M. Bhaskaran and S. Balendhran, "Dual gas sensing characteristics of non-stoichiometric 2D α-MoO_3**."**

1.6 References

1. Kingon, A. I., *et a*l., Alternative dielectrics to silicon dioxide for memory and logic devices. Nature **2000,** 406 (6799), 1032-1038.

2. Novoselov, K. S., *et al.,* Two-dimensional atomic crystals. Proceedings of the National Academy of Sciences of the United States of America **2005,** 102 (30), 10451-10453.

3. Whitener Jr, K. E.; Sheehan, P. E., Graphene synthesis. Diam. Relat. Mater. **2014,** 46, 25-34.

4. Novoselov, K. S., *et al*., Two-dimensional gas of massless Dirac fermions in graphene. Nature **2005,** 438, 197.

5. Bonaccorso, F., *et al*., Graphene photonics and optoelectronics. Nature Photonics **2010,** 4, 611.

6. Yanwu, Z., *et al*., Graphene and graphene oxide: synthesis, properties, and applications. Adv. Mater. **2010,** 22 (35), 3906-3924.

7. Schwierz, F., Graphene transistors. Nat. Nanotechnol. **2010,** 5, 487.

8. Kim, K. S., *et al*., Large-scale pattern growth of graphene films for stretchable transparent electrodes. Nature **2009,** 457, 706.

9. Castro Neto, A. H., *et al.*, The electronic properties of graphene. Rev. Mod. Phys. **2009,** 81 (1), 109-162.

10. Bao, W., *et al*., High mobility ambipolar MoS_2 field-effect transistors: Substrate and dielectric effects. Appl. Phys. Lett. **2013,** 102 (4).

11. Alsaif, M. M. Y. A., *et al*., High-performance field effect transistors using electronic inks of 2D molybdenum oxide nanoflakes. Adv. Funct. Mater. **2016,** 26, 91-100.

12. Pu, J., *et al*., Flexible and stretchable thin-film transistors based on molybdenum disulphide. Phys. Chem. Chem. Phys. **2014,** 16 (29), 14996-5006.

13. Novoselov, K. S., *et al*., Electric field effect in atomically thin carbon films. Science **2004,** 306 (5696), 666.

14. Balendhran, S., *et al*., Enhanced charge carrier mobility in two-dimensional high dielectric molybdenum oxide. Adv. Mater. **2013,** 25 (1), 109-14.

15. Ou, J. Z., *et al*., In situ Raman spectroscopy of H_2 gas interaction with layered MoO_3. J. Phys. Chem. C **2011,** 115 (21), 10757-10763.

16. Choi, S.-J.; Kim, I.-D., Recent developments in 2D nanomaterials for chemiresistive-type gas sensors. Electron. Mater. Lett. **2018,** 14 (3), 221-260.

17. Yang, S., *et al*., Gas sensing in 2D materials. Applied Physics Reviews **2017,** 4 (2), 021304.

18. Balendhran, S., *et al*., Field effect biosensing platform based on 2D α-MoO_3. ACS Nano **2013,** 7 (11), 9753-9760.

19. Tan, Z.-H., *et al*., One-dimensional memristive device based on MoO_3 nanobelt. Appl. Phys. Lett. **2015,** 106 (2), 023503.

20. Alsaif, M. M. Y. A., *et al*., Two dimensional α-MoO_3 nanoflakes obtained using solvent-assisted grinding and sonication method: Application for H_2 gas sensing. Sensors and Actuators B: Chemical **2014,** 192, 196-204.

21. Zhang, L., *et al*., Self-assembly gridding α-MoO_3 nanobelts for highly toxic H_2S gas sensors. Sens. Actuator B-Chem. **2016,** 237, 350-357.

22. Wang, Q. H., *et al*., Electronics and optoelectronics of two-dimensional transition metal dichalcogenides. Nat. Nanotechnol. **2012,** 7, 699.

23. Balendhran, S., *et al*., Two-dimensional molybdenum trioxide and dichalcogenides. Adv. Funct. Mater. **2013,** 23 (32), 3952-3970.

24. Kalantar-zadeh, K., *et al*., Synthesis of nanometre-thick MoO_3 sheets. Nanoscale **2010,** 2 (3), 429-433.

25. Lu, X., *et al*., Layer-by-layer thinning of MoS_2 by thermal annealing. Nanoscale **2013,** 5 (19), 8904-8908.

26. Amara, K. K., *et al*., Wet chemical thinning of molybdenum disulfide down to its monolayer. APL Mater. **2014,** 2 (9).

27. Castellanos-Gomez, A., *et al*., Laser-thinning of MoS_2: On demand generation of a single-layer semiconductor. Nano Lett. **2012,** 12 (6), 3187-3192.

28. Huang, Y., *et al*., An innovative way of etching MoS_2: Characterization and mechanistic investigation. Nano Res. **2013,** 6 (3), 200-207.

29. Zhang, Y., *et al*., Review of chemical vapor deposition of graphene and related applications. Acc. Chem. Res. **2013,** 46 (10), 2329-2339.

30. Liu, H. F., *et al*., CVD growth of MoS_2-based two-dimensional materials. Chem. Vap. Deposition **2015,** 21 (10-11-12), 241-259.

31. Zheng, B.; Chen, Y., Controllable growth of monolayer MoS_2 and $MoSe_2$ crystals using three-temperature-zone furnace. IOP Conf Ser Mater Sci Eng **2017,** 274, 012085.

32. Jeon, J., *et al*., Layer-controlled CVD growth of large-area two-dimensional MoS_2 films. Nanoscale **2015,** 7 (5), 1688-1695.

33. Wang, T., *et al*., Synthesis of MoS_2 and MoO_3 hierarchical nanostructures using a single-source molecular precursor. Powder Technology **2014,** 253, 347-351.

34. Ivanova, T., *et al*., Structure and optical properties of CVD molybdenum oxide films for electrochromic application. J. Solid State Electr. **2002,** 7 (1), 21-24.

35. Hyeong, U. K., *et al*., Highly uniform wafer-scale synthesis of α -MoO_3 by plasma enhanced chemical vapor deposition. Nanotechnology **2017,** 28 (17), 175601.

36. M. Wang, S. C., C. Pan, C. Wang, X. Lian, Y. Zhuo, K. Xu, T. Cao, X. Pan, B. Wang, S. J. Liang, J. J. Yang, P. Wang, and F. Miao, Robust memristors based on layered two-dimensional materials. Nat. Electron **2018,** 1 (2), 130-136.

37. Gwang Hyuk, S., *et al.*, Multilevel resistive switching nonvolatile memory based on MoS 2 nanosheet-embedded graphene oxide. 2D Mater. **2016,** 3 (3), 034002.

38. Mohammad, B., *et al.*, State of the art of metal oxide memristor devices. Nanotechnol. Rev. **2016,** 5 (3), 311-329.

39. Sawa, A., Resistive switching in transition metal oxides. Mater. Today **2008,** 11 (6), 28-36.

40. Chaoliang Tan, Z. L., Wei Huang and Hua Zhang, Non-volatile resistive memory devices based on solution-processed ultrathin two-dimensional nanomaterials. Chem Soc Rev **2015,** 44.

41. Scott, J. C., Is There an Immortal Memory? Science **2004,** 304 (5667), 62-63.

42. Cheng, P., *et al*., Memristive behavior and ideal memristor of 1T phase MoS_2 nanosheets. Nano Lett. **2016,** 16 (1), 572-576.

43. de Castro, I. A., *et al*., Molybdenum oxides – from fundamentals to functionality. Adv. Mater. **2017,** 29 (40), 1701619.

44. Zhou, Y., *et al*., UV assisted ultrasensitive trace NO_2 gas sensing based on few-layer MoS2 nanosheet–ZnO nanowire heterojunctions at room temperature. Journal of Materials Chemistry A **2018,** 6 (22), 10286-10296.

45. Sukunta, J., *et al*., WO_3 nanotubes−SnO_2 nanoparticles heterointerfaces for ultrasensitive and selective NO 2 detections. Applied Surface Science **2018,** 458, 319-332.

46. Dey, A., Semiconductor metal oxide gas sensors: A review. Materials Science and Engineering: B **2018,** 229, 206-217.

47. Neri, G., Thin 2D: The New Dimensionality in Gas Sensing. Chemosensors **2017,** 5 (3), 21.

48. Ko, K. Y., *et al*., Improvement of gas-sensing performance of large-area tungsten disulfide nanosheets by surface functionalization. ACS Nano **2016,** 10 (10), 9287-9296.

49. Yang, Y. A., *et al*., Microstructures of electrochromic MoO_3 thin films colored by injection of different cations. J. Phys. Chem. B **1998,** 102 (47), 9392-9396.

50. Ajito, K., *et al*., Study of the photochromic properties of amorphous MoO_3 films using Raman microscopy. J. Phys. Chem. **1995,** 99 (44), 16383-16388.

51. Arnoldussen, T. C., Electrochromism and photochromism in MoO_3 films. J. Electrochem. Soc. **1976,** 123 (4), 527-531.

52. Ji, F., *et al*., 2D-MoO_3 nanosheets for superior gas sensors. Nanoscale **2016,** 8 (16), 8696-703.

Chapter 2 : LITERATURE REVIEW

2.1 Introduction

As modern technologies continue to evolve in a moderately exponential and self-enhancing manner, existing technologies for the current computing systems are approaching their physical limits. These highly evolved technologies demand electronic devices that are not only simple and infinitesimal in size but also increasingly capable. Two-dimensional materials are substances with a thickness of a few nanometres or less. As they are only one or several atoms thick, they have the potential to play a significant role in the future of nano-electronics and the assembly of novel ultrathin devices. Since the discovery of graphene, it has been the most popular and vastly used 2D material due to its ultrahigh carrier mobility (> 200,000 $cm^2V^{-1}s^{-1}$), large mechanical strength (55 N/m), room temperature quantum Hall effect and tuneable optical absorption.[1-2] As such, progress in graphene research has had an enormous effect on the field of electronics.[3-6] However, the lacking intrinsic bandgap in graphene has led to the further investigation of other 2D materials, such as metal dichalcogenides and layered metal oxides.[7] The properties of these 2D materials are widely studied, as they show both exceptional electrical and thermal conductivity, and excellent flexibility and stretchability.[8-16] The 2D material family encompasses a large variety of materials with versatile electronic and physical properties including insulating to semimetallic behaviour. As such, 2D nanostructures are anticipated to have an important influence on a huge diversity of electronics and optoelectronic applications.[17-21]

2.2 2D MoO_3

Molybdenum oxide (MoO_3), a member of the 2D materials family, is an *n*-type material with a wide bandgap (~3 eV) and high dielectric (*k*) value. Its high dielectric value makes it appropriate for electronic applications, as it reduces Coulomb scattering. MoO_3 shows enhanced electronic properties, where the band structure of MoO_3 can be tuned via ionic intercalation, which enables the engineering of its properties and potentially renders it semi-metallic to insulating on demand.[21] Usually, ion intercalation changes the stoichiometry of the material by introducing oxygen vacancies, thus, enhancing the charge carrier concentration as a result of the increasing density of states at the Fermi level.[22] Such aspects of 2D MoO_3 makes it promising in a variety of potential applications such as field effect transistors,[21] bio and gas-sensors,[23-24] light emitting diodes,[25] supercapacitor electrodes,[26] flexible photodetectors,[27] and memristors.[28]

MoO_3 has two major crystal phases: thermodynamically stable α-MoO_3 and metastable β-MoO_3 (Figure 2.1).[29-30] Among them, orthorhombic α-MoO_3 possesses the stratified layered crystal phase of molybdenum trioxide, and α-MoO_3 possesses the double layers of MoO_6, stacked together through weak van der Waals forces along the vertical direction. Each double layer consists of edge-sharing MoO_6 octahedra along the {0 0 1} direction and corner-sharing rows along the {1 0 0} direction.[31-32] This layered and stratified configuration allows for the easy exfoliation of layers from the parent crystal. In addition, the weak van der Waals attraction facilitates layered growth of the material from the bottom.

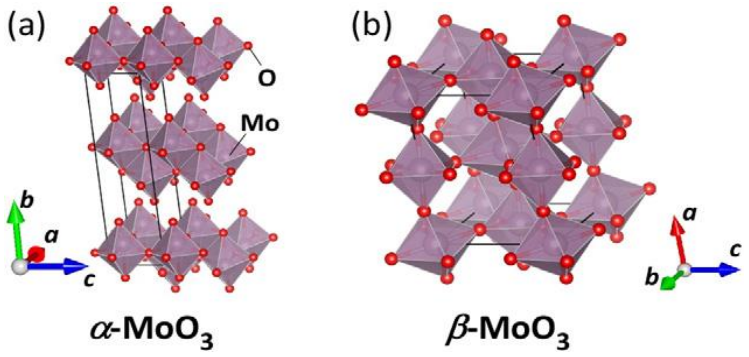

Figure 2.1 Schematic illustration of crystal structures of (a) orthorhombic α-MoO_3, and (b) monoclinic β-MoO_3. The gray and red balls correspond to Mo and O atoms, respectively. The black lines show each unit cell.[30]

Furthermore, oxygen deficient intermediate state of Molybdenum Oxide can be obtained which is in between MoO_3 and MoO_2 (i.e., $Mo_{18}O_{52}$, $Mo_{17}O_{47}$, Mo_9O_{26}, Mo_8O_{23}, Mo_5O_{14}, and Mo_4O_{11}). Figure 2.2 represents some of the sub-stoichiometric crystal structure.[27] The oxygen vacancies induce gap states, resulting in bandgap engineering and enhancing the charge carrier concentration near the gap states.[21,34] Hence, these oxygen vacancies play an important role in modifying the electronic and optical properties of the material.[34] There are theoretical and experimental results demonstrating that oxygen vacancies play an important role in modifying the electronic and optical properties of the oxide.[35] Hydrogen intercalation is one of the most common adopted procedures for producing the oxygen vacancies in the material.[21,36] Alkali metals such as lithium (Li), sodium (Na), potassium (K) has been used as intercalants for the manipulation of the stoichiometry of the material.[37-38] Other than this, thermal treatment and ultraviolet irradiation can be adopted to change the stoichiometry of the material.[34,39]

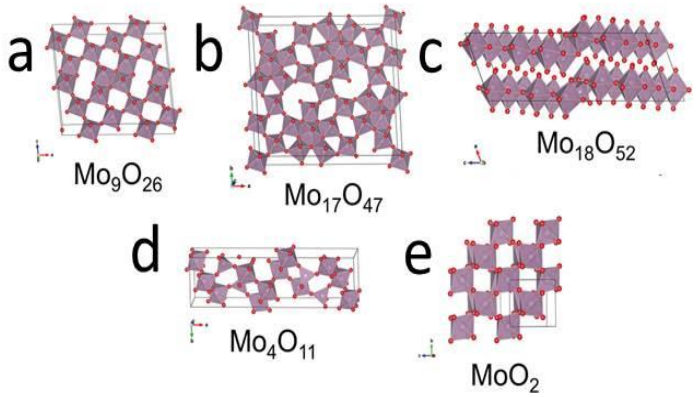

Figure 2.2 Crystal structures of sub-stoichiometric molybdenum oxides (a–e) as indicated in each image and showing their single unit cells.[27]

2.3. Synthesis of 2D MoO_3

The development of facile, feasible and reliable methods for the preparation of 2D materials is of great importance for the exploration of their properties and translating their new electronic and optical properties into applications. As such, considerable efforts have been devoted to the synthesis of a large variety of 2D materials. Generally, all these methods can be classified into two categories: (i) top-down approaches, including mechanical exfoliation and liquid-phase exfoliation, and (ii) bottom-up approaches, including CVD. The top-down method relies on the exfoliation of layered bulk crystals into single or few-layer nano-sheets, in which various driving forces are used to break the weak van der Waals interaction between the stacked layers. However, the lack of uniformity in the exfoliated crystal's size and shape appears an important issue that has motivated development beyond the fundamental studies.

2.3.1 Mechanical exfoliation

Mechanical exfoliation is a simple and popular technique to obtain single/few layers of MoO_3 by cleaving bulk crystals. The adjacent double layers of MoO_6 octahedra are linked together only by weak van der Waals forces forming the layered structure of MoO_3. The weak van der Waals forces between sheets can be overcome by applying a sufficient mechanical force perpendicular to the planar direction using adhesive tape. Eventually, a single atomic layer can be isolated from the bulk and deposited onto a substrate for characterisation. Novoselov *et al*. first used this method to peel off graphene layers from graphite.[20] Since then it has been the mostly used technique to obtain 2D crystals (Figure 2.3a–d).[8] This method is highly remarkable, as it offers a simple strategy for preparing 2D mono-atomic layers and it enables the fundamental study of the material.[40-42] As such, most reported data and theory on the fundamental physics and devices of 2D materials have largely relied on the mechanical exfoliation method. Indeed, this produces high quality atomically thin and pristine crystals, but it is not scalable and does not allow for the controllable production of crystals with uniform thicknesses and size (Figure 2.3 e,f).[32]

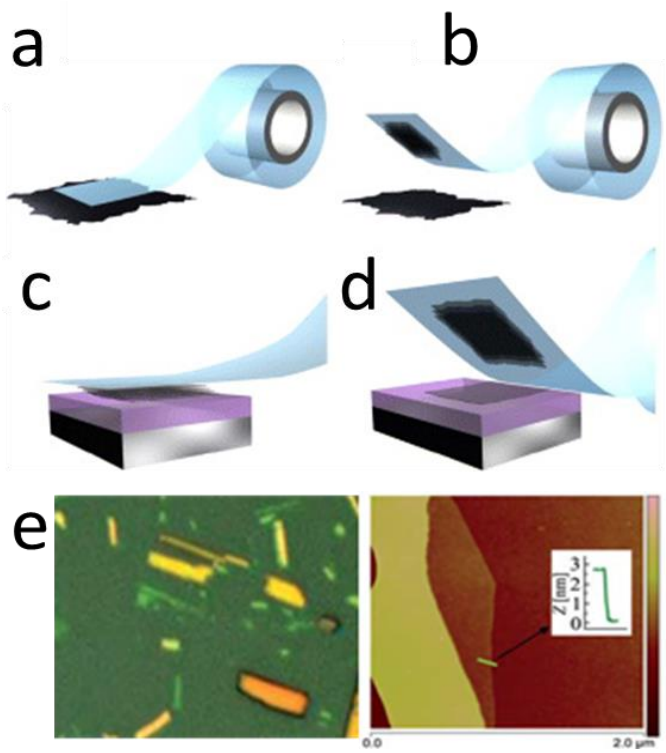

Figure 2.3 Micromechanical exfoliation of 2D crystals. (a) Adhesive tape is pressed against a 2D crystal so that the top few layers are attached to the tape (b). (c) The tape with crystals of layered material is pressed against a surface of choice. (d) Upon peeling off, the bottom layer is left on the substrate.[8] (e) Typical optical image and atomic force microscopy (AFM) thickness profiles (inset) of mechanically exfoliated MoO_3 crystals.[32]

2.3.2 Liquid phase exfoliation

Liquid-phase exfoliation is a high yield method to produce 2D crystals; this involves the exfoliation of the layers using the intercalation method.[43-44] Different chemical elements are intercalated between the gaps of the layers, and they weaken the van der Waals bonding between the layers. The MoO_3 crystals suspended in a suitable solvent are sonicated using a high-energy probe sonicator to create synergy with the surface energy of MoO_3. The sonication process applies shear force on the surface of the crystals, which delaminates and exfoliates the layers of the crystals.,[23,45] Subsequently, this suspension of exfoliated crystals is centrifuged to separate the lighter monolayers from their bulk counterparts. Figure 2.4a–c

illustrates the steps in a liquid exfoliation process.[7] Dispersions of layered compounds in a liquid solution can be deposited over large areas, where the size and thickness of the material are comparatively controllable. Though it is a high-yield technique, the properties of the resulting exfoliated liquid differ from those of its bulk, as the solvent used for exfoliation may leave residue. Figure 2.4d–e shows the AFM image and transmission electron microscopy (TEM) images of liquid phase exfoliated 2D MoO_3 crystals.[24]

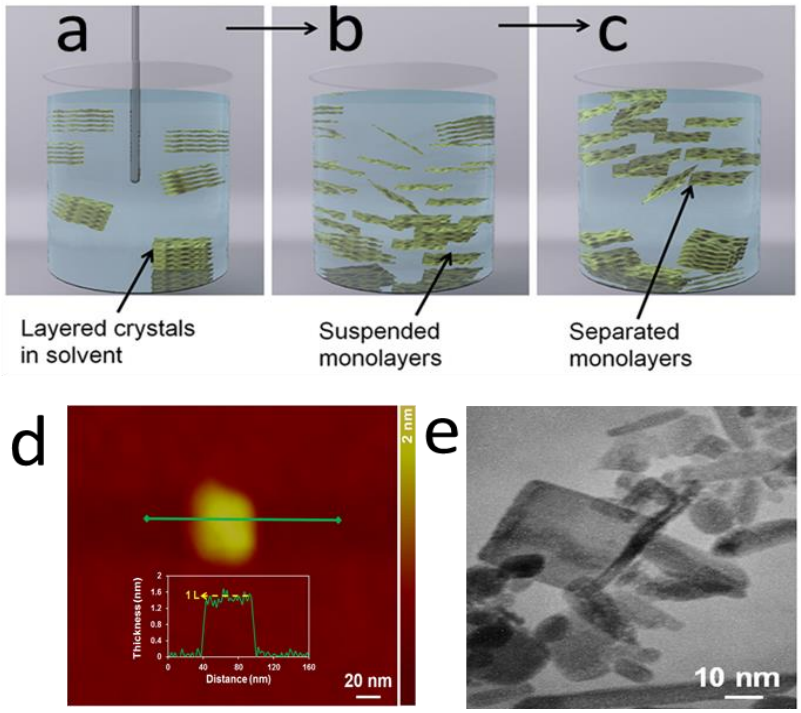

Figure 2.4 Liquid exfoliation processes. (a) Probe sonication (b) Centrifugation (c) Separation of monolayers.[7] (d) AFM image and (e) TEM images of 2D α-MoO_3 crystals.[24]

2.3.3 Chemical vapour deposition

Bottom-up CVD is an effective technique that has recently been adopted for studying the scalable and reliable production of large-area 2D materials. In particular, this technique relies on the direct synthesis of 2D materials from different precursors by chemical reactions or the direct growth of the precursor under certain experimental conditions on various substrates.[46-49] Figure 2.5a illustrates the experimental setup for 2D MoO_{3-x} growth.[12] In a typical process, the given substrate is exposed to one or two reactive precursors at a high temperature in a high vacuum furnace. Herein the volatile precursors react and/or decompose on the surface of the substrate to form 2D crystals or large-area ultra-thin films. As such, 2D materials can be synthesised on a wafer scale by controlling the growth parameters (pressure, temperature and time, etc.), precursors and substrates. Ultra-thin 2D dichalcogenides with a high crystal quality, scalable size, tuneable thickness and excellent electronic properties are produced.[50-51] Kim *et al*. reported crystalline-layered nature of CVD-grown bulk MoO_3 using single precursor MoO_3 powder (Figure 2.5b, c).[52] As such, the large area growth of 2D MoO_3 would be worthwhile for fundamental study and its electronic applications.

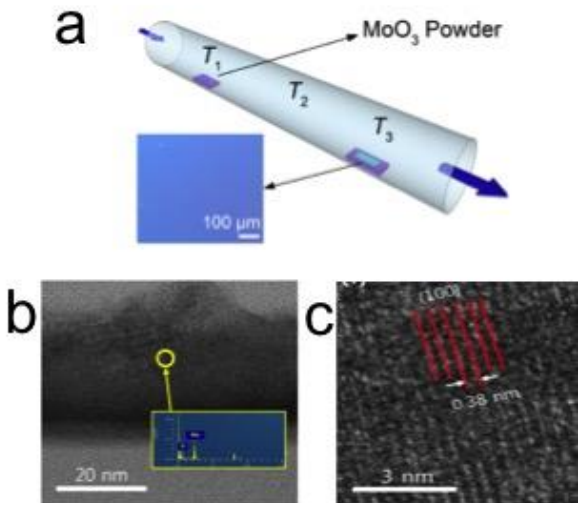

Figure 2.5 Schematic diagram of the CVD process for MoO_{3-x} growth.[12] (b) TEM cross-section image of the sample obtained by exposing the sample to a FIB; the inset shows the EDS spectrum of MoO_3. (c) STEM mode image of MoO_3.[52]

2.4 Applications

The unprecedented physical, electronic, chemical and optical properties of 2D materials arising from their unique structural features offer great potential for numerous applications. The abundant numbers in the family of 2D materials with versatile properties enable us to select materials specific to the desired application. Ultrathin 2D materials have been explored for various uses in electronics, optoelectronics, gas and biosensors and energy storage.[2, 16, 19, 53] As such, some promising applications based on 2D material platforms, particularly focusing on FETs,[11, 21, 54-55] resistive memory[56-57] and gas sensors[58-59] have been highlighted in this section.

2.4.1 Field Effect Transistors

The most important basic building block of modern-era electronic circuits is the FET, mostly used as a switch in digital circuits. An ideal transistor channel material should satisfy several criteria, such as having high charge carrier mobility for faster operation, high on/off ratios and a high dielectric value to reduce unexpected charge carrier scattering. Two-dimensional materials, representing the ultimate limit of miniaturisation in the vertical dimension, are therefore highly interesting, as they allow a great degree of electrostatic control. To date, graphene has been the most investigated 2D material, as it shows the high carrier mobility of 10^5 $cm^2V^{-1}s^{-1}$ at room temperature due to confined electrons in graphene behaving like massless Dirac fermions.[60] However, the lack of an intrinsic bandgap of graphene has drawn attention to alternative layered materials, such as transition metal dichalcogenides and MoS_2, despite their electrical performance remaining relatively low.[61-63] Radisavljevic *et al*. have reported modulation in single layer MoS_2 where carrier mobility is ~217 $cm^2V^{-1}s^{-1}$ (Figure 2.6a-c).[11] Wide band gap MoO_3 has a naturally low free-carrier concentration, which

is challenging for FET applications. Nonetheless, the stoichiometry of the material can be tuned, resulting in increased in free-carrier concentrations that lead to fabrication of 2D FETs. Indeed, electronic properties of liquid exfoliated 2D MoO_3 nanoflakes have been successfully tuned by manipulating the level of oxygen deficiencies and used as printable semiconducting ink for printing and bio sensing FETs.[23,55] Balendhran *et al*. reported that intrinsic high dielectric values of 2D MoO_3 provide an environment that reduce Coulomb scattering during transport, resulting in enhanced carrier mobility (Figure 2.6d–f).[21] Furthermore, MoO_3 was used as the surface over layer, which is able to modulate the transport properties of MoS_2 based FETs.[64] As such, exfoliated MoO_3 with a high dielectric constant has been studied as a channel, as it shows excellent carrier mobility and a higher on/off ratio.

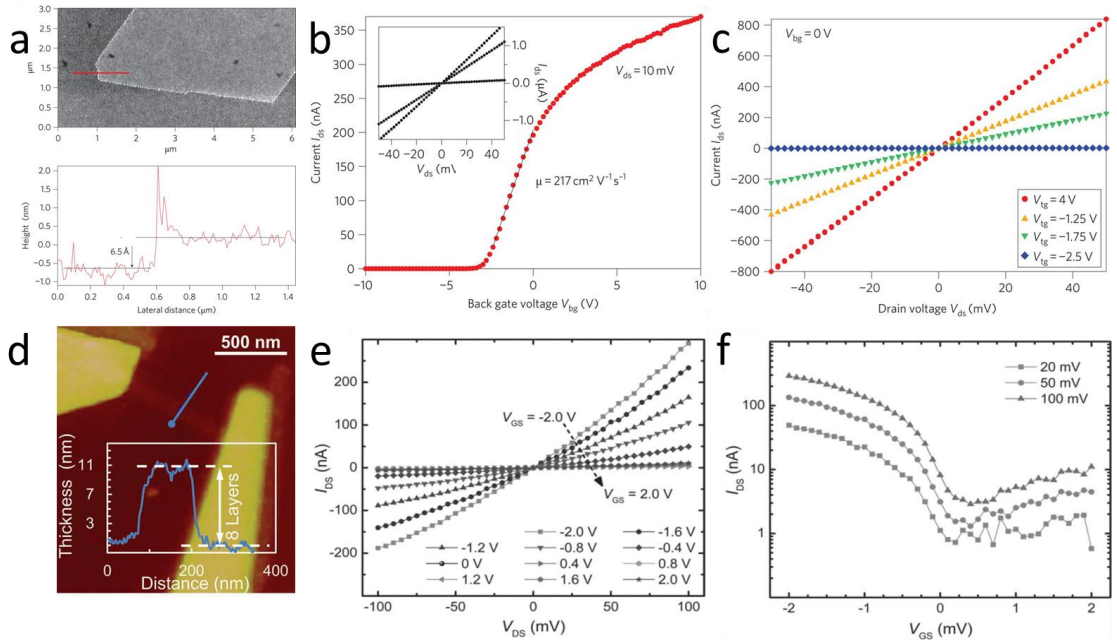

Figure 2.6(a) AFM image of a single layer of MoS_2 crystal and corresponding cross- sectional plot along the red line. (b) Room-temperature transfer characteristic for the FET with 10 mV applied bias voltage V_{ds}. Inset: I_{ds}-V_{ds} curve acquired for V_{bg} values of 0, 1 and 5 V. (c) I_{ds}-V_{ds} curves recorded for different values of V_{tg}.[11](d) AFM scan and the corresponding thickness profile of a MoO_3 FET fabricated by electron beam direct writing. (e) I_{ds}-V_{ds} characteristics of the FET with varying back-gate voltages (V_{gs}) in steps of 0.4 V from −2 to + 2 V. (b) Corresponding I_{ds}-V_{gs} curves of the FET acquired at V_{ds} values of 20, 50, and 100 mV.[21]

2.4.2 Resistive memories

The current digital era of smart devices demands efficient and high-density electronics. It becomes notably difficult to retain a charge reliably in existing Si-based technology due to its theoretical and physical limitations.[65-67] Non-volatile resistive memory technology has the potential to offer high-performance memory devices due to their simple physical structure, scalability and reliable characteristics. [68-69] Metal oxides with a high dielectric value are the most popular active material, as they exhibit reversible resistive switching behaviours. In general, the oxygen vacancies of the oxide material play an important role in such switching behaviour under the influence of applied external electric fields.[70] These oxygen vacancies sometimes exist in the system, or they may be generated by inducing a thermal or electrical reduction. It is believed that under the influence of an applied electric field, these oxygen vacancies diffuse through the channel material that forms one/more conductive filamentary paths. Consequently, these filamentary paths form and rupture with changes in the biasing voltages. In some cases these oxygen vacancies causing physical deformation of the junction, which can be mitigated by shrinking to the nanoscale and controlling the electroforming voltage polarity.[70] However, existing oxide-based memory cells experience several drawbacks, such as a high electroforming voltage, poor retention and low switching ratios.[64,71-78] As a result, research has been extended to understand the resistive behaviour of 2D materials, as they show excellent electronic properties. Several reports of reversible resistive memory applications based on 2D MoS_2 have been published that show resistive memory, but with comparatively poor performances.[9,13,56] Cheng *et al.* shown resistive memory behaviour in 1T phase MoS_2 crystals (Figure 2.7a and b).[9] Further, Sangwan *et al.* reported grain boundary mediated resistive memory behaviour in single layer MoS_2 (Figure 2.7c, d).[13] M. Arita *et al.* notably examined the potential of MoO_3 prepared by thermal oxidation of Mo films, in the resistive random-access memory (RERAM) switching

(Figure 2.7e, f and g).[79] However, neither reproducibility nor stability of the reported MoO_3–based ReRAM switching was significant. Z-H. Tan *et al*. synthesised MoO_3 nanobelts using hydrothermal method for a resistive switching performance study. This showed stable unipolar switching with high ON/OFF ratio and demonstrated that the electroforming process introduces defect states in MoO_3 (Figure 2.7h, i and j).[80] Despite the high ON/OFF ratio, the cyclic endurance of the memory devices was not established. Thus, MoO_3 which can exist in multiple stable oxidation states is favourable for resistive switching memory devices. However, there is no detailed study of stable and repeatable 2D MoO_3-based resistive switching applications. Considering the high-dielectric value of MoO_3, and enhanced carrier mobility observed in 2D structures, it would be valuable to study the resistive memory behaviour of planar 2D MoO_3.

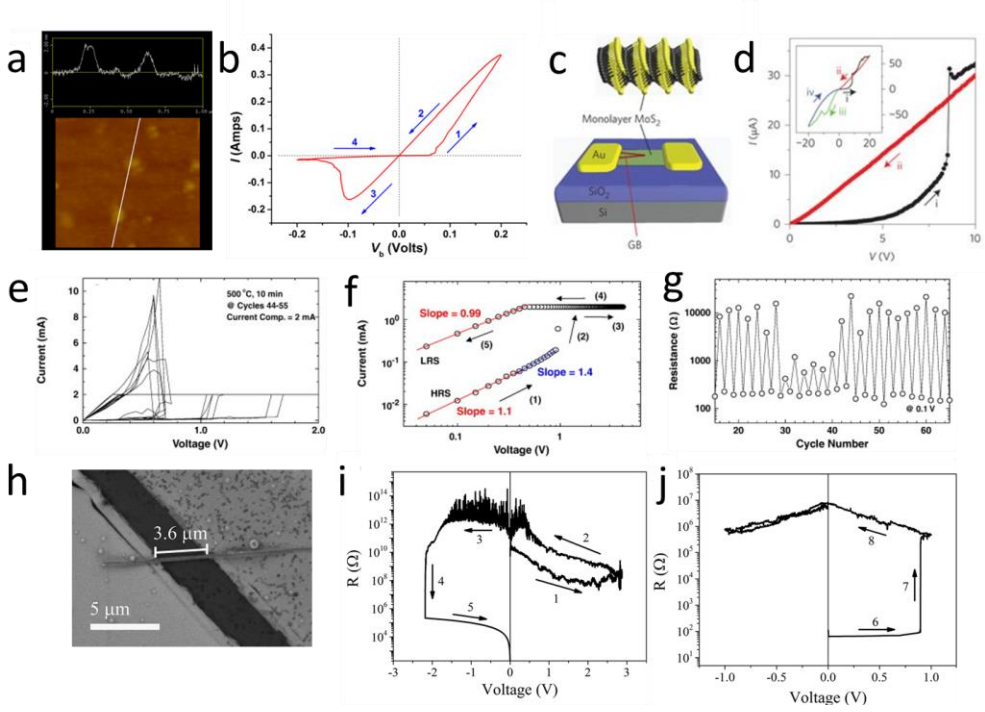

Figure 2.7(a) AFM image and corresponding height profile of MoS_2 nanosheets (b) Typical *I–V* characteristic of Ag/MoS_2/Ag switch at room temperature.[9] (c) Schematic of a MoS_2 memristor (d) Partial *I–V* characteristics of an electroformed MoS_2 memristor.[13] (e) *I–V* curve showing set and reset processes. (f) The log–log plot of the voltage and the current during the set process where the numbers denote the sequence of voltage application. (g) The endurance property where the resistance was estimated at 0.1 V. [79](h) scanning electron microscopy (SEM) image of an Au/MoO_3/Au device.(i) *R-V* curves of the first cycle of voltage sweeping. (j) ON and OFF retention states.[80]

2.4.3 Sensors

Environmental pollution is one of the greatest challenges in the modern era. The continuous emission of toxic gases in the air has accelerated the study and investigation of effective gas sensors. Among these gases, nitrogen oxide (NO_2) and hydrogen sulphide (H_2S) are highly toxic and hazardous. Even at significantly low concentrations, they cause severe effects on the nervous system.[81-82] As such, detecting traces of such gases in the atmosphere is essential for both human health and environmental safety. Until now, semiconducting metal oxides are largely used as sensor materials due to their high sensitivity towards many target gases, as well as their low cost, easy fabrication and compatibility with present technology.[83-85] Accordingly, many metal oxides, such as SnO_2,[84] CuO[86-88] and WO_3,[89] as well as MoO_3[90-93] thin films and nanostructures, have been used to detect H_2S and NO_2, as they show excellent sensing properties. Among them MoO_3 has been extensively studied in gas-sensing applications due to their noticeable surface sensitivity to reducing and oxidizing gases at elevated operating temperatures.[91-92] However, the demand for highly sensitive, selective, low-power consuming and reliable sensors has motivated research on 2D material-based sensors. The high surface-to-volume ratio, along with the excellent electronic properties of 2D materials, offer the potential for the detection of large amounts of target analysts per unit area, as well as result in a rapid response and recovery with low power consumption.[59,94-95] Donarelli *et al*. reported on chemically exfoliated MoS_2 based conductometric gas sensors (Figure 2.8a).[10] These exfoliated MoS_2 flakes exhibited dynamic sensing response towards NO_2 at a temperature of 200 °C. However, the sensors demonstrated poor selectivity, sensitivity and significantly long air recovery kinetics with unstable base line. Alsaif *et al.* has developed conductometric gas-sensors based on liquid exfoliated MoO_3 for H_2 sensing applications (Figure 2.8b–c).[24] The MoO_3 sensors demonstrated large sensitivity towards H_2

with fast response and recovery time. Ji *et al*. prepared 2D MoO_3 combining grinding and sonication exfoliation method, and used them for the detection of volatile organic compounds (VOCs) (Figure 2.8d–f).[95] [95] These 2D MoO_3–based sensors showed significantly faster response and recovery compared to their bulk counterparts. Usually, arrays of sensors are used to identify and detect different type of gases, which increase the size of the device and power consumption.[96] Thus, the detection of multiple gases using a single sensor is an effective solution which helps to reduce the sensor size and power consumption by minimising the number of sensors.[97] Often gas sensors exhibit similar responses to a range of gases, which results in poor selectivity. So, the response sensitivity between two or more gases should be detectable and distinguishable for reliable selectivity. Several reports show that introducing oxygen vacancies in to the lattice of sensor materials enhances the response

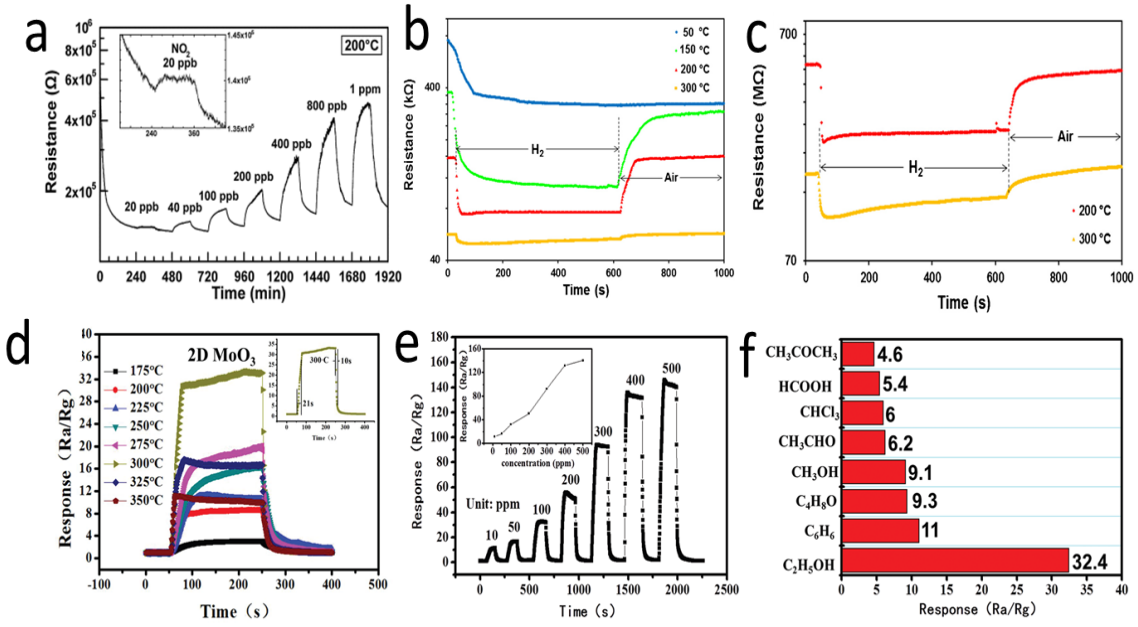

Figure 2.8 (a) Dynamic response of the MoS_2 device toward NO_2 in the range 20 ppb–1 ppm at 200 °C. Inset: magnified view of the electrical response to 20 ppb NO_2.[10] The actual resistance changes of (b) the MoO_3/Si and (c) the MoO_3/glass sensors in response to 1% of H_2 gas in dry synthetic air with respect to time at different temperatures.[24] (d) Transient sensor response toward 100 ppm alcohol vapor at different temperatures using MoO_3 nanosheets. Inset shows the response and recovery curves for the senor at its optimum working temperature (e) Response and recovery curves of the MoO_3 nanosheets based sensor toward different alcohol vapour concentration ranging from 10 ppm to 500 ppm at the optimum working temperature. (f) Sensor responses of those made of MoO_3 nanosheets toward 100 ppm VOCs.[96]

performance.[98] Thus, oxygen deficient 2D MoO_3–based conductometric sensors have been developed and the response performances of such material towards NO_2 and H_2S gases were studied as a dual gas sensor. The distinctive and unique physical and enhanced electronic properties of 2D MoO_3 made them promising candidates for the development of high sensitive and lower power consumption novel gas sensing applications.

2.5 Conclusions

Several synthesis methods for obtaining 2D MoO_3 including a collective review on the applications of 2D MoO_3 were presented in this chapter. However, research on 2D materials is in continuous progress and holds potential for the development of diverse range of applications. Based on the presented discussion, the following choices of study were made to address the identified knowledge gaps.

It is found that the contemporary exfoliation techniques do not produce pristine crystals efficiently. Hence, the post deposition etching technique will be a novel route for obtaining 2D crystals, as this direction has never been explored in order to obtain pure crystals of 2D MoO_3 controllably. Consequently the study of both physical and electronic properties based on such etched 2D crystals would confirm the viability of the method and would be beneficial for nano-electronic applications. A detailed study on the etching method will be presented in Chapter 3.

Though 2D materials show excellent electronic and physical properties, no study has been carried out for understanding the resistive memory behaviour of sub-stoichiometric 2D MoO_3 crystals. The sub-stoichiometric nature of MoO_3 provides the oxygen deficiencies, which are required for electroforming and switching mechanism. Hence, to understand the switching mechanism of such planar system, the sub-stoichiometric 2D MoO_3 crystals-based memory-

performance characterisation will be studied and presented in Chapter 4.

Evidently, 2D materials have the potential to act as high performance sensor materials due to their unique physical properties, including a high surface-to-volume ratio, tuneable bandgaps and high absorption coefficient. However, the gas-sensing characteristics of 2D crystals in non-stoichiometric α-MoO_3 have rarely been studied. Exploration of such 2D gas-sensing systems is an important next step to realise high performance gas-sensing technology. As such, a detail sensing characterisation of 2D non-stoichiometric α-MoO_3 will be presented in Chapter 5.

2.5 References:

1. Hsu, A., *et al*., Large-area 2-D electronics: Materials, technology, and devices. Proc. IEEE **2013,** 101 (7), 1638-1652.

2. Wang, Q. H., *et al*., Electronics and optoelectronics of two-dimensional transition metal dichalcogenides. Nat. Nanotechnol. **2012,** 7, 699.

3. Zhu, Y., *et al*., Graphene and graphene oxide: Synthesis, Properties, and Applications. Adv. Mater **2010,** 22 (35), 3906-3924.

4. F. Bonaccorso, Z. S., T. Hasan, A. C. Ferrari, Graphene photonics and optoelectronics. Nat. Photonics **2010,** 4, 611.

5. Neto, A. H. C., *et al*., The electronic properties of graphene. Rev. Mod. Phys. **2009,** 81 (1), 109-162.

6. Novoselov, K. S., *et al*., Electric field effect in atomically thincarbon films. Science **2004,** 306 (5696), 666.

7. Balendhran, S., *et al*., Elemental Analogues of Graphene: Silicene, Germanene, Stanene, and Phosphorene. Small **2015,** 11 (6), 640-652.

8. Novoselov, K. S.; Neto, A. H. C., Two-dimensional crystals-based heterostructures: materials with tailored properties. Physica Scripta **2012,** 2012 (T146), 014006.

9. Cheng, P., *et al*., Memristive Behavior and Ideal Memristor of 1T Phase MoS_2 Nanosheets. Nano Lett. **2016,** 16 (1), 572-576.

10. Donarelli, M., *et al*., Response to NO_2 and other gases of resistive chemically exfoliated MoS_2-based gas sensors. Sens. Actuators, B **2015,** 207, 602-613.

11. Radisavljevic, B., *et al*., Single-layer MoS_2 transistors. Nat. Nanotechnol. **2011,** 6, 147.

12. Arash, A., *et al*., Large-scale synthesis of 2D MoO_{3-x} for enhanced optoeletronics applications . 2D Mater. **2019,** 6 (3), 035031.

13. Sangwan, V. K., *et al*., Gate-tunable memristive phenomena mediated by grain boundaries in single-layer MoS_2. Nat. Nanotechnol. **2015,** 10 (5), 403-406.

14. Feng, W., *et al*., Synthesis, properties and applications of 2D non-graphene materials. Nanotechnology **2015,** 26 (29), 292001.

15. Akinwande, D., *et al*., Two-dimensional flexible nanoelectronics. Nat Commun **2014,** 5, 5678.

16. Balendhran, S., *et al*., Two-dimensional molybdenum trioxide and dichalcogenides. Adv. Funct. Mater. **2013,** 23 (32), 3952-3970.

17. Fiori, G., *et al*., Electronics based on two-dimensional materials. Nature Nanotechnol **2014,** 9, 768.

18. Gupta, A., *et al*., Recent development in 2D materials beyond graphene. Progress in Materials Science **2015,** 73, 44-126.

19. Choi, W., *et al*., Recent development of two-dimensional transition metal dichalcogenides and their applications. Mater. Today **2017,** 20 (3), 116-130.

20. Novoselov, K. S., *et al*., Two-dimensional atomic crystals. Proc. Natl. Acad. Sci. U.S.A. **2005,** 102 (30), 10451-10453.

21. Balendhran, S., *et al*., Enhanced charge carrier mobility in two-dimensional high dielectric molybdenum oxide. Adv. Mater. **2013,** 25 (1), 109-14.

22. Wang, H., *et al*., Physical and chemical tuning of two-dimensional transition metal dichalcogenides. Chem. Soc. Rev. **2015,** 44 (9), 2664-2680.

23. Balendhran, S., *et al*., Field effect biosensing platform based on 2D α-MoO_3. ACS Nano **2013,** 7 (11), 9753-9760.

24. Alsaif, M. M. Y. A., *et al*., Two dimensional α-MoO_3 nanoflakes obtained using solvent-assisted grinding and sonication method: Application for H_2 gas sensing. Sens. Actuators, B **2014,** 192, 196-204.

25. Dagar, J., *et al*., Application of 2D-MoO_3 nano-flakes in organic light emitting diodes: Effect of semiconductor to metal transition with irradiation. RSC Advances **2015,** 5 (11), 8397-8403.

26. Hanlon, D., *et al*., Production of molybdenum trioxide nanosheets by liquid exfoliation and their application in high-performance supercapacitors. Chem. Mater. **2014,** 26 (4), 1751-1763.

27. Zheng, Q., *et al*., A flexible ultraviolet photodetector based on single crystalline MoO3 nanosheets. J. Mater. Chem. C **2015,** 3 (28), 7469-7475.

28. Bessonov, A. A. K., M. N. Petukhov, D. I. Allen, M. Ryhänen, T. Bailey, M. J. A., Layered memristive and memcapacitive switches for printable electronics. Nat. Mater. **2015,** 14 (2), 199-204.

29. Carcia, P. F.; McCarron, E. M., Synthesis and properties of thin film polymorphs of molybdenum trioxide. Thin Solid Films **1987,** 155, 53-63.

30. Shimizu, R., *et al.*, Low-temperature deposition of meta-stable β-MoO_3(011) epitaxial thin films using step-and-terrace substrates. Thin Solid Films **2015,** 595, 153-156.

31. Smith, R. L.; Rohrer, G. S., Scanning probe microscopy of cleaved molybdates: α-MoO_3(010), $Mo_{18}O_{52}$(100), Mo_8O_{23}(010), and η-Mo_4O_{11}(100). J. Solid State Chem **1996,** 124 (1), 104-115.

32. Kalantar-zadeh, K., *et al*., Synthesis of nanometre-thick MoO_3 sheets. Nanoscale **2010,** 2 (3), 429-33.

33. Inzani, K., *et al*., Electronic properties of reduced molybdenum oxides. Physical Chemistry Chemical Physics **2017,** 19 (13), 9232-9245.

34. Rabalais, J. W., *et al*., Trapped electrons in substoichiometric MoO_3 observed by X-ray electron spectroscopy. Chem. Phys. Lett. **1974,** 29 (1), 131-133.

35. Chen, C. Z., *et al*., Evidence of oxygen vacancy and possible intermediate gap state in layered α-MoO_3 single-crystal nanobelts. Physica B: Condensed Matter **2016,** 481, 192-196.

36. Ou, J. Z., *et al*., In Situ Raman Spectroscopy of H_2 Gas Interaction with Layered MoO3. The Journal of Physical Chemistry C **2011,** 115 (21), 10757-10763.

37. Tagaya, H., *et al*., Intercalation of organic compounds in the layered host lattice MoO_3. Journal of Materials Chemistry **1994,** 4 (4), 551-555.

38. Wang, J., *et al.*, The preparation of polyaniline intercalated MoO_3 thin film and its sensitivity to volatile organic compounds. Thin Solid Films **2006,** 514 (1), 329-333.

39. Fleisch, T. H.; Mains, G. J., An XPS study of the UV reduction and photochromism of MoO_3 and WO_3. The Journal of Chemical Physics **1982,** 76 (2), 780-786.

40. Li, H., *et al*., Preparation and Applications of Mechanically Exfoliated Single-Layer and Multilayer MoS_2 and WSe_2 Nanosheets. Acc. Chem. Res. **2014,** 47 (4), 1067-1075.

41. Ottaviano, L., *et al*., Mechanical exfoliation and layer number identification of MoS_2 revisited. 2D Materials **2017,** 4 (4), 045013.

42. Tang, D.-M., *et al*., Nanomechanical cleavage of molybdenum disulphide atomic layers. Nature Communications **2014,** 5, 3631.

43. Eda, G., *et al*., Photoluminescence from chemically exfoliated MoS_2. Nano Letters **2011,** 11 (12), 5111-5116.

44. Matte, H. S. S. R., *et al*., Graphene analogues of layered metal selenides. Dalton Trans. **2011,** 40 (40), 10322-10325.

45. Huang, Q., *et al*., MoO_{3-x}-based hybrids with tunable localized surface plasmon resonances: Chemical oxidation driving transformation from ultrathin nanosheets to nanotubes. Chem. Eur. J. **2012,** 18 (48), 15283-15287.

46. Wang, X., *et al*., Chemical vapor deposition growth of crystalline monolayer $MoSe_2$. ACS Nano **2014,** 8 (5), 5125-5131.

47. Jeon, J., *et al*., Layer-controlled CVD growth of large-area two-dimensional MoS_2 films. Nanoscale **2015,** 7 (5), 1688-1695.

48. Qiu, D., *et al*., Structural and optical properties of MoS_2 layers grown by successive two-step chemical vapor deposition method. Thin Solid Films **2015,** 587, 47-51.

49. Yu, J., *et al*., Large-scale synthesis of 2D metal dichalcogenides. J. Mater. Chem. **2018,** 6 (17), 4627-4640.

50. Lu, X., *et al*., Large-area synthesis of monolayer and few-layer $MoSe_2$ films on SiO_2 substrates. Nano Lett **2014,** 14 (5), 2419-25.

51. Dai, T. J., *et al*., Layer-controlled synthesis of wafer-scale $MoSe_2$ nanosheets for photodetector arrays. J Mater Sci **2018,** 53 (11), 8436-8444.

52. Kim, H. U., *et al*., Highly uniform wafer-scale synthesis of α-MoO_3 by plasma enhanced chemical vapor deposition. Nanotechnology **2017,** 28 (17), 175601.

53. Fiori, G., *et al.*, Electronics based on two-dimensional materials. Nat. Nanotechnol. **2014,** 9, 768.

54. Nourbakhsh, A., *et al*., MoS_2 Field-Effect Transistor with Sub-10 nm Channel Length. Nano Letters **2016,** 16 (12), 7798-7806.

55. Alsaif, M. M. Y. A., *et al*., High-performance field effect transistors using electronic inks of 2D molybdenum oxide Nanoflakes. Adv. Funct. Mater. **2016,** 26, 91-100.

56. Gwang Hyuk, S., *et al.*, Multilevel resistive switching nonvolatile memory based on MoS 2 nanosheet-embedded graphene oxide. 2D Mater. **2016,** 3 (3), 034002.

57. Wang, M., *et al*., Robust memristors based on layered two-dimensional materials. Nat. Electron **2018,** 1 (2), 130-136.

58. Choi, S.-J.; Kim, I.-D., Recent developments in 2D nanomaterials for chemiresistive-type gas sensors. Electronic Materials Letters **2018,** 14 (3), 221-260.

59. Yang, S., *et al*., Gas sensing in 2D materials. Appl. Phys. Rev. **2017,** 4 (2), 021304.

60. Novoselov, K. S., *et al*., Two-dimensional gas of massless Dirac fermions in graphene. Nature **2005,** 438, 197.

61. Osada, M.; Sasaki, T., Twodimensional dielectricnanosheets: Novel nanoelectronics from nanocrystal building blocks. Adv. Mater **2012,** 24 (2), 210-228.

62. Kim, H., *et al*., Optimized single-layer MoS_2 field-effect transistors by non-covalent functionalisation. Nanoscale **2018,** 10 (37), 17557-17566.

63. Liu, W., *et al*., High-performance few-layer-MoS_2 field-effect-transistor with record low contact-resistance, 2013 IEEE International Electron Devices Meeting, 9-11 Dec. 2013; 2013; pp 19.4.1-19.4.4.

64. Lin, J., *et al*., Modulating electronic transport properties of MoS_2 field effect transistor by surface overlayers. Applied Physics Letters **2013,** 103 (6), 063109.

65. Kingon, A. I., *et al*., Alternative dielectrics to silicon dioxide for memory and logic devices. Nature **2000,** 406 (6799), 1032-1038.

66. Sawa, A., Resistive switching in transition metal oxides. Mater. Today **2008,** 11 (6), 28-36.

67. Kim, K. M., *et al*., Nanofilamentary resistive switching in binary oxide system; a review on the present status and outlook. Nanotechnology **2011,** 22 (25), 254002.

68. B. Mohammad, M. A. J., V. Kumar, D. M. A. Homouz, H. A. Nahla, M. A. Qutayri, and N. Christoforou, State of the art of metal oxide memristor devices. Nanotechnol. Rev. **2016,** 5 (3), 311-329.

69. Liang, L., *et a*l., Vacancy associates-rich ultrathin nanosheets for high performance and flexible nonvolatile memory device. J. Am. Chem. Soc. **2015,** 137 (8), 3102-8.

70. Yang, J. J., *et al*., The mechanism of electroforming of metal oxide memristive switches. Nanotechnology **2009,** 20 (21), 215201.

71. Pickett, M. D., *et al*., Switching dynamics in titanium dioxide memristive devices. J. Appl. Phys. **2009,** 106 (7), 074508.

72. Qu, B., *et al*., Recent progress in tungsten oxides based memristors and their neuromorphological applications. Electron. Mater. Lett. **2016,** 12 (6), 715-731.

73. Hota, M. K., *et al.*, Electroforming free resistive switching memory in two-dimensional VO_x nanosheets. Appl. Phys. Lett. **2015,** 107 (16), 163106.

74. H. Nili, *et al*., Microstructure and dynamics of vacancy-induced nanofilamentary switching network in donor doped $SrTiO_{3-x}$ memristors. Nanotechnology **2016,** 27 (50), 505210.

75. Choi, J. G.; Thompson, L. T., XPS study of as-prepared and reduced molybdenum oxides. Appl. Surf. Sci. **1996,** 93 (2), 143-149.

76. Wang, Z., *et al*., Modulation of nonlinear resistive switching behavior of a TaO_x-based resistive device through interface engineering. Nanotechnology **2017,** 28 (5), 055204.

77. He, W., *et al*., Customized binary and multi-level HfO_{2-x}-based memristors tuned by oxidation conditions. Sci. Rep. **2017,** 7 (1), 10070.

78. Lee, D., *et al*., Resistance switching of copper doped MoO_x films for nonvolatile memory applications. Appl. Phys. Lett. **2007,** 90 (12), 122104.

79. Tan, Z.-H., *et al*., One-dimensional memristive device based on MoO_3 nanobelt. Appl. Phys. Lett. **2015,** 106 (2), 023503.

80. M Arita, H. K., T. Fujii, Y. Takahashi, Resistance switching properties of molybdenum oxide films. Thin Solid Films **2012,** 520, 4762-4767.

81. Afzal, A., *et al*., NO_x sensors based on semiconducting metal oxide nanostructures: Progress and perspectives. Sens. Actuators, B **2012,** 171-172, 25-42.

82. Chen, Y. J., *et al*., Porous iron molybdate nanorods: in situ diffusion synthesis and low-temperature H_2S gas sensing. ACS Appl. Mater. Interfaces **2013,** 5 (8), 3267-74.

83. Gutruf, P., *et al*., Stretchable and tunable microtectonic ZnO-based sensors and photonics. Small **2015,** 11 (35), 4532-9.

84. H. Zhang, J. F., T. Fei, S. Liu, T. Zhang, , SnO_2 nanoparticles-reduced graphene oxide nanocomposites for NO_2 sensing at low operating temperature. Sens. Actuators, B **2014,** 190, 472-478.

85. Liu, S., *et al*., High performance room temperature NO_2 sensors based on reduced graphene oxide-multiwalled carbon nanotubes-tin oxide nanoparticles hybrids. Sens. Actuators, B **2015,** 211, 318-324.

86. Fu, D., *et al*., Two-dimensional net-like SnO_2/ZnO heteronanostructures for high-performance H_2S gas sensor. J. Mater.Chem. A **2016,** 4 (4), 1390-1398.

87. Kong, X.; Li, Y., High sensitivity of CuO modified SnO_2 nanoribbons to H_2S at room temperature. Sens. Actuators, B **2005,** 105 (2), 449-453.

88. Qin, Y., *et al*., Hierarchically porous CuO hollow spheres fabricated via a one-pot template-free method for high-performance gas sensors. J. Phys. Chem. C **2012,** 116 (22), 11994-12000.

89. Shendage, S. S., *et al*., Sensitive and selective NO_2 gas sensor based on WO_3 nanoplates. Sens. Actuators, B **2017,** 240, 426-433.

90. Zhang, L., *et al*., Self-assembly gridding α-MoO_3 nanobelts for highly toxic H_2S gas sensors. Sens. Actuators, B **2016,** 237, 350-357.

91. Mane, A. A.; Moholkar, A. V., Orthorhombic MoO_3 nanobelts based NO_2 gas sensor. Appl. Surf. Sci. **2017,** 405, 427-440.

92. Rahmani, M. B., *et al*., Gas sensing properties of thermally evaporated lamellar MoO_3. Sensors and Actuators B: Chemical **2010,** 145 (1), 13-19.

93. Yang, S., *et al*., Highly Responsive Room-Temperature Hydrogen Sensing of alpha-MoO_3 Nanoribbon Membranes. ACS Appl. Mater. Interfaces **2015,** 7 (17), 9247-53.

94. Neri, G., Thin 2D: The new dimensionality in gas sensing. Chemosensors **2017,** 5 (3), 1-21.

95. Liu, B., *et al*., High-performance chemical sensing using schottky-contacted chemical vapor deposition grown monolayer MoS_2 transistors. ACS Nano **2014,** 8 (5), 5304-5314.

96. Ji, F., *et al*., 2D-MoO_3 nanosheets for superior gas sensors. Nanoscale **2016,** 8 (16), 8696-703.

97. Zhang, S., *et al*., A sensor array optimization method for electronic noses with sub-arrays. Sens. Actuators, B **2009,** 142 (1), 243-252.

98. Zhou, J. Y., *et al*., Gas sensing enhancing mechanism via doping-induced oxygen vacancies for gas sensors based on indium tin oxide nanotubes. Sens. Actuators, B **2018,** 265, 273-284.

Chapter 3 : FIELD EFFECT TRANSISTORS BASED ON CHEMICALLY ETCHED 2D MoO_3

Existing exfoliation techniques (both mechanical and liquid-phase exfoliation) to obtain 2D MoO_3 do not produce high-yield pure crystals with a uniform thickness simultaneously. In this chapter, a novel wet chemical etching route in order to obtain 2D MoO_3 crystals is presented. The reliability and repeatability of the chemical etching technique of obtaining 2D MoO_3 is investigated thoroughly. In addition, extensive characterisations of MoO_3 crystals are carried out pre- and post-etching to establish the material's compositional integrity through the etching process. FETs based on these 2D MoO_3 crystals have been demonstrated to assess the transport properties of the post-etched material.

3.1 Introduction

Two-dimensional materials yield a high specific surface area with quantum confinement of charge carriers, which offer extraordinary mechanical, optical and electronic properties in comparison to their bulk counterparts.[1-3] Graphene has been the most investigated 2D material, since its discovery more than a decade ago. However, the lack of an intrinsic energy band gap has hindered the widespread deployment of graphene in nano-electronic applications.[4] Hence, an extensive effort has been applied into the exploration of other semiconducting 2D materials, from both scientific and application point of view. Reliable production of high purity, crystalline 2D materials is a crucial aspect for studying them and translating their electronic and optical properties into a viable technology.

Typically, 2D materials can be realized by bottom-up synthesis and top-down exfoliation methods. CVD has been the most effective and widely adopted bottom-up technique, commonly used in the large area growth of 2D crystals (graphene,[5] MoS_2[6-7]). However, obtaining the desired thickness of 2D materials using CVD is rather complicated as it involves several parameters to be optimised such as amount of precursor, deposition temperature/pressure, and carrier gas flow rate. The top-down synthesis methods include mechanical[3, 8] and liquid [9-10] phase exfoliation processes. Liquid phase exfoliation has a higher yield of 2D crystals, but generally carries significant traces of contaminants from the solvents which tend to affect the intrinsic properties of the material. As a result, the structural and electronic qualities of liquid phase exfoliated 2D materials are compromised. Mechanical exfoliation is the simplistic traditional process to achieve 2D crystals, first demonstrated for graphene.[11] This process provides crystals of high purity, which is ideal for electronic device applications and fundamental research. However, the exfoliated crystals are found in random lateral sizes and thicknesses, making it challenging to obtain single crystals with desired thicknesses on-demand. As a result, post-deposition etching of the multi-layered crystals is a promising avenue towards the sustainable production of 2D crystals with desired thicknesses. Recently, wet chemical thinning of MoS_2 using HNO_3,[12] laser thinning,[13] and layer-by-layer thinning of MoS_2 by using XeF_2[14] has been reported. However, there has not been any reported post deposition thinning method to controllably obtain 2D MoO_3 crystals.

This work explores a facile and low-cost, top-down, wet chemical etching method to obtain 2D crystals of MoO_3. The reliability and repeatability of the chemical etching process is investigated. Extensive characterisations of the MoO_3 crystals are carried out pre- and post-etching, in order to establish the retention of the material's compositional integrity through the etching process. Field effect transistors (FETs) based on these etched crystals has been demonstrated to assess the transport properties of the post-etched material.

3.2 Experimental Section

3.2.1 Preparation of MoO_3 crystals

Mechanical exfoliation of MoO_3 crystals was conducted using polydimethylsiloxane (PDMS) as an alternative to the conventional scotch-tape method.[15] Firstly, 80 nm SiO_2/Si substrates were cleaned using acetone and isopropyl alcohol, followed by drying with compressed N_2. Subsequently, the substrates were subjected to 5 min of oxygen plasma treatment, ensuring all organic residues are completely removed. The MoO_3 crystals were then cleaved using flexible pieces of PDMS and transferred onto the SiO_2/Si substrates. The samples were further subjected to oxygen plasma treatment for 2 min to remove any residue from PDMS.

3.2.2 Chemical etching process

A potassium hydroxide buffer solution was utilised as the etchant to thin the exfoliated MoO_3 crystals. This was chosen as a commercially available solution AZ400K (AZ Chemicals), which is routinely used as a developer in photolithography processes. A range of solutions with varying ratio of etchant: water content (1:100, 1:200, 1:300, 1:400, and 1:500) were prepared to identify the best ratio for controllable etching. The exfoliated MoO_3 crystals were etched for a fixed duration of 5 s, at various etchant concentrations and the solution with the slowest etch rate was adopted for further experiment and characterisation. The thinning process was then repeated multiple times to establish repeatability.

3.2.3 Characterisation

The change in thickness of MoO_3 crystals was measured using Digital Instruments D3100 atomic force microscope (AFM) under tapping mode. LabRam HR Evolution Raman

Spectrometer (laser excitation at 532 nm with a 50× objective) was utilised to assess composition of MoO_3 crystals before and after etching. A high resolution transmission electron microscope (JEOL 2100F at 200 KV) was utilised to characterise and compare the crystal structure of MoO_3 before and after etching. The devices were characterised for their electronic transport properties in a back-gated FET configuration using semiconductor parameter analyser (Keithley 4200SCS).

3.2.4 Field effect transistor fabrication

Device fabrication was carried out on the etched crystals by adopting standard photolithography. Source and drain electrodes (Au 100 nm with Cr 10 nm to promote adhesion) were deposited using electron beam deposition. The fabricated devices were subjected to liquid phase H^+ intercalation using 0.5 M H_2SO_4 in a propylene carbonate (PLC) solution at a constant bias voltage of 0.5 V.

3.3 Results and Discussion

In this study, mechanically exfoliated crystals of MoO_3 are employed. Thermodynamically stable orthorhombic α-MoO_3 phase, possesses double layers of MoO_6, stacked together through weak van der Waals forces along the [010] vertical direction (Figure 3.1). Each double layer consists of edge-sharing MoO_6 octahedra along the [001] direction and corner-sharing rows along the [100] direction. This configuration allows easy exfoliation of layers from the parent crystal. Mechanical exfoliation preferentially breaks large crystals of MoO_3 along the [001] direction resulting in long rectangular crystals (Figure 3.1a,b). This can be attributed to the doubly-coordinated $O_{(2)}$ being weaker than the triply-coordinated $O_{(3)}$ (Figure 3.1a,b).

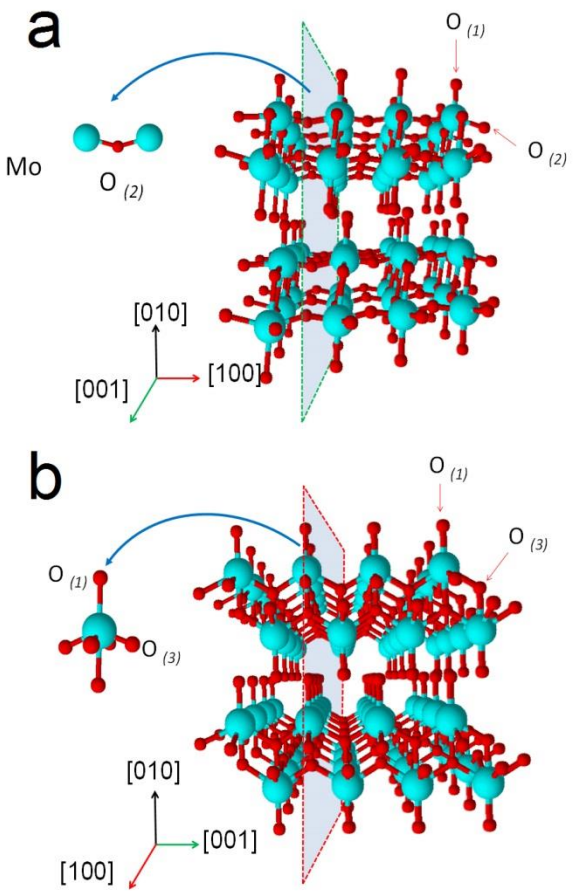

Figure 3.1 Crystal structure of MoO_3 crystal along (a) 001 direction and (b) 100

Typically, base (OH^-) solutions are known to be solvents for metal oxides. Hence, we utilise a KOH-based buffer solution to controllably etch MoO_3. Multiple etching experiments were conducted on mechanically-exfoliated MoO_3 crystals, with varying concentrations of the etchant (in water) at a constant etch duration (5 s), in order to determine an optimum etchant concentration for controlled crystal thinning. Figure 3.2a shows the statistical data regarding the change in thickness (Δt) of multiple crystals with respect to etchant ratio, obtained using atomic force microscopy. As seen in the graph, Δt is very large (~65 nm) for a 5 s etch duration, at an etchant ratio of 1:100, where controllability of the change in thickness is

minimal. The etchant is further diluted with water and, Δt is significantly lower (~5 nm) for the same etch duration, at an etchant ratio of 1:500. An overall decreasing trend of Δt with respect to the etchant ratio was observed, with the highest controllability achieved at an etchant to water ratio of 1:500. This is expected, as fewer number of cations in the etchant result in a weaker reaction with the edge sharing oxygen atoms in the crystal; thereby, providing controllability over the thinning process with respect to etch duration. As such, a ratio of 1:500 is adopted as the ratio for further characterisation of the thinning process.

Subsequently, the MoO_3 crystals were subjected to increasing etch durations using an etchant to water ratio of 1:500. The etch rate was calculated, by assessing the corresponding Δt. Figure 3.2b presents the statistical data regarding the variation in the etch rate with respect to the etch duration for multiple crystals, depicting a non-linearly rising trend in the etch rate. The non-linearity is expected due to the non-uniform distribution of the initial dimensions of the subjected crystals. The exponentially rising trend in the etch rate can be attributed to two factors: (i) the non-linearly increasing number of exposed dangling oxygen bonds in the crystal with progressing etch durations, and (ii) the exothermic process of the etching reaction results in moderately increased temperatures, which would accelerate the reaction rate with time.[14] To confirm the repeatability of the process, the experiments were conducted multiple times and the etch rate was confirmed to be consistent with the observed trend at a confidence level of 95%.

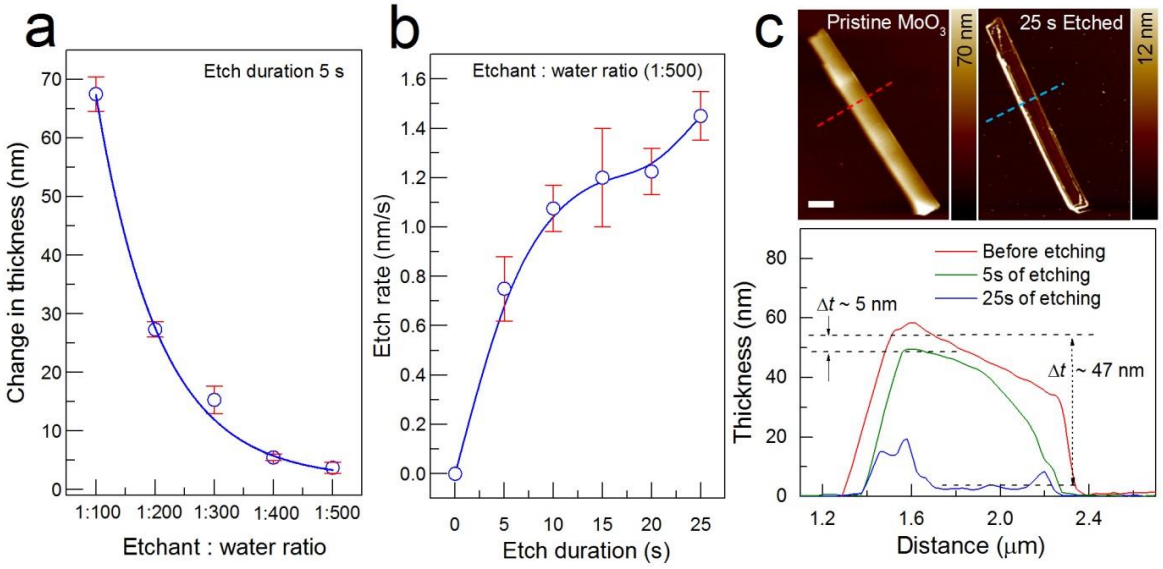

Figure 3.2 (a) Change in MoO_3 crystal thickness *vs.* ratio of the etchant to water, at a fixed etch duration of 5 s. (b) The etch rate *vs.* etch duration, at the optimum etchant ratio (1:500). Error bars in both (a) and (b) represent a confidence interval of 95%. (c) Atomic force micrographs of a MoO_3 crystal before and after 25 s of etching using the optimum ratio (1:500) of the etchant. The scale bar denotes 1 μm. The corresponding thickness profiles of the crystal along the dashed lines reveal the reduction in thickness.

Figure 3.2c shows the surface atomic force microscopy (AFM) scans of a MoO_3 crystal prior to and after 25 s of etching. The corresponding cross-sectional thickness profile (indicated by the dotted lines) of the MoO_3 crystal pre- and post-etching (at two etching steps) are indicative of the change in thickness. Cross-sectional profiles indicate that ~3 and ~33 mono layers of MoO_3 have been etched after 5 and 25 s of etching, respectively. Based on the AFM analysis of the etched crystals, it can be seen that the top-down thinning process results in the bulk crystals of MoO_3 being stripped down into 2D layers. The etch process is observed to start from the crystal edges and move inwards with time, resulting a slight reduction in lateral dimensions, as seen from the cross-sectional profile (Figure 3.2c). However, for longer etch durations (25 s) the change in thickness is uneven with bulges at the edges, which might result from the bending of unremoved MoO_3 due to strong adsorption between the substrate and the material, at the edges of the crystals.[16]

The proposed two-step etching mechanism can be described as follows: [17]

$$MoO_3 + OH^- \rightarrow H\text{–}O\text{–}MoO_3^- \quad (1)$$

$$OH^- + H\text{–}O\text{–}MoO_3^- \rightarrow MoO_4^{2-} + H_2O \quad (2)$$

There are three distinct oxygen sites in each octahedra: $O_{(1)}$ is the singly-coordinated terminal oxygen, $O_{(2)}$ is the asymmetrically-bonded bridging oxygen with the two neighbouring Mo atoms, and $O_{(3)}$ is the triply-coordinated asymmetric oxygen with two Mo atoms oriented along the (001) plane and one sublayer Mo atom[18] (Figure 3.1a, b). The etching process can be seen as the breaking of the MoO_6 octahedron to form a MoO_4 tetrahedron after reacting with the hydroxyl group (OH^-) present in the etchant. The difference in the bonding structure of Mo and O along the (100) and (001) planes results in different reactivities towards the etchant. The Mo and O atoms are unsaturated in the (100) planes, as the bridging oxygen $O_{(2)}$ between two Mo atoms becomes a terminal oxygen on the (100) plane after exfoliation. The OH^- reacts with these new terminal oxygen atoms forming $H\text{–}O\text{–}MoO_3^-$ and eventually produces MoO_4^{2-}. As such, an entire chain of MoO_6 octahedron, that shares edges and vertices through cross-linking oxygen atoms, can be peeled off sequentially from the plane.

Raman spectroscopy was employed to characterise the structural integrity of the material post-etching. Figures 3.3a-c show spatial map of the dominant Raman peak (820 cm^{-1}) intensity of a pristine MoO_3 crystal, sequentially subjected to the etching process. The 820 cm^{-1} peak in the Raman spectrum denotes the stretching mode for doubly-coordinated oxygen.[8, 19-20] The results indicate a reduction in Raman peak intensity with the etching process, which is attributed to the reducing number of MoO_3 layers present in the crystal. Full-range Raman spectra (Figure 3.3d) show the other characteristic peaks for MoO_3 at 115, 157, 197, 283, 336, 363, 666, 819, and 995 cm^{-1} [8] pre- and post-etching. The sharp nature of

the peaks suggests that the corresponding vibrational modes are from a highly-ordered structure. No shift in the positions of the peaks is observed post-etching, which suggests that the composition of MoO_3 crystals is preserved.[9,21] To verify the consistency and reproducibility of aforementioned observations, Raman analyses carried out on multiple MoO_3 crystals are presented in Figure 3.3e. As seen in Figure 3.3e, a decrease in normalised peak intensity is indicative of the reduction in MoO_3 crystal thickness,[8] whereas the average peak shift observed (~0.35 cm^{-1}) is negligible (being less than the resolution of the equipment 0.5 cm^{-1}). It can be concluded that the compositional integrity of the MoO_3 crystal remains intact post-etching.

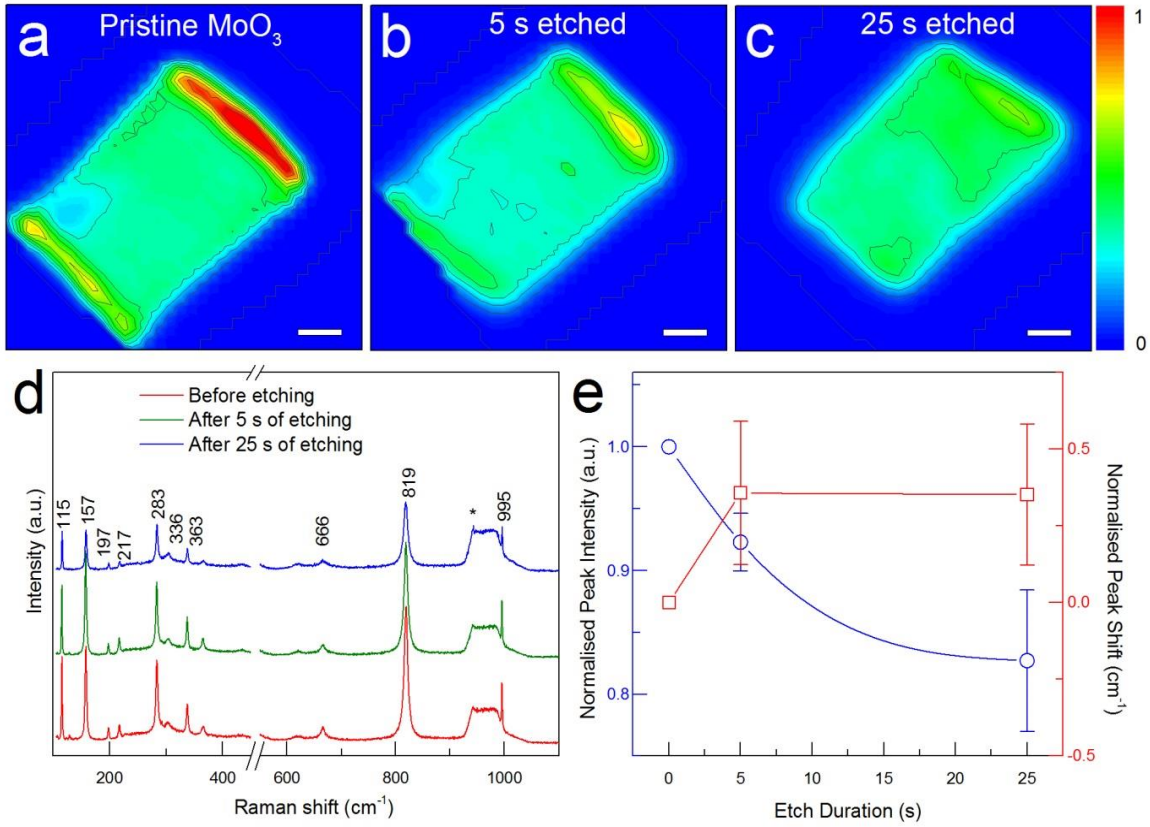

Figure 3.3 Micro-Raman maps of a (a) pristine and (b) 5 s and (c) 25 s etched MoO_3 crystal. Scale bar denotes 2 µm. Micro-Raman spectra of mechanically-exfoliated a MoO_3 crystal before and after etching steps. The etching was carried out using the optimum ratio (1:500) of the etchant for 5 s and 25 s. (e) The normalised

High-resolution transmission electron microscopy (HRTEM) was utilised to compare the crystallinity of the pristine and etched MoO_3 crystals. Figure 3.4a shows a pristine MoO_3 crystal with its corresponding selected-area electron diffraction (SAED) pattern (inset). Figures 3.4b and c present MoO_3 crystals that were subjected to 5 s and 25 s of chemical etching, respectively. The SAED patterns acquired on multiple locations of the etched crystals are in agreement with that of the pristine MoO_3 crystal. The lattice parameters calculated from the SAED patterns of the pristine and etched (5 s and 25 s duration) MoO_3 crystals show identical values, confirming there are no structural defects present initially or introduced by the etching process.

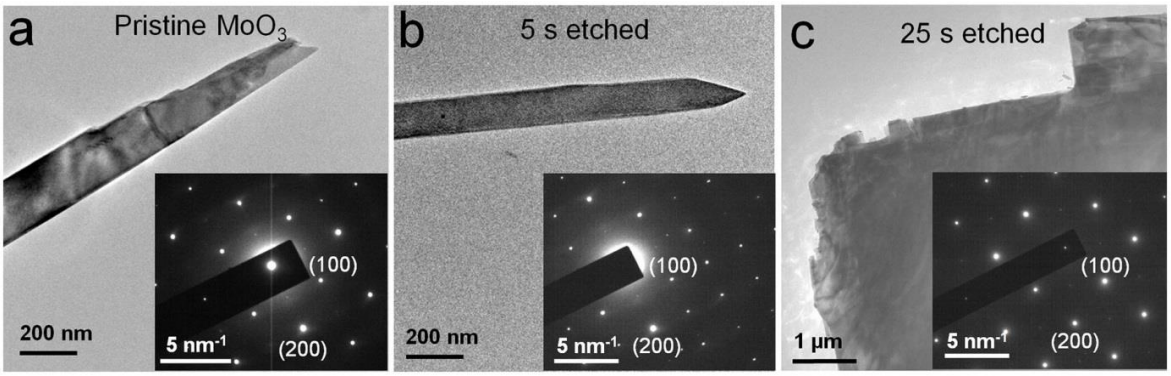

Figure 3.4 Transmission electronic micrographs with SAED patterns (as insets) of the mechanically-exfoliated and etched MoO_3 crystals: (a) pristine, (b) 5 s etched, and (c) 25 s etched. The optimum ratio

To quantify the charge transport properties of the obtained 2D MoO_3 (following 25 s of etching), field effect measurements were carried out in a back-gate configuration at room temperature. Ion intercalation was carried out in order to introduce sub-stoichiometry in the channel, making it ideal for FET applications.[9] Typical drain current *vs.* voltage (*I–V)* characteristics of a MoO_3 FET at an applied gate voltage in the range of −2.6 to 7 V are shown in Figure 3.5a. At a channel bias of 300 mV, an ON/OFF ratio of ~4,000 was observed (Figure 3.5b). A table including V_{ds} and corresponding I_{ds} of multiple working devices are

presented in Appenxdix A. The field effect carrier mobility was calculated using the following equation:

$$\mu = \frac{\Delta I_{DS}}{\Delta V_{GS}} \times \frac{l}{CwV_{DS}} \quad (3)$$

where $\Delta I_{DS}/\Delta V_{GS}$ is the transconductance, l is the channel length, w is the channel width, and C *(*~4.3×10^{-8} F/cm^2*)* is the gate capacitance per unit area V_{DS} is the drain–source voltage (300 mV). The carrier mobility was calculated to be ~175 cm^{2}V^{-1}s^{-1}. The room temperature ON/OFF ratio and carrier mobility values of ~4,000 and 175 cm^{2}V^{-1}s^{-1}, respectively are

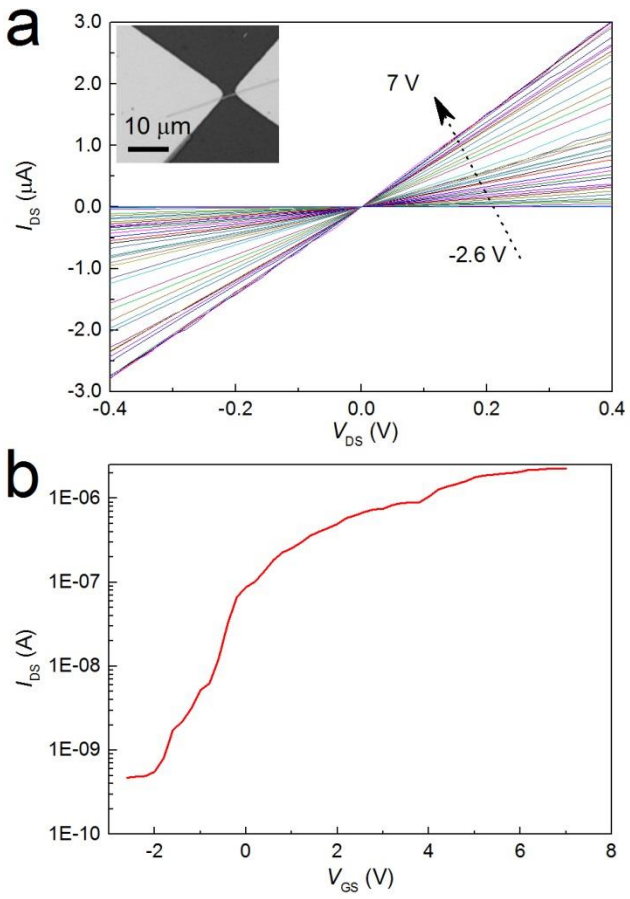

Figure 3.5 The experimental *I*–*V* characteristics of a 25 s etched MoO_3 FET. (a) I_{DS} *vs.* V_{DS} characteristics of the FET with varying back-gate voltages (V_{GS}) in steps of 0.2 V from −2.6 V to +7 V. Inset shows an optical micrograph of the FET. (b) Corresponding I_{DS}–V_{GS} curves of the FET acquired at V_{DS} values of 300 mV.

comparable to other 2D dichalcogenide-based FETs.[22] However, by adopting alternate device architectures and dielectric capping, carrier scattering can be further reduced, improving the carrier mobility.

3.4 Conclusions

In conclusion, the adopted wet chemical etching process provides a low-cost and easily deployable method to obtain high quality 2D crystals of MoO_3. No compositional and structural changes in the MoO_3 crystal are introduced as a result of the etching process. This is also evidenced by the demonstration of FETs which exhibit low-voltage switching ratios that are $>10^3$. This provides a controllable and simple process to integrate 2D MoO_3 as the functional and tunable material in 2D electronics.

3.5 References

1. Cheng, R., *et al*., Few-layer molybdenum disulfide transistors and circuits for high-speed flexible electronics. Nat. Commun. **2014,** 5, 1-9.

2. Wang, Q. H., *et al*., Electronics and optoelectronics of two-dimensional transition metal dichalcogenides. Nat Nano **2012,** 7 (11), 699-712.

3. Balendhran, S., *et al*., Two-dimensional molybdenum trioxide and dichalcogenides. Adv. Funct. Mater. **2013,** 23 (32), 3952-3970.

4. Wang, F., *et al*., Synthesis, properties and applications of 2D non-graphene materials. Nanotechnology **2015,** 26 (29), 1-26.

5. Reina, A., *et al*., Large area, few-layer graphene films on arbitrary substrates by chemical vapor deposition. Nano Letters **2009,** 9 (1), 30-35.

6. Jeon, J., *et al*., Layer-controlled CVD growth of large-area two-dimensional MoS_2 films. Nanoscale **2015,** 7 (5), 1688-1695.

7. Senthilkumar, V., *et al*., Direct vapor phase growth process and robust photoluminescence properties of large area MoS_2 layers. Nano Research **2014,** 7 (12), 1759-1768.

8. Kalantar-Zadeh, K., *et al*., Synthesis of nanometre-thick MoO_3 sheets. *Nanoscale* **2010,** 2 (3), 429-433.

9. Balendhran, S., *et al*., Enhanced charge carrier mobility in two-dimensional high dielectric molybdenum oxide. Adv. Mater. **2013,** 25 (1), 109-114.

10. Alsaif, M. M. Y. A., *et al*., High-performance field effect transistors using electronic inks of 2D molybdenum oxide nanoflakes. Adv. Funct. Mater. **2016,** 26 (1), 91-100.

11. Novoselov, K. S., *et al*., Electric field effect in atomically thin carbon films. Science **2004,** 306 (5696), 666-669.

12. Amara, K. K., *et al.*, Wet chemical thinning of molybdenum disulfide down to its monolayer. APL Mater. **2014,** 2 (9), 092509.

13. Castellanos-Gomez, A., *et al.*, Laser-thinning of MoS_2: On demand generation of a single-layer semiconductor. Nano Letters **2012,** 12 (6), 3187-3192.

14. Huang, Y., *et al*., An innovative way of etching MoS_2: Characterization and mechanistic investigation. Nano Research **2013,** 6 (3), 200-207.

15. Whitener Jr, K. E.; Sheehan, P. E., Graphene synthesis. Diam. Relat. Mater. **2014,** 46, 25-34.

16. Yi-Kai Huang, *et al*., Evaporative thinning: A facile synthesis method for high quality ultrathin layers of 2D crystals. ACS nano **2014,** 8 (10), 10851-10857.

17. Zeng, H. C., Chemical etching of Molybdenum Trioxide: A new tailor-made synthesis of MoO_3 catalysts. Inorg. Chem. **1998,** 37, 1967-1973.

18. Huang, P.-R., *et al*., Impact of lattice distortion and electron doping on α-MoO_3 electronic structure. Sci. Rep. **2014,** 4, 7131.

19. Lee, S.-H., *et al*., Raman spectroscopic studies of electrochromic a-MoO_3 thin films. Solid State Ionics **2002,** 147, 129-133.

20. Mai, L., *et al*., Lithiated MoO_3 nanobelts with greatly improved performance for lithium batteries. Adv. Mater. **2007,** 19 (21), 3712-3716.

21. Ou, J. Z., *et al*., In situ Raman spectroscopy of H_2 gas interaction with layered MoO_3. J. Phys. Chem. C **2011,** 115 (21), 10757-10763.

22. Radisavljevic B, *et al*., Single-layer MoS_2 transistors. Nat. Nano. **2011,** 6 (3), 147-150.

Chapter 4 : REVERSIBLE RESISTIVE SWITCHING BEHAVIOUR IN LAYERED MoO_x

Memristors have the potential for use in future-generation memory applications. In this chapter, the characterisation of MoO_3-based memory cells is presented. MoO_3 is a potential two-dimensional transition metal oxide with enhanced electronic transport properties, and it can be easily tuned via the manipulation of its stoichiometry. Hence, exploiting the planar form of sub-stoichiometric MoO_3 in its multi-oxidation states has the potential to offer higher switching ratio and low power-resistive memory elements. Extensive characterisation has been carried out on the as-grown material to study the chemical composition and crystalline structure of the material. The suitability of the material in non-volatile memory applications was experimentally assessed via cyclic repeatability and memory retention tests.

4.1 Introduction

Existing Si-based technologies for the current computing systems has reached their physical limits, as the modern devices demand efficient and high-density electronics.[1] Resistive memory devices or memristors are two-terminal 'memory resistors' that can store information in the form of resistance states. The resistive states of such a device rely on the history of applied voltage and can be reversibly switched.[2] In theory, non-volatile resistive memory technology holds potential,[3-5] as it possesses superior features; including non-volatile electrical switching, longer memory retention, high data density and compatibility with contemporary complementary metal oxide semiconductor (CMOS) technology.[6-8] They

can also be easily scaled down to less than 10 nm,[6] and offer ease of fabrication.[9] Several metal oxides such as, TiO_2,[10-13] WO_3,[14] VO_2,[15] STO,[16-19] ZnO,[20] TaO_2[21] and HfO_2 [22-23] have been used as the active material, which exhibit reversible resistive switching behaviours. Among them, high dielectric binary metal oxides such as, TiO_2, TaO_2, HfO_2 have been extensively studied as resistive switching layers for CMOS technology. High dielectric oxide layers have the potential to suppress sneak path current and undesirable parasitic effects during resistive switching performance. However, there are several drawbacks such as high electroforming voltage and in other cases; poor memory retention and switching ratios are observed. As the field is still at its infancy, significant progress is yet to be made, in order to integrate memristor technology into the existing CMOS based nano-electronics. As such, to realise practical resistive memory devices, a versatile material with multiple stable stoichiometries that offers high switching ratios is essential.

Molybdenum oxide (MoO_x) is a potential two-dimensional transition metal oxide with enhanced electronic transport properties, which can be easily tuned via the manipulation of its stoichiometry.[24-25] MoO_x can be obtained in two stable states, MoO_2 and MoO_3. MoO_2 is the lowest oxidation state Mo^{4+}, which exists as a distorted rutile-type monoclinic structure and shows semi-metallic properties. On the other hand, the highest oxidation state of MoO_3 is a wide bandgap semiconductor that occurs in an orthorhombic-layered structure. In-between exists the oxygen-deficient intermediate state MoO_{3-x}, that can be tuned to behave anywhere from semi-metallic to insulating. The multitude of stable stoichiometries of MoO_x along with high thermodynamic stability renders it ideal for resistive memory applications. To date, resistive memory behaviour of bulk MoO_3 composites have been studied.[26-29] However, exploiting the planar form of non-stoichiometric MoO_x in its multi-oxidation states has the potential to offer higher switching ratio, and low power resistive memory elements.

In this work, CVD grown thin layers (~25 nm) of MoO_x has been introduced as a resistive switching oxide for non-volatile memory applications, in cross-planar device architecture. Extensive characterisation has been carried out on the as-grown material to establish the chemical composition and crystalline structure. The suitability of the material in non-volatile memory applications has been experimentally assessed via cyclic repeatability and memory retention tests.

4.2 Experimental Section

4.2.1 CVD growth of MoO_x

MoO_x film with thickness of 25-30 nm was deposited on patterned bottom Pt/Ti electrodes on SiO_2/Si substrates using chemical vapour deposition at 530 °C. The precursor (MoO_3 powder, 5 mg) was placed in the middle zone (785 °C) of a horizontal 3-zone furnace. The growth substrates were placed downstream in the third zone, at 530 °C. Argon was used as the carrier gas at a rate of 100 sccm and a chamber pressure of 300 mT has been maintained. The furnace was ramped up to the set temperatures in 50 minutes and then maintained the set temperatures for 10 minutes for the reaction to occur. Thereafter, the furnace was allowed to cool down naturally. A table comparing the growth conditions of crystalline MoO_3 from existing literature is presented in appendix B.

4.2.2 Material characterisation

The thickness of MoO_x layer was measured using Dimension Icon Bruker atomic force microscope under ScanAsyst Air mode. LabRam HR Evolution Raman Spectrometer

(laser excitation of 532 nm with a 50× objective) has been utilised to assess the composition of the as-grown MoO_x, prior to device fabrication. X-ray diffractograms were collected using a Bruker D4 Endeavor XRD instrument with monochromatic Cu Kα as radiation source, within an angular range 2θ from 20° to 60°. X-ray photoelectron spectroscopy was performed using a Thermo Scientific K-alpha X-ray Photoelectron Spectrometer with an Al Kα radiation source with energy of 1485 eV. Adventitious carbon peak at 284.8 eV has been used as the calibration reference for fitting of the core level spectra of the principal elements. A FEI Nova NanoSEM has been utilised to characterise the morphology of the devices after patterning top electrode.

TEM lamella samples have been prepared using focused ion beam milling in a FEI Scios DualbeamTM scanning electron microscope. Cross-sectional analysis and energy-dispersive X-ray spectroscopy are performed on a JEOL 2100F scanning transmission electron microscope (STEM) with attached Tridium Gatan image filter.

4.2.3 Cross-point device fabrication

MoO_x memory devices in cross-point configuration (square overlap areas with sides of 2-40 μm) were fabricated on SiO_2/Si substrates, using a three-step photolithography and lift-off process. Metal thin films of 30 nm Pt with a 5 nm Ti adhesion layer were deposited as bottom electrodes via electron beam evaporation at room temperature. Subsequently, MoO_x was deposited over the bottom electrodes using a CVD process. Typically, de-wetting of Pt is initiated at temperatures higher than 600 °C,[30] which is much higher than the deposition temperature of MoO_x (530 °C) in this work. As such, it is confirmed that the de-wetting does

not occur on the bottom electrode. Thereafter, top electrodes of 30 nm Pt (with a 10 nm Ti adhesion layer) were deposited via electron beam evaporation. Finally, photolithography and selective MoO_x etching was utilised to reveal the bottom electrode pads, for electrical characterisation.

4.2.4 Electrical characterisation

Two-terminal electrical characterisation was performed using an Agilent B2912A source with a micromanipulator probe station. Bipolar current–voltage (*I–V*) sweep cycles, memory retention and cyclic endurance tests were performed on the fabricated devices. All electrical characterisations were performed by applying a bias voltage to the bottom electrode with the top electrode being grounded.

4.3 Results and Discussion

AFM has been utilised to measure the thickness of the CVD grown oxide films. In order to measure the step thickness of the as grown film, photolithography and subsequent selective area etching of MoO_x, was carried out.[24] Figure 4.1a shows the AFM image and the thickness profile of the as-deposited material. The thickness profile revealed that the as-grown material is ~25 nm thick (Figure 4.1a). Raman spectroscopy has been employed to assess the chemical composition of the as-grown oxide layer. Figure 4.1b shows the micro-Raman spectrum of the CVD grown film, in which Raman signature peaks corresponding to MoO_x (MoO_2, MoO_{3-x} and MoO_3) were identified. The low intensity characteristic peaks at 356 cm^{-1} and 732 cm^{-1} confirm the presence of an intermediate oxidation state (MoO_{3-x}) indicative of localised Mo^{5+}, produced due to oxygen vacancies.[31-32] The high intensity peak at 201 cm^{-1} and relatively lower intensity peaks at 493 cm^{-1} and 567 cm^{-1} suggest the presence of Mo^{4+} in

the as-grown material.[31, 33] Peaks observed at 820 cm^{-1} and 995 cm^{-1} can be correlated to the Mo^{6+} oxidation state of α-MoO_3.[31, 34] The Raman analysis indicates that a mixture of molybdenum oxide species (Mo^{4+}, Mo^{5+}, and Mo^{6+}) are present in the as-deposited film.

To further analyse the compositional ratio of the oxide species, high resolution X-ray photoemission spectroscopy (XPS) measurements were carried out (Figure 4.1c). Adventitious carbon C 1s peak at 284.8 eV has been taken as a reference which shows no charge shifting.[35] The presence of C 1s peak is due to the expected carbon contamination from the environment. Typically, a Mo 3d-doublet with a spin-orbit component of Mo $3d_{5/2}$ and Mo $3d_{3/2}$ is associated with a single oxidation state in molybdenum oxides. The de-convolution and the curve fitting of the XPS spectrum reveals that Mo 3d spectrum can be well fitted with three sets of 3d doublets in the form of a Gaussian function, which are corresponding to three oxidation states of Mo. The peak fitting has been done with a fixed energy gap of 3.2 eV for the doublet of spin-orbit coupling peaks. The convoluted peaks also show that the ratio of the integral areas between two doublets is 3:2 and have the same full width at half maximum (FWHM) values for each doublet.[34, 36] The binding energy values corresponding to 232.7 eV (Mo $3d_{5/2}$) and 235.9 eV (Mo $3d_{3/2}$) are characteristics of oxidation state of Mo^{6+}.[37-38] Whereas, the peaks at 229.4 eV (Mo $3d_{5/2}$) and 232.6 eV (Mo $3d_{3/2}$) are assigned to Mo^{4+} oxidation state.[39] In addition, a third pair of doublets at 231.3 eV (Mo $3d_{5/2}$) and 234.5 eV (Mo $3d_{3/2}$) corresponding to Mo^{5+} are also observed.[40] Based on the XPS analysis, it can be concluded that the as-deposited material is a combination of multiple oxidation states of Mo (26% Mo^{4+}, 46% Mo^{5+} and 28% Mo^{6+}). The calculated atomic mass percentages of each oxidation state and their corresponding binding energy values are listed in Table 1.

Table 4 1 Binding energy values for Mo 3d spin-orbit component of molybdenum oxide at various oxidation states

Oxidation state	Binding Energy value (eV)		Concentration (Atomic%)
	$Mo3d_{5/2}$	$Mo3d_{3/2}$	
Mo^{4+}	229.4	232.6	26%
Mo^{5+}	231.3	234.4	46%
Mo^{6+}	232.7	235.9	28%

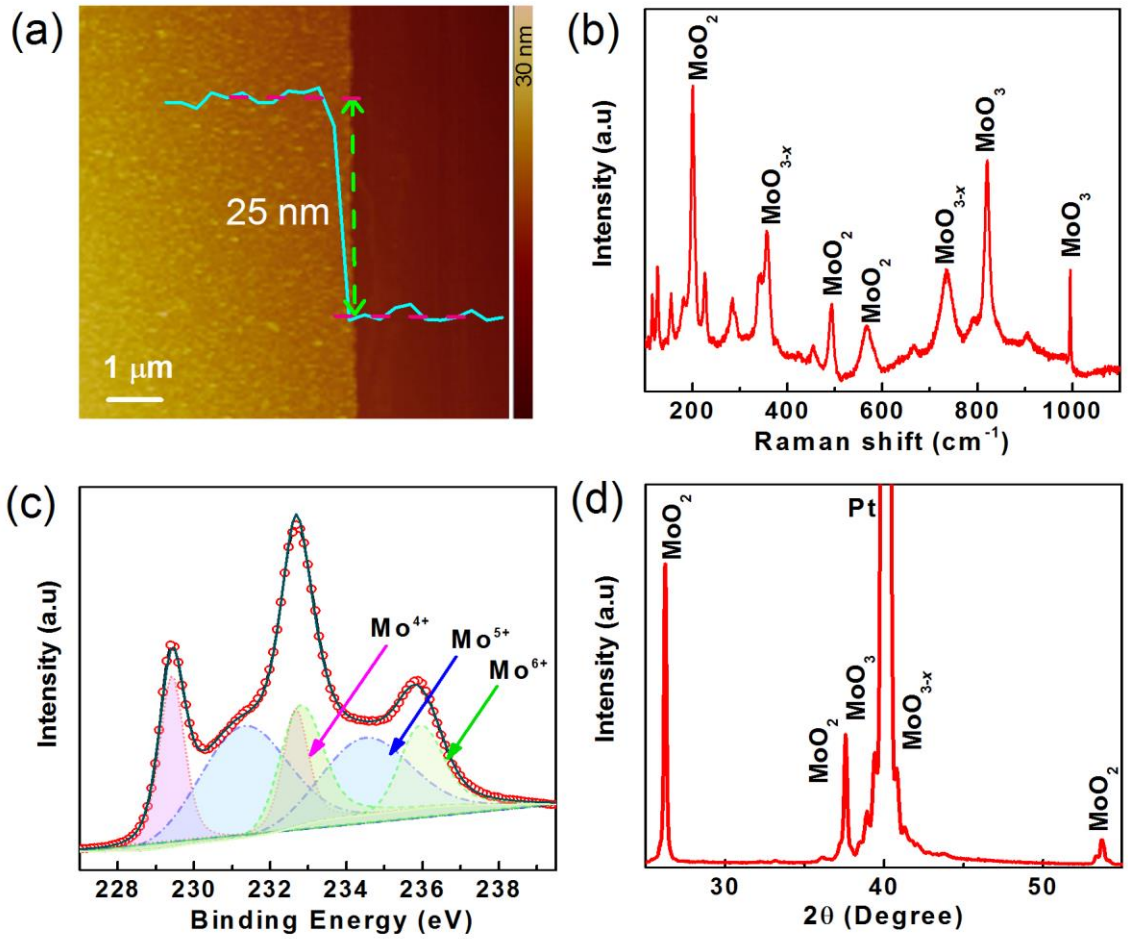

Figure 4.1 Characterisation of chemical vapour deposition grown MoO_x: (a) Atomic force micrograph with the cross-sectional thickness profile, (b) micro-Raman spectra, (c) X-ray photoelectron spectra of Mo 3d XPS peaks with fitted spin-orbit components, and (d) X-ray diffractogram.

To investigate the crystallinity of the as-grown material, X-ray diffraction (XRD) patterns were recorded (Figure 4.1d). The diffractogram shows two dominant peaks at 26.1° and 37.5°, corresponding to (011) and (002) planes, respectively, of monoclinic MoO_2 (JCPDS No. 78-1070).[41-42] There are two comparatively low intensity peaks at 38.9° and 40.6° correspond to (060) plane of MoO_3 (JCPDS No. 05-0508) and (203) plane of MoO_{3-x} (JCPDS No. 05-0337), respectively. The XRD patterns indicate a dominant presence of monoclinic MoO_2 co-existing with MoO_{3-x} and MoO_3, further validating the conclusions derived from the

Raman and XPS analyses. However, once the material is subject to electric fields (an electroforming process), it transforms to predominantly MoO_{3-x} (discussed later).

Typically, resistive states of the memristors are electrically manipulated by controlling conductive filaments that are composed of oxygen vacancies. Since the oxygen vacancies are widely dispersed in metal oxides, an application of a large electric field across the material is required for the initial formation of conductive filaments (electroforming process). Upon electroforming, the material switches from a high resistive state (HRS) to a low resistive state (LRS). Subsequently, depending on the polarity of the applied electric field, the oxygen vacancies can be scattered to rupture the conductive paths (to achieve HRS) or concentrated to re-form conductive filaments (to achieve LRS).[10, 16, 43-45] Owing to the formation and rupture of the conductive filaments, a reversible behaviour in the resistive state of the material can be observed. The current–voltage (*I*–*V*) characteristics curve of such a device exhibits a pinched hysteresis trend, illustrating the reversible switching between the low and high resistive states of the material.

Cross-point memory cells were fabricated on large area CVD grown MoO_x (see experimental section). Figure 4.2a shows a schematic illustration of the Pt/Ti/MoO_x/Pt/Ti cross-point memory cell while Figure 4.2b and c, present optical and scanning electron micrographs of an as fabricated device, respectively. To electroform the as-fabricated devices, a set of positive bias (0 to +5 V) and subsequent negative bias was applied across the bottom and top electrodes. A current compliance limit of 800 µA was set to prevent any dielectric breakdown of the device. The electroforming process was observed to take place at an applied voltage of -2.7 V, where the device resistance was reduced by several orders of magnitude.

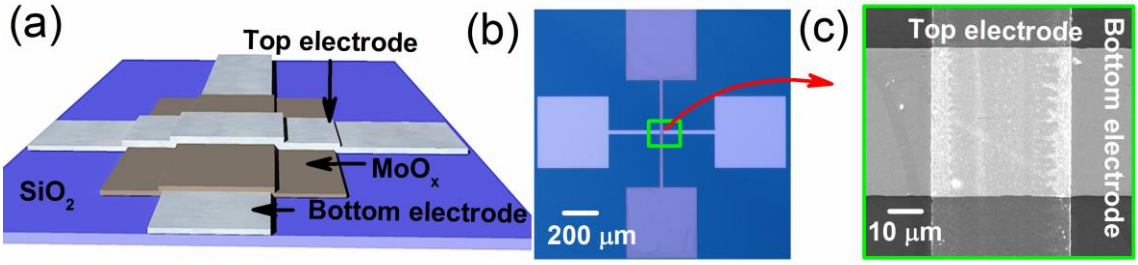

Figure 4.2 (a) Schematic illustration of the cross-point memristor device architecture. (b) Optical and (c) scanning electron micrographs of an as-fabricated memristor.

Following the electroforming process, several cycles of bipolar switching voltage were applied, and the devices show reversible resistive switching behaviour over multiple cycles. Figure 4.3a shows the electrical characteristics of an electroformed memory cell, when subjected to voltage sweeps of -2.0 V to +2.5 V. Minor fluctuations in threshold voltages are observed in the pinched hysteresis loops. Such negligible fluctuations are attributed to the variations in I_{HRS}, which is caused by the existence of conductive filamentary paths that can survive the RESET process, and the stochastic nature of filament formation.[46] Figure 4.3b shows the statistical distribution of the switching voltages (V_{SET} and V_{RESET}), observed in the cyclic switching results presented in Figure 4.3a. The V_{SET} ranges from -0.7 to -1.3 V with a mean value of -1.09 V and the V_{RESET} ranges from +2.2 to +2.6 V with a mean value of +2.3 V. The stability of the resistive states was measured over a long period of time, to acquire the memory retention characteristics of the electroformed devices. Figure 4.3c shows the stability of the resistive states for durations of over 10^4 s, at room temperature. Here, the ON/OFF ratio was consistently maintained above 10^3 without any deterioration, at a read voltage of 500mV. As such the retention test reveals robust non-volatile behaviour of the devices and reliability of the material for memory applications. Electrical endurance tests were performed at room temperature to evaluate the cycle-to-cycle stability and reproducibility of MoO_x-

based devices. The current values (I_{LRS} and I_{HRS}) of a memory cell were extracted at a read voltage of 500 mV, while the device was subjected to a train pulse of (2 ms pulse width) alternating write and erase cycles (Figure 4.3d). The associated energies for SET and RESET switching were computed to be 6.7 µJ to 18 nJ range during the pulse. Further details on the train pulse during endurance performance and the computed energy consumption are presented in Appendix B. The device was observed to have successfully retained the two distinct resistance states for >6000 repetitive cycles while maintaining a switching ratio of ~10^3. Within the LRS and HRS, the resistance values appear to be dispersive. Such behaviour suggests that the switching is caused by several filamentary paths.[46] Endurance failure in such devices is caused by Joule heating and repetitive redox reactions leading to the formation of permanent filamentary paths, at which point the devices continue to remain in their LRS. A quantitative comparison resistive switching performance of various 2D memristors has been presented in Appendix B. Further, a table representing multiple device performance is presented in Appendix B.

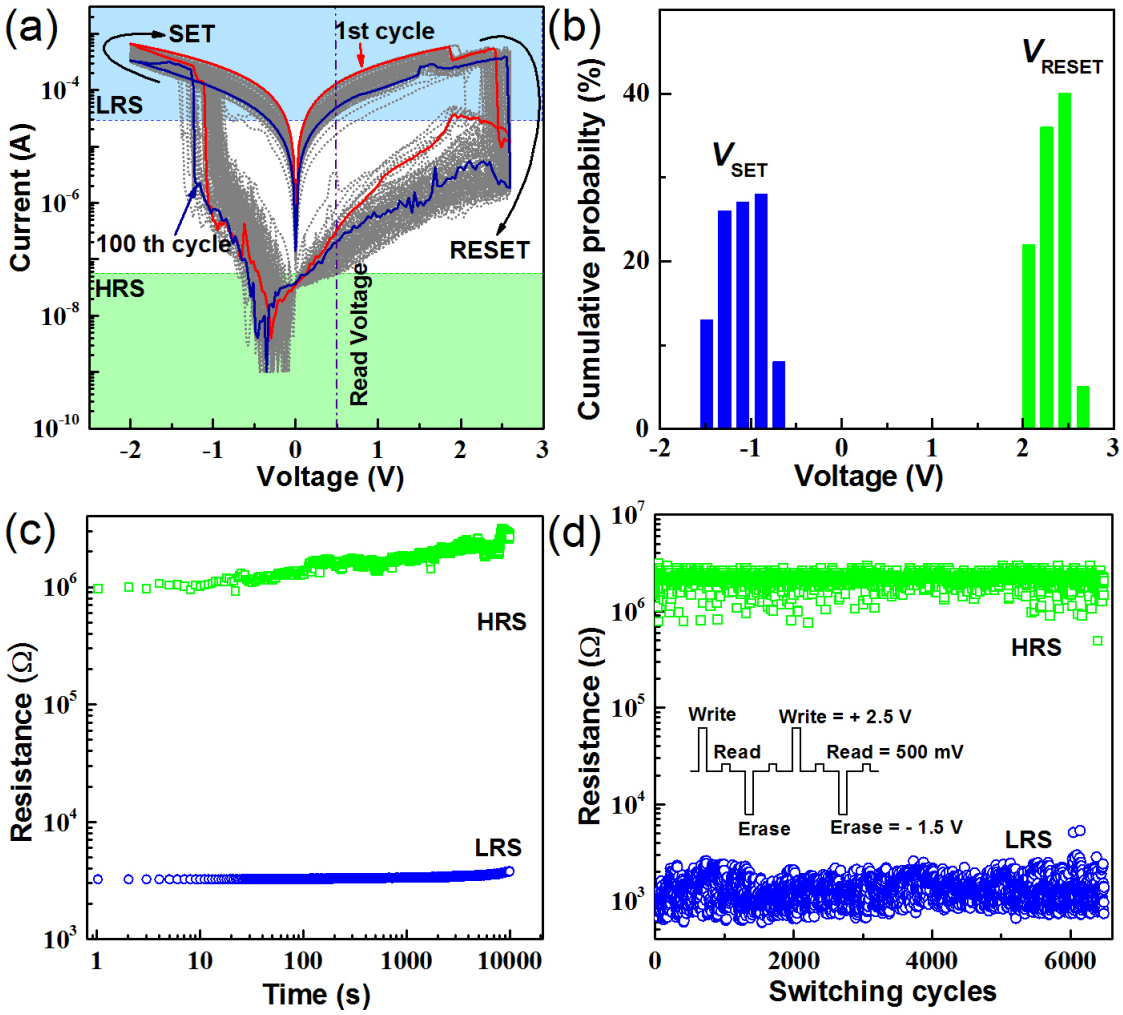

Figure 4.3 switching cycles. (b) Statistical analysis of the switching voltages over 100 switching cycles. (c) Retention of the resistive state with respect to time. (d) Performance endurance with respect to number of switching cycles. (Resistance values obtained at a read voltage of 500 mV). Inset shows the voltage pulse train during endurance measurement with duration of 2 ms of each pulse.

To understand the charge transfer and switching mechanism in the MoO_x memory clearly, *I-V* characteristics curves are plotted on a double logarithmic scale. Figure 4a, b show the *I-V* curves for both positive and negative biasing. The characteristics curve shows Ohmic conduction behaviour ($I \infty V$)[47-48] in LRS region for both positive and negative biasing. The *I-V* characteristics curve in HRS during positive biasing, shows $I \infty V$ relationship at lower voltages and $I \infty V^{\geq 2}$ at higher voltages, indicating a space charge limited conduction (SCLC) mechanism.[49] The HRS region during negative biasing can be divided in to two parts. In the

lower voltage region, the current decreases with an increase in applied voltage, which suggests the existence of a reverse built-in electric field.[50-52] This is attributed to the interfacial Ti layer, which has a tendency to oxidise, creating a reverse built in potential near the top electrode interface. Once this voltage is breached, the current then increases with an increasing bias voltage, which is in good agreement with SCLC mechanism.

Based on the above results, a physical model of oxygen vacancy migration and filaments formation has been developed and a schematic illustration of the resistive switching mechanism is presented in Figure 4.4c. The pristine MoO_x cells contain randomly distributed positively charged oxygen vacancies (the presence of Mo^{5+}),[53] which act as mobile donors in the oxide layers.[54] As the applied voltage increases, the oxygen vacancies present in the oxide layers migrate in the direction of applied field and accumulate near the bottom electrode. Eventually this oxygen deficient region forms single/multiple conductive filaments between the electrodes, leading to LRS of the material. Subsequently, a positive bias at the bottom electrode (Pt) repels the oxygen vacancies from the electrode, resulting in the partial rupture of the conductive filaments. Consequently, the memory cell reverts back to a HRS between the electrodes (RESET). Conversely, a smaller negative bias (relative to the electroforming voltage), enables the reformation of the filaments and allow the cell to switch back to a LRS (SET). As such, the partial rupture and the reformation of filaments composed of oxygen vacancies, result in the resistive switching of layered MoO_x.

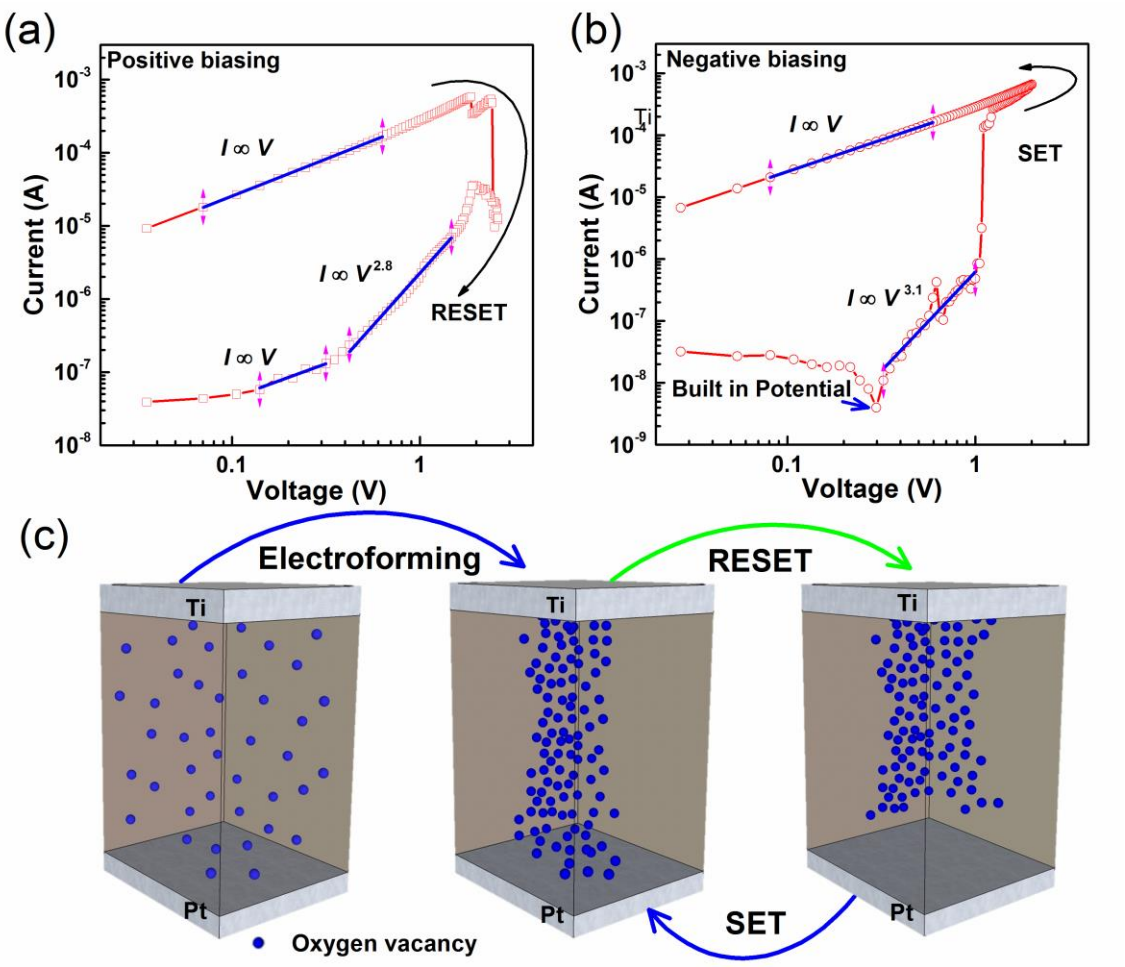

Figure 4.4 *I-V* characteristics curves of both (a) positive and (b) negative bias regions of the MoO_x memory device, plotted in a double-logarithmic scale. Both LRS and HRS are included on this plot. (c) Schematic illustration of electroforming and subsequent switching mechanisms in MoO_x memory cells. Bottom electrode is biased and the top electrode remains grounded.

To analyse the structural integrity of the resistive memory cells, cross-sectional high-resolution transmission electron microscopy (HRTEM) of pristine and electroformed memory cells was undertaken (Figure 4.5). The MIM interface can be clearly identified on the HRTEM images for both the pristine and electroformed devices. The HRTEM image of a pristine memory cell reveals the presence of both polycrystalline and amorphous phases in the MoO_x stack (inset of Figure 4.5a). For the compositional analysis of the distinct phases,

three regions of interest (ROIs) were selected (highlighted in Figure 4.5a). The fast Fourier transform (FFT) diffraction pattern of the first ROI shows the amorphous nature of the film. In the other two distinct ROIs, (001) plane of α-MoO_3 and (002) plane of MoO_2 were identified. This agrees with the XPS characterisations confirming the existence of multiple oxidation states in the metal oxide layer (MoO_3, MoO_{3-x}, and MoO_2). However, the cross-sectional HRTEM image of the electroformed device reveals only one type of crystalline structure, corresponding to MoO_3/MoO_{3-x} (Figure 4.5b). Inset at the top shows the FFT diffraction pattern of the selected ROI. The diffraction spots with d-spacing 0.36 nm are indexed to (001) plane corresponding to orthorhombic MoO_3/MoO_{3-x}. The phase change of the material suggests that the process of electroforming predominantly oxidises the Mo^{4+} to Mo^{5+}/Mo^{6+} states. The diffraction patterns corresponding to (001) are used to generate the inverse FFT, which highlights the dominant existence of MoO_3/MoO_{3-x}, in the ROI (Figure 4.5b, bottom right inset). A further analysis on the inverse FFT of the cross-sectional area (pre- and post-electroformed cell) is presented in Appendix B. Utilising ImageJ, it is determined that the 72.50% of the pristine cell is crystalline MoO_3/MoO_2 and 94.11% of the electroformed cell remains crystalline sub-stoichiometric MoO_3. Such a transition is expected, as the lower oxidation states (Mo^{4+}) get oxidised into higher states (Mo^{5+}/Mo^{6+}), due to Joule heating induced by the localized electrical stress. Based on the TEM analyses, it can be conferred that the applied electric field, changes the material composition from its multi-oxidation state to a sub-stoichiometric form of MoO_3.

To ensure the integrity of the MIM architecture post electroforming, an elemental analysis on the cross section of the devices was carried out using energy dispersive spectroscopy (EDS). Cross-sectional scanning transmission electron microscopy (STEM) image and the corresponding elemental EDS maps carried out on a pristine (Figure 4.5c) and an

electroformed device (Figure 4.5d) are presented. The MIM structure was well maintained pre- and post-electroforming process, with no diffusion of metal observed through the oxide (Pt/Ti/MoO_x/Pt/Ti). Slight overlap of the elements in the interfacial region is attributed to the localised Joule heating and the resolution of the imaging technique. It is inaccurate to draw a conclusion from the oxygen map, as the cross-sectional sample preparation involves high-energy focussed ion beam milling process, which typically results in oxygen contamination. Based on these results, metal diffusion is eliminated as a contributing factor in the switching process and the MoO_x layer is concluded as the sole contributor to the observed resistive switching.

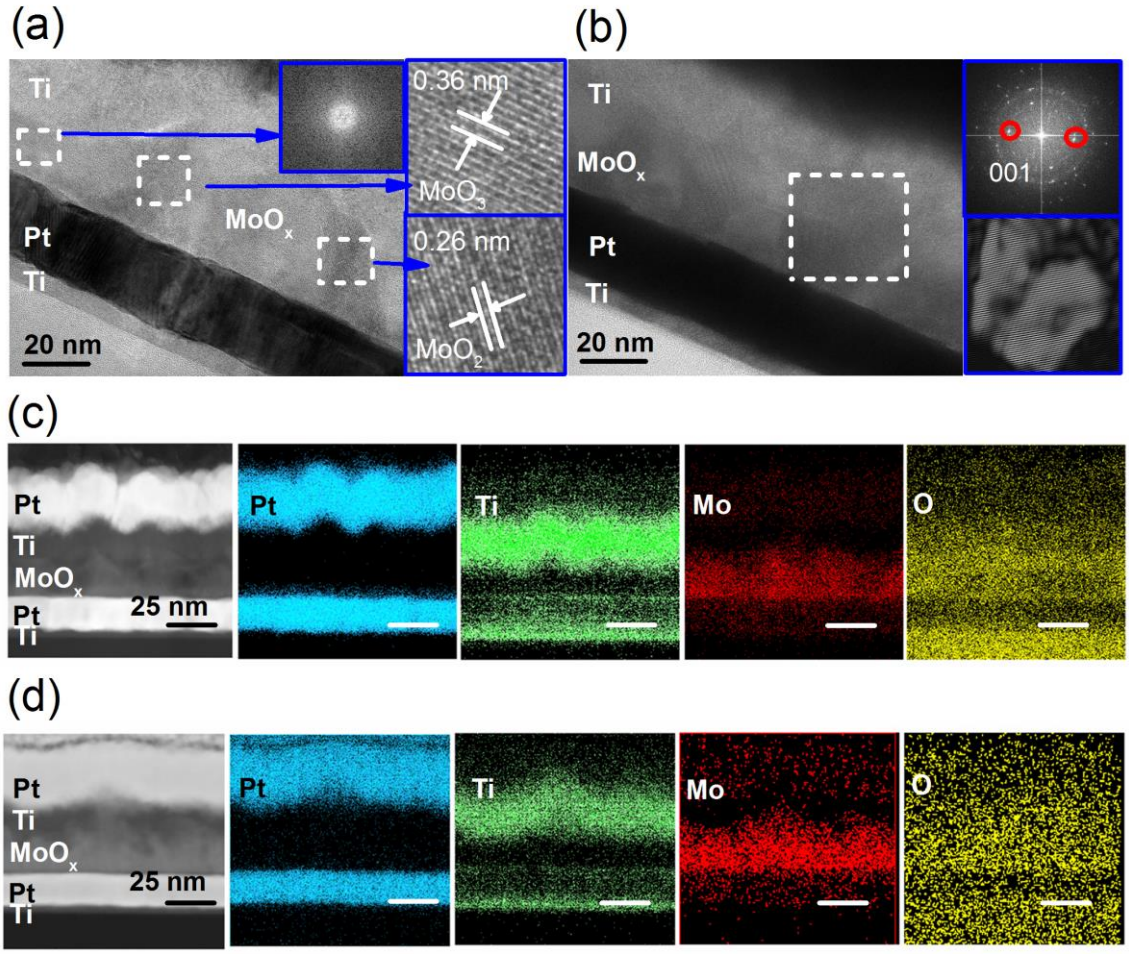

Figure 4.5 Structural analyses of a pristine and an electroformed device. (a) The cross-sectional HRTEM image of a pristine cell. Insets showing different lattice parameters indicating the co-existence of multi-oxidation state of molybdenum oxide (MoO_2 and MoO_3). (b) HRTEM image of an electroformed cell. Insets are the FFT image and inverse FFT of the ROI in (b). The cross-sectional EDS elemental maps of (c) a pristine device cell

4.4 Conclusions

In conclusion, resistive switching behaviour has been demonstrated in CVD grown ultra-thin MoO_x films. The switching performance of cross-point MoO_x memory devices are driven by the presence of oxygen vacancies, due to the various oxidation states co-existing in the as-grown material. The composition of the as-grown MoO_x films are thoroughly characterised

through multiple spectroscopic techniques. However, it is found that post electroforming, the material composition changes to an oxygen-deficient MoO_{3-x} film. The room temperature memory retention tests show high ON/OFF ratios exceeding ~10^3 for durations over 10^4 s. The cyclic endurance of the memory devices shows that they remain stable over 6000 cycles, while maintaining a switching ratio of ~10^3. The devices also exhibit relatively lower electroforming voltages (~2.7 V) in comparison to other high dielectric metal oxides. As such, this work showcases the adaptability of MoO_x nanofilms, in non-volatile resistive memory applications for future integrated two-dimensional electronics.

4.5 References

1. Kingon, A. I., *et al.*, Alternative dielectrics to silicon dioxide for memory and logic devices. Nature **2000,** 406 (6799), 1032-1038.

2. Waser, R., *et al.*, Redox-based resistive switching memories - Nanoionic mechanisms, prospects, and challenges. Adv. Mater. **2009,** 21 (25-26), 2632-2663.

3. Sawa, A., Resistive switching in transition metal oxides. Mater. Today **2008,** 11 (6), 28-36.

4. Kim, K. M., *et al.*, Nanofilamentary resistive switching in binary oxide system; a review on the present status and outlook. Nanotechnology **2011,** 22 (25), 254002.

5. Yoshihisa, F., Review of emerging new solid-state non-volatile memories. Jpn. J. Appl. Phys. **2013,** 52 (4R), 040001.

6. Mohammad, B., *et al*., State of the art of metal oxide memristor devices. Nanotechnol. Rev. **2016,** 5 (3), 311-329.

7. Sangwan, V. K., *et al*., Gate-tunable memristive phenomena mediated by grain boundaries in single-layer MoS_2. Nat. Nanotechnol. **2015,** 10 (5), 403-406.

8. Cheng, P., *et al*., Memristive behavior and ideal memristor of 1T phase MoS_2 nanosheets. Nano Lett. **2016,** 16 (1), 572-576.

9. Liang, L., *et al*., Vacancy associates-rich ultrathin nanosheets for high performance and flexible nonvolatile memory device. J. Am. Chem. Soc. **2015,** 137 (8), 3102-8.

10. Pickett, M. D., *et al*., Switching dynamics in titanium dioxide memristive devices. J. Appl. Phys. **2009,** 106 (7), 074508.

11. Xia, Q., *et al*., Impact of geometry on the performance of memristive nanodevices. Nanotechnology **2011,** 22 (25), 254026.

12. Yang, J. J., *et al*., The mechanism of electroforming of metal oxide memristive switches. Nanotechnology **2009,** 20(21), 215201.

13. Huang, J.-J., *et al*., Transition of stable rectification to resistive-switching in $Ti/TiO_2/Pt$ oxide diode. Appl. Phys. Lett. **2010,** 96 (26), 262901.

14. Qu, B., *et al*., Recent progress in tungsten oxides based memristors and their neuromorphological applications. Electron. Mater. Lett. **2016,** 12 (6), 715-731.

15. Hota, M. K., *et al*., Electroforming free resistive switching memory in two-dimensional VO_x nanosheets. Appl. Phys. Lett. **2015,** 107 (16), 163106.

16. Nili, H., *et al*., Nanoscale resistive switching in amorphous perovskite oxide (a-$SrTiO_3$) memristors. Adv. Funct. Mater. **2014,** 24 (43), 6741-6750.

17. Nili, H., *et al*., Donor-induced performance tuning of amorphous $SrTiO_3$ memristive nanodevices: Multistate resistive switching and mechanical tunability. Adv. Funct. Mater. **2015,** 25 (21), 3172-3182.

18. Nili, H., *et al*., Microstructure and dynamics of vacancy-induced nanofilamentary switching network in donor doped $SrTiO_{3-x}$ memristors. Nanotechnology **2016,** 27 (50), 505210.

19. Ahmed, T., *et al*., Transparent amorphous strontium titanate resistive memories with transient photo-response. Nanoscale **2017,** 9 (38), 14690-14702.

20. Qi, J., *et al*., Multimode resistive switching in single ZnO nanoisland system. Sci. Rep. **2013,** 3, 2405.

21. Zongwei, W., *et al*., Modulation of nonlinear resistive switching behavior of a TaO_x-based resistive device through interface engineering. Nanotechnology **2017,** 28 (5), 055204.

22. He, W., *et al*., Customized binary and multi-level HfO_{2-x}-based memristors tuned by oxidation conditions. Sci. Rep. **2017,** 7 (1), 10070.

23. Chen, Y. S., *et al*., Well controlled multiple resistive switching states in the Al local doped HfO_2 resistive random access memory device. J. Appl. Phys. **2013,** 113 (16), 164507.

24. Rahman, F., *et al.*, Two-dimensional MoO_3 via a top-down chemical thinning route. 2D Mater. **2017,** 4 (3), 035008.

25. Balendhran, S., *et al*., Enhanced charge carrier mobility in two-dimensional high dielectric molybdenum oxide. Adv. Mater. **2013,** 25 (1), 109-114.

26. Tan, Z.-H., *et al*., One-dimensional memristive device based on MoO_3 nanobelt. Appl. Phys. Lett. **2015,** 106 (2), 023503.

27. Lee, D., *et al*., Resistance switching of copper doped MoO_x films for nonvolatile memory applications. Appl. Phys. Lett. **2007,** 90 (12), 122104.

28. M Arita, H. K., T. Fujii, Y. Takahashi, Resistance switching properties of molybdenum oxide films. Thin Solid Films **2012,** 520, 4762-4767.

29. Bessonov, A. A., *et al*., Layered memristive and memcapacitive switches for printable electronics. Nat. Mater. **2015,** 14 (2), 199-204.

30. Lee, J.-M.; Kim, B.-I., Thermal dewetting of Pt thin film: Etch-masks for the fabrication of semiconductor nanostructures. Mater. Sci. Eng. A **2007,** 449-451, 769-773.

31. Camacho-López, M. A., *et al*., Micro-Raman study of the m-MoO_2 to α-MoO_3 transformation induced by cw-laser irradiation. Opt. Mater. **2011,** 33 (3), 480-484.

32. Pham, D. V., *et al*., Doping-free bandgap tuning in one-dimensional Magneli-phase nanorods of Mo_4O_{11}. Nanoscale **2016,** 8 (10), 5559-5566.

33. Spevack, P.; McIntyre, N., Thermal reduction of MoO_3. J. Phys. Chem. **1992,** 96 (22), 9029-9035.

34. Hu, X. K., *et al*., Comparative study on MoO_3 and H_xMoO_3 nanobelts: Structure and electric transport. Chem. Mater. **2008,** 20 (4), 1527-1533.

35. Spevack, P. A.; McIntyre, N. S., A Raman and XPS investigation of supported molybdenum oxide thin films. 1. Calcination and reduction studies. J. Phys. Chem. **1993,** 97 (42), 11020-11030.

36. Wang, C., *et al*., Role of molybdenum oxide for organic electronics: Surface analytical studies. J. Vac. Sci. Technol. B **2014,** 32 (4), 040801.

37. Scanlon, D. O., *et al*., Theoretical and experimental study of the electronic structures of MoO_3 and MoO_2. J. Phys. Chem. C **2010,** 114 (10), 4636-4645.

38. Choi, J. G.; Thompson, L. T., XPS study of as-prepared and reduced molybdenum oxides. Appl. Surf. Sci. **1996,** 93 (2), 143-149.

39. Baltrusaitis, J., *et al*., Generalized molybdenum oxide surface chemical state XPS determination via informed amorphous sample model. Appl. Surf. Sci. **2015,** 326, 151-161.

40. Sunu, S. S., *et al*., Electrical conductivity and gas sensing properties of MoO_3. Sens. Actuators, B **2004,** 101 (1-2), 161-174.

41. Hao, S., *et al*., Chemical vapor deposition growth and characterization of drop-like MoS_2/MoO_2 granular films. Phys. Status Solidi B **2017,** 254 (4), 1600245.

42. Kumari, L., *et al*., X-ray diffraction and Raman scattering studies on large-area array and nanobranched structure of 1D MoO_2 nanorods. Nanotechnology **2007,** 18 (11), 115717.

43. Ielmini, D., Resistive switching memories based on metal oxides: mechanisms, reliability and scaling. Semicond. Sci. Technol. **2016,** 31 (6), 063002.

44. Zongwei, W., *et al*., Modulation of nonlinear resistive switching behavior of a TaO_x-based resistive device through interface engineering. Nanotechnology **2017,** 28 (5), 055204.

45. Chen, J.-Y., *et al*., Switching kinetic of VCM-based memristor: Evolution and positioning of nanofilament. Adv. Mater. **2015,** 27 (34), 5028-5033.

46. Efeoglu, H., *et al*., Resistive switching of reactive sputtered TiO_2 based memristor in crossbar geometry. Appl. Surf. Sci. **2015,** 350, 10-13.

47. Lim, E.; Ismail, R., Conduction mechanism of valence change resistive switching memory: A survey. Electronics **2015,** 4 (3), 586.

48. Zhou, G., *et al*., Coexistence of negative differential resistance and resistive switching memory at room temperature in TiO_x modulated by moisture. Adv. Electron. Mater. **2018,** 4(4), 1700567.

49. Wang, S.-Y., *et al*., Multilevel resistive switching in Ti/Cu_xO/Pt memory devices. J. Appl. Phys. **2010,** 108 (11), 114110.

50. Xu, Z., *et al*., Low-energy resistive random access memory devices with no need for a compliance current. Sci. Rep. **2015,** 5, 10409.

51. Valov, I., *et al*., Nanobatteries in redox-based resistive switches require extension of memristor theory. Nat. Commun. **2013,** 4, 1771.

52. Gao, S., *et al*., Dynamic processes of resistive switching in metallic filament-based organic memory devices. J. Phys. Chem. C **2012,** 116 (33), 17955-17959.

53. Rabalais, J. W., *et al*., Trapped electrons in substoichiometric MoO_3 observed by X-ray electron spectroscopy. Chem. Phys. Lett. **1974,** 29 (1), 131-133.

54. Menzel, S., *et al*., Physics of the switching kinetics in resistive memories. Adv. Funct. Mater. **2015,** 25 (40), 6306-6325.

Chapter 5 : DUAL GAS SENSING CHARACTERISTICS OF NON-STOICHIOMETRIC 2D α-MoO_3

Environmental pollution due to the emission of various toxic and greenhouse gases is an emerging threat to the environment and ecosystem. Detecting traces of such gases in the atmosphere is essential for both human health and environmental safety, as they have a severe effect on the nervous system even at significantly low concentrations. In this work, non-stoichiometric 2D MoO_3 has been employed to develop gas sensors. The non-stoichiometric layer of MoO_3 has been synthesised on mica via the CVD technique. An easy and reliable transfer technique has been adopted to transfer the material onto any arbitrary substrates. The extensive characterisation of the transferred crystals has been carried out to establish the viability of the transfer process.

5.1 Introduction

The isolation of the graphene monolayers by mechanical exfoliation of bulk graphite opened the field of 2D materials that offers a unique combination of excellent mechanical and electronic properties.[1] However, the absence of intrinsic bandgap in graphene, expanded the exploration of other 2D materials, such as molybdenum dichalcogenides and oxides, Boron–nitride (h-BN), phosphorene.[2] The absence of interlayer interaction due to the electron confinement in single/two atomic layer enables the enhanced electrical properties compared to their bulk counterparts.[3] As such, 2D materials have been employed in a large number of

electronic and opto-electronic applications.[4-8] In addition to that, 2D structure provides large lateral size and ultrathin structure, which endow them an ultrahigh surface area with an extremely large proportion of surface atoms.[9] These surface atoms serve as active sites to effectively react with gas molecules. Hence, the distinctive structural features and outstanding electronic properties of 2D materials are favourable in the field of gas sensing applications.[10]

Environmental pollution due to emission of various toxic and greenhouse gases is an emerging threat to the natural balance. Among them, NO_2 (produced in combustion chemical plants and automobiles) and H_2S (produced in sewage plants, coal-mines, oil and natural gas industries) are two highly toxic and health hazard gases that make up a significant proportion.[11-12] Detecting traces of such gases in the atmosphere is essential for both human health and environmental safety, as even at very low concentrations they cause severe effect on the nervous system. The threshold limit for health safety standards of NO_2 and H_2S are <3 ppm and <10 ppm respectively.[11, 13-16]

Metal oxides are commonly used as gas sensing material due to their low cost and chemical stability at elevated temperature.[17-19] MoO_3 is one of the metal oxides that show excellent electrochromic and gasochromic properties.[20-23] Thermodynamically stable orthorhombic α-MoO_3 is a wide bandgap and high dielectric (*k*) material, which can be resolved into 2D layers. The high dielectric value of MoO_3 in combination with the 2D nature provides enhanced carrier mobility by reducing the Coulomb scattering.[5] Furthermore, the bandgap of the material can be easily tuned by introducing oxygen vacancies in the lattice, thereby creating gap states.[10] Combining all these properties of MoO_3, large surface area-to-volume

ratio in 2D form have the potential to provide higher sensitivity and lower power consumption for gas sensing applications.

In this work, the CVD has been utilised to grow large area 2D MoO_3 on mica. A facile transfer technique has been demonstrated, where the as-grown material was transferred onto SiO_2 via PDMS stamping process. Extensive characterisation of transferred MoO_3 crystals has been carried out, in order to establish the retention of the material's compositional integrity through the transfer process. These transferred crystals have been utilised to develop 2D conductometric gas sensors. The performance of the sensors toward H_2S and NO_2 has thoroughly evaluated.

5.2 Experimental Section

5.2.1 Chemical Vapour Deposition of non-stoichiometric α-MoO_3

Crystals of non-stoichiometric α-MoO_3 (MoO_{3-x}) were deposited on mica using CVD at 530 °C. MoO_3 powder (5 mg) used as a precursor, was placed in the middle zone (785 °C) of a horizontal 3-zone tube furnace. The growth substrates were placed downstream in the third zone, at 530 °C. 100 sccm Argon used as the carrier gas and the chamber pressure was maintained at ~300 mT throughout the whole deposition process. The furnace temperature was ramped up to the set temperatures in 60 minutes. The set temperatures maintained for 10 minutes for the reaction to occur. Thereafter, the furnace was allowed to cool down naturally.

5.2.2 Transfer process

The as grown MoO_{3-x} was transferred from mica to SiO_2 substrate via PDMS and

deterministic transfer method.[24] PDMS was spun on the MoO_{3-x}/mica growth surface at 300 rpm and cured at 120 °C. The PDMS/MoO_{3-x}/mica layers are dipped in to DI water at room temperature to allow the water penetrate between the MoO_{3-x}/mica layers. The PDMS/MoO_{3-x}/mica layer is taken out of the water bath after few minutes and the PDMS/MoO_{3-x} was peeled off from mica and blow-dried with N_2 gas. The delaminated MoO_3 crystals from mica were transferred subsequently on to SiO_2 substrate using the attached PDMS stamp. A detail schematic of the transfer process has been presented in Appendix C.

5.2.3 Material characterisation

The thickness of the transferred MoO_3 crystals was measured using Dimension Icon Bruker atomic force microscope under ScanAsyst Air mode. X-ray diffractogram were collected using a Bruker D4 Endeavor XRD instrument with monochromatic Cu *K*α as radiation source, within an angular range 2θ from 20° to 60°. LabRam HR Evolution Raman Spectrometer (laser excitation of 532 nm with a 50× objective) was utilised to assess the composition of the as-grown MoO_3. X-ray photoelectron spectroscopy (XPS) was performed using a Thermo Scientific K-alpha X-ray Photoelectron Spectrometer with an Al *K*α radiation source with energy of 1485 eV. Adventitious carbon peak at 284.8 eV was used as the calibration reference for fitting of the core level spectra of the principal elements. A high resolution transmission electron microscope (JEOL 2100F TEM/STEM (2011) operating with 200 kV acceleration voltage) was utilized for high-resolution transmission electron microscopy (HR-TEM) imaging.

5.2.4 Gas sensor fabrication and performance characterisation

Device fabrication was carried out on the transferred crystals on SiO_2/Si substrates by adopting standard photolithography. Electrodes (Au 90 nm with Cr 10 nm to promote adhesion) were deposited using electron beam deposition.

Gas sensing performance of the fabricated sensors was measured using Keithley 2001 Series multimeter and LabView software. A LINKAM (Scientific Instruments, United Kingdom) gas chamber with heating capability (of up to 600 °C) was used to conduct the gas sensing measurements. A multichannel mass flow controller (MKS 1479A, U.S.A.) was programmed to regulate gas input at a constant flow rate of 200 sccm. A schematic diagram of the gas sensing system is presented in Figure 5.1. Test gases were mixed with synthetic air to achieve the desired concentration. Various concentrations of NO_2 gas (0.5, 1, 5, 10 ppm) and H_2S gas (5, 10, 25, 50 ppm) at different operating temperatures (160 °C to 270 °C) were investigated for determining the optimal response. Additionally to establish the selectivity of the gas, H_2 (10,000 ppm), CO (1200 ppm), CO_2 (1000 ppm) and CH_4 (10000 ppm) also tested.

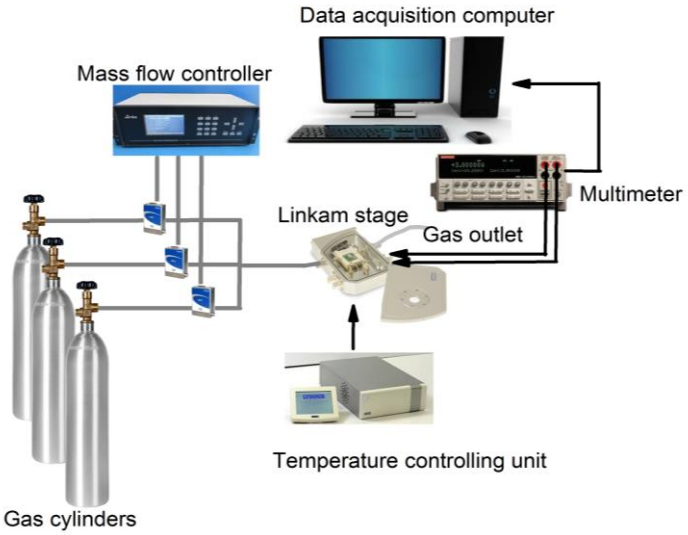

Figure 5.1 Schematic view of multi-channel gas sensing measurement system

5.3 Results and Discussion

Figure 5.2a shows the optical image of as-grown α-MoO_{3-x} on mica substrate. Here, mica was chosen as a growth substrate, as it provides a dangling-bond-free chemically inert surface that enables layered growth of α-MoO_{3-x}.[25-27] Layered α-MoO_{3-x} sheets mostly cover the whole area of the substrate. AFM was utilised to measure the thicknesses of the as-grown material on the edge of the coverage. The cross sectional profile reveals that the thickness of the as-grown material to be ~11 nm (Figure 5.2b). The optical image of the transferred material on to SiO_2/Si is presented in Figure 5.2c. The thickness profile of the transferred material shows ~8 nm of thickness on SiO_2 (Figure 5.2d).

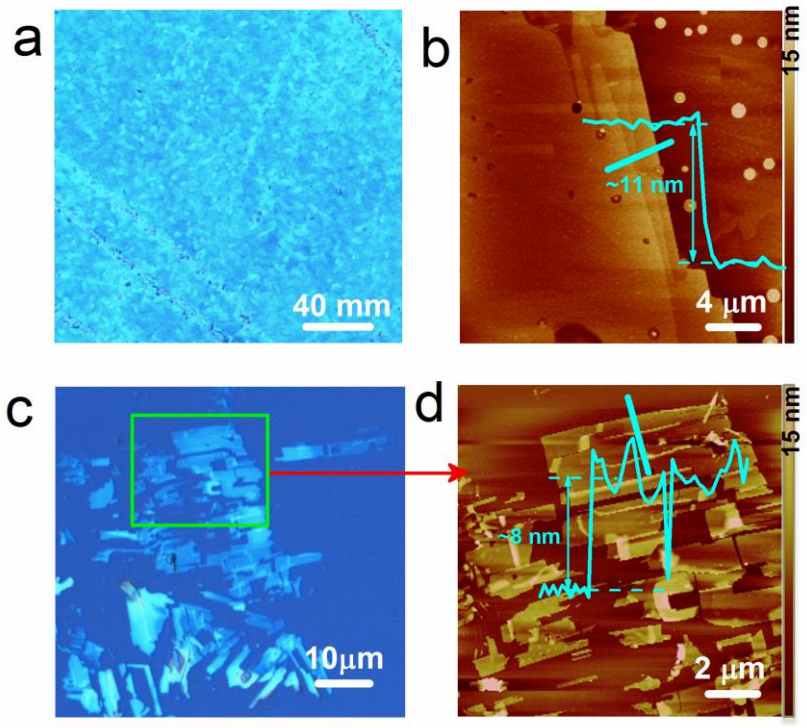

Figure 5.2 (a) Optical image and (b) AFM thickness profile of as-grown MoO_3 on mica. (c) Optical image and (d) AFM thickness profile of transferred MoO_3 on SiO_2.

In order to avoid contamination/degradation in crystal quality a simple and reliable transfer technique is essential. The viscoelastic property of PDMS is utilised to transfer the as-grown material from mica to other arbitrary substrates.[28] Liquid PDMS was spun on MoO_{3-x}/mica layers and cured at 120 °C. Subsequently, the PDMS/MoO_{3-x}/mica stack was submerged in DI water. Due to the hydrophilic nature of mica, water wedging occurs at the mica MoO_{3-x} interface, producing a MoO_{3-x}/PDMS stamp.[28] Consequently MoO_{3-x}/PDMS layer separates and releases from mica substrate. In order to transfer MoO_{3-x} on to the other target surface, the MoO_{3-x}/PDMS stamp is pressed against the surface of SiO_2 for deterministic transfer and peeled off slowly. By peeling off the PDMS stamp from the surface, MoO_{3-x} crystals get exfoliated and adhered preferentially on the target SiO_2 substrate.

Preserving the material composition and crystalline structure of the as-grown material are important to evaluate the transfer process. As such a detail characterisation was performed on as-grown and post-transferred material. XRD was utilised to characterise the crystalline nature of the as- grown and post-transferred material (Figure 5.3a). The diffraction peaks can be indexed as (040) at 25.6° and (060) at 38.9° of the orthorhombic α-MoO_3 crystal (JCPDS No 05–0508), which suggests the layered growth of the material perpendicular to the substrate. The sharpness of (020) and (040) peaks suggests highly ordered and preferentially crystalline nature of the as-grown material. The diffraction peaks of (040) and (060) planes of of post-transferred material are identical to α-MoO_3. As such, XRD results prove that the crystalline nature of the material retains unaltered post-transfer.

Raman spectroscopy was utilised to characterise the compositional integrity of the as-grown and post-transferred material. Full range Raman spectra (Figure 5.3b) show all the characteristics vibrational peaks of α-MoO_3 at 115, 157, 284, 336, 820 and 996 cm^{-1} on both as-grown and post-transferred material.[29-30] The strong in-plane vibration peak of 820 cm^{-1} and comparatively weak out-of-plane vibration of 996 cm^{-1} refers to the layered growth of the material in 010 directions. In addition, sharp and prominent nature of the Raman peaks suggests that the corresponding vibrational modes are from highly ordered structure of the material. Additional less intense peaks at 221 and 663 cm^{-1} on both as-grown and post-transferred material are observed, which correspond to non-stoichiometric MoO_3.[27, 28] As such, the Raman analysis suggests the presence of an intermediate oxidation state indicative of localized Mo^{5+}, produced due to oxygen vacancies. The Raman peaks on the post-transferred material appearing identical to the as-grown material confirms the preservation of compositional integrity and consistency of the material.

To further analyse the stoichiometry of the material, high-resolution XPS measurements were carried out on as-grown and post-transferred material (Figure 5.3c). The de-convoluted XPS peaks show two sets of doublets of Mo $3d_{5/2}$ and Mo $3d_{3/2}$. Binding energy of Mo $3d_{5/2}$ and Mo $3d_{3/2}$ levels are observed at 232.9 eV and 236.09eV respectively, which confirms Mo^{6+} oxidation state related to MoO_3.[31-33] Further examination of the XPS peaks reveals the presence of a second doublet at 231.8 eV and 234.8 eV for Mo $3d_{5/2}$ and Mo $3d_{3/2}$ confirming the existence of Mo^{5+} ions indicating the non-stoichiometric nature of the material.[34] As such, the above-mentioned characterisation results confirm that the as-grown material is non-stoichiometric (MoO_{3-x}) and that the transfer process does not affect the composition/structure of the material.

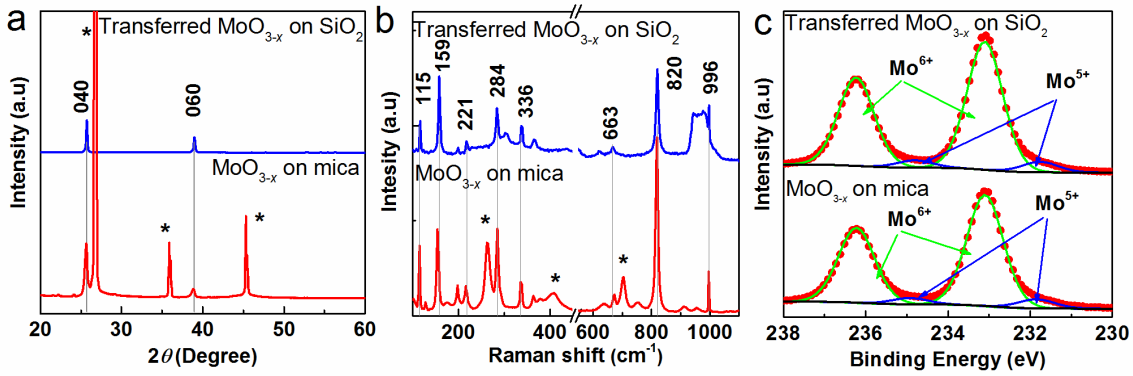

Figure 5.3(a) Raman spectra (b) XRD diffractogram and (c) XPS spectra of as grown MoO_3 on mica substrate and transferred MoO_3 on SiO_2/Si substrate. * denoted the mica peaks in a and b.

In order to gain further insight into the atomic structure of the as-deposited MoO_{3-x}, high resolution transmission electron microscopy (HRTEM) was utilized. CVD grown MoO_{3-x} was transferred onto a Carbon TEM grid using the previously described transfer procedure. During TEM imaging, ultrathin nano-sheets of MoO_{3-x} crystals are found (Figure 5.4). The HRTEM image shows that the grown material is highly crystalline. The crystal lattice spacing of 0.18 nm (Figure5.4 inset) represents the (002) plane of α-MoO_{3-x}.[25, 34, 35] The corresponding selected area electron diffraction (SAED) pattern shows clearly distinguishable diffraction spots (Figure5.4 inset) representing the (200) and (002) planes of orthorhombic α-MoO_{3-x}.[36, 37] As such, the TEM and XRD analyses collectively indicate the crystaline growth of the as synthesised material.

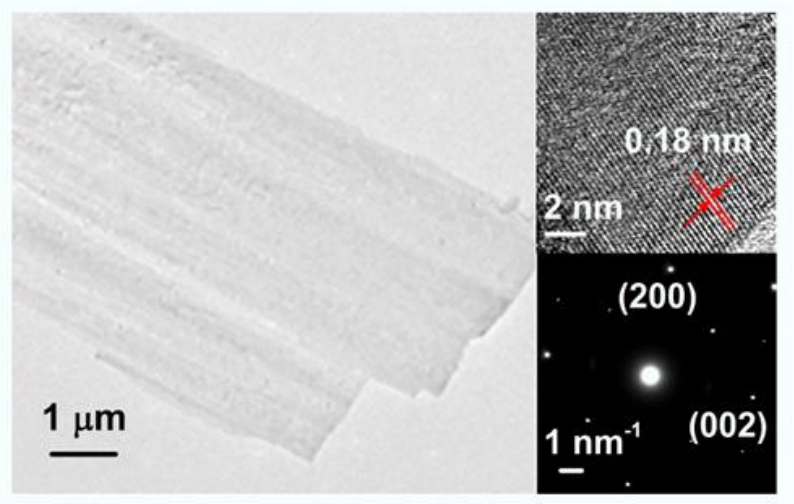

Figure 5.4 TEM image of CVD grown MoO_{3-x}. Inset showing HRTEM image and corresponding SAED pattern of as grown MoO_{3-x} crystals.

Gas sensing performance of the material was assessed, by developing conductometric gas sensors based on transferred MoO_{3-x}. The sensitivity, S has been calculated using the following formula,

$$S = \frac{R_a - R_g}{R_a} \times 100 \qquad (1)$$

where, R_a is the resistance in air and R_g is the resistance upon exposure to the target gas. It was observed that there is no response towards both NO_2 and H_2S below 160 °C, as the adsorbed oxygen on the surface does not have sufficient energy to react with the exposed gas molecules. As the temperature is increased beyond 160 °C, the conductivity of the metal oxide started to vary with the gas exposure. The response of the oxide layer towards NO_2 and H_2S was recorded at a range of working temperatures from 160 °C to 270 °C. The optimum temperature for sensing was determined from the sensitivity *vs*. Temperature relation (Figure 5.5a). It shows that the sensitivity of the material towards both gases started to

increase with temperature until 250 °C beyond which point, it was observed to saturate. Hence, 250 °C has been taken as the optimum working temperature for sensing performance.

In order to quantify the sensor characteristics, the sensitivity of the device towards varying concentrations of the targeted gas (NO_2 and H_2S) has been measured (Appendix C). Based on the results the sensitivity as a function of target gas concentration is presented in Figure 5.5b (NO_2 from 0.5 ppm to 10 ppm and H_2S from 1 pm to 50 ppm). It is evident that the *S* is directly proportional to the gas concentration in both cases, while the ΔS is significantly different for the two gases. This aspect allows us to reliably differentiate and identify the response between the two gases.

Selectivity of the material was studied, using both oxidizing and reducing gases such as, NO_2 (10 ppm), H_2S (10 ppm), H_2 (10,000 ppm) and CO (1200 ppm) CO_2 (1000 ppm) and CH_4 (10000 ppm) (Figure 5.5c). A negligible response to H_2 (10,000 ppm),CO (1200 ppm) CO_2 (1000 ppm) and CH_4 (10000 ppm) gases were observed, while a response of 56% and 18% observed when subjected to NO_2 (10 ppm) and H_2S (10 ppm) respectively. Upon exposure to NO_2 gas the resistance of the material increases and vice versa, the resistance decreases when exposed to H_2S. Thus, it demonstrates that the sensors based on 2D MoO_{3-x} exhibits selectivity towards both NO_2 and H_2S gases. These results indicate that the devices only respond towards NO_2 and H_2S. Being an oxidizing gas NO_2 has tendency to accept electrons from the oxide surface, which in return increases the resistance of the metal oxide. On the contrary, reducing gas such as H_2S donates electrons when interacting with metal oxide surface, and the conductivity of the oxide increases.

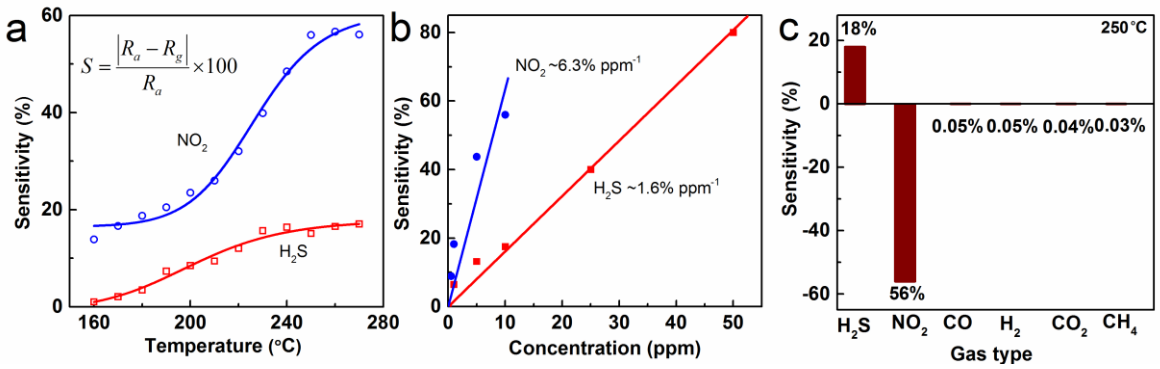

Figure 5.5(a) Sensitivity of the MoO_{3-x} based sensor upon 300 s of exposure to NO_2 (10 ppm) and H_2S (10 ppm) gases as a function of temperature. (b) Response sensitivity of the sensor towards different concentrations of NO_2 (10 ppm, 5 ppm, 1 ppm and 0.5 ppm) and H_2S (50 ppm, 25 ppm, 10 ppm, 5 ppm and 1 ppm) gases at 250 ^{0}C. (c) Selectivity of the sensors towards different gases upon 300 s of exposure (H_2S (10 ppm), NO_2 (10 ppm), CO (1200 ppm), H_2 (1000 ppm), CO (1000 ppm) and CH_4 (10,000 ppm)).

Response and recovery rate has been determined from response–recovery curve of NO_2 and H_2S gas (Figure 5.6a and b). Calculated response and recovery rate at 300 s are ~295.0 kΩ/s and ~276.0 kΩ/s for NO_2 gas, while ~28.5 kΩ/s and 48.0 kΩ/s for H_2S gas respectively. As such, the sensor shows significant difference in sensing properties towards NO_2 and H_2S gases. Response and recovery data were obtained at optimum temperature using the highest concentration of H_2S (50 ppm) gas (Appendix C).

To investigate the cyclic stability of the sensors, they were exposed to repetitive cycles of the target and recovery gases at 250 °C (Figure 5.6c and d). The change in resistance (ΔR) was measured for 10 repetitive cycles, where an average ΔR ~112 ± 1.64 MΩ and 19.5 ± 1.13 MΩ were observed for NO_2 and H_2S respectively. Such a small standard deviation in ΔR indicates the excellent cyclic endurance of the devices towards the targeted gases. A table is presented in Appendix C to refer the repeatabilty of the working devices.

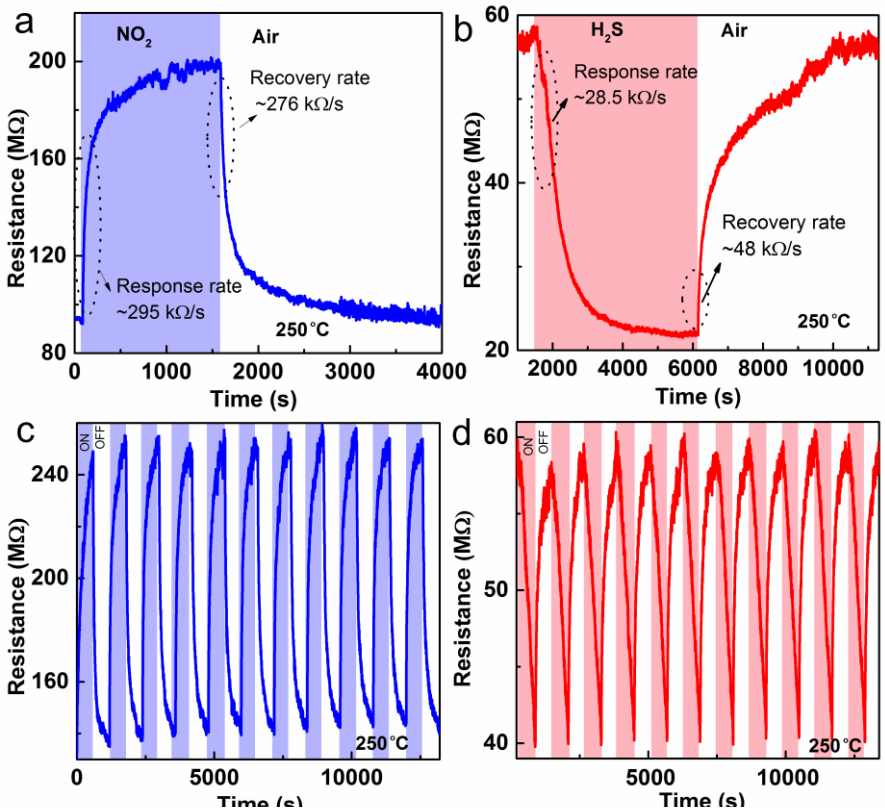

Figure 5.6 Response/recovery curves of the MoO_{3-x} sensor towards (a) NO_2 (10 ppm) and (b) H_2S (10 ppm) gases at 250 ^{0} C. Cyclic repeatability of the MoO_{3-x} based sensor towards (c) NO_2 (10 ppm) and (d) H_2S (10 ppm) showing repetitive cycles of response and recovery, at 250 ^{0} C.

It is known that the sensing mechanism in semiconducting oxides is influenced by the chemisorbed oxide ions that modulate the carrier concentration on the surface of the material.[35] The exposed gas causes a change in the oxygen balance of the oxide layer, resulting in an increase/decrease of charge carriers, leading to a variation in its resistance. However, the gas sensing reaction of MoO_3 does not involve the general mechanism operating in other semiconducting oxide sensors. Several reports show that MoO_3 does not chemisorb oxygen due to its crystalline-layered structure, rather it forms shear structure by removing lattice oxygen at the surface.[33, 36-37] The presence of oxygen vacancies in MoO_{3-x} material (refer to XPS and Raman analysis above), which works as adsorbing center with

high affinity to gases at high temperature. The oxygen molecules from environment will adsorb spontaneously on the surface vacancy sites and such oxygen species trap free electrons near the surface area can be written as follows:[38]

$$O_{2(g)} \leftrightarrow O_{2(ad)} \quad (2)$$

$$O_{2(ad)} + e^- \rightarrow O^-_{2(ad)} \quad (3)$$

At lower temperatures, these vacancies are not reactive, which results in high resistance of the conduction channel. Higher operating temperature provides abundant thermal energy to overcome the activation energy barrier to accomplish surface reaction, resulting in increasing free charge carrier density near the conduction band.[39] As such, the sensitivity increases with temperature and reaches a saturation point, where it is limited by the number of surface vacancy sites.

NO_2 sensing and recovering mechanism can be expressed as follows:

$$NO_2 + Mo^{5+} + O^-_{2(ad)} \rightarrow Mo^{6+} + NO^-_2 \quad (4)$$

$$Mo^{6+} + NO^-_2 + O^-_{2(ad)} \rightarrow Mo^{5+} + 2NO + O_2 \quad (5)$$

Upon exposure to NO_2 gas, oxygen species of MoO_{3-x} interact with NO_2 gas molecules and are being captured from conduction band of the sensing material. This results in an electron depleted charge region at the surface of the material, which results into an increase in resistance of the sensor material.[41] Subsequently when the sensor material comes in contact

with air, the ionised oxygen molecules trapped in to the vacancy sites and hence decrease the resistance of the sensor.

H_2S sensing reactions can be written as follows[42]

$$H_2S + O^-_{2(ad)} + Mo^{5+} \rightarrow Mo^{4+} + SO_2 + H_2O \qquad (6)$$

Upon exposure to H_2S gas, these oxygen species interact with H_2S gas molecules and releases charge carriers to the conduction band of the material, which reduces the surface depletion layer.[43] As such, the resistance of the sensor decreases, which shows the *n*-type behaviour of MoO_{3-x} towards a reducing gas. Subsequently, with the presence of oxygen these oxygen vacancies of MoO_{3-x} are being replenished by re-oxidation of the oxide surface with gaseous oxygen. [44]

$$Vo^{2+} + \frac{1}{2}O_2 + 2e^{-1} \leftrightarrow O_{o(s)} \qquad (7)$$

As discussed above, the α-MoO_{3-x} based sensors respond upon exposure to both NO_2 and H_2S gases. Consequently, to distinguish the response of the device in the presence of both of these target gases, membrane coatings can be used as filters to permit the passage of selected gases near the surface of the sensors.[45, 46] Furthermore, artificial neural networking systems can be utilized, which can efficiently differentiate the two types of gas response, when both of these gases are present.[47, 48] However, this aspect of the sensor development requires further research, which is beyond the limited scope of the current work.

5.4 Conclusions

In conclusion, gas-sensing performances have been demonstrated on 2D MoO_{3-x} after being transferred on to SiO_2/Si substrates. The transfer process enables the development of gas sensors on any arbitrary substrates. Extensive characterisation has been performed to confirm the compositional integrity after being transferred. The transferred material showed excellent selectivity and sensitivity to H_2S and NO_2. Minimum detectable limit of H_2S and NO_2 were observed to be 1 ppm and 0.5 ppm respectively. The calculated response and recovery rate are NO_2 ~295 kΩ/s and ~276 kΩ/s towards NO_2, while ~28.5 kΩ/s and 48 kΩ/s towards H_2S gas respectively. In addition to that, the sensor material shows stable cyclic repeatability with negligible variation in ΔR for several cycles. These results suggest that the sensors based on 2D MoO_{3-x} crystals provide opportunities to create high performance 2D sensing systems in future.

5.5 References

1. Novoselov, K. S., *et al*., Electric field effect in atomically thin carbon films. Science **2004,** 306 (5696), 666.

2. Novoselov, K. S., *et al*., Two-dimensional gas of massless Dirac fermions in graphene. Nature **2005,** 438, 197.

3. Radisavljevic, B., *et al*., Single-layer MoS_2 transistors. Nat. Nanotechnol. **2011,** 6, 147.

4. Cheng, R., *et al*., Few-layer molybdenum disulfide transistors and circuits for high-speed flexible electronics. Nat. Commun. **2014,** 5, 5143.

5. Balendhran, S., *et al*., Enhanced charge carrier mobility in two-dimensional high dielectric molybdenum oxide. Adv. Mater. **2013,** 25 (1), 109-14.

6. Feng, W., *et al*., Synthesis, properties and applications of 2D non-graphene materials. Nanotechnology **2015,** 26 (29), 292001.

7. Bhimanapati, G. R., *et al*., Recent advances in two-dimensional materials beyond Graphene. ACS Nano **2015,** 9 (12), 11509-11539.

8. Rahman, F., *et al*., Two-dimensional MoO_3 via a top-down chemical thinning route. 2D Mater. **2017,** 4 (3), 035008.

9. Yang, S., *et al*., Gas sensing in 2D materials. Appl. Phys. Rev. **2017,** 4 (2), 021304.

10. Neri, G., Thin 2D: The new dimensionality in gas sensing. Chemosensors **2017,** 5 (3), 1-21.

11. Afzal, A., *et al*., NO_x sensors based on semiconducting metal oxide nanostructures: Progress and perspectives. Sens. Actuators, B **2012,** 171-172, 25-42.

12. Chen, Y. J., *et al*., Porous iron molybdate nanorods: in situ diffusion synthesis and low-temperature H_2S gas sensing. ACS Appl. Mater. Interfaces **2013,** 5 (8), 3267-74.

13. Yu, L., *et al*., Both oxygen vacancies defects and porosity facilitated NO_2 gas sensing response in 2D ZnO nanowalls at room temperature. J. Alloys Compd. **2016,** 682, 352-356.

14. Sun, G.-J., *et al*., Bi-functional mechanism of H_2S detection using CuO–SnO_2 nanowires. J. Mater. Chem. C **2013,** 1 (35), 5454-5462.

15. Gao, X., *et al*., Synthesis and H_2S sensing performance of $MoO_3/Fe_2(MoO_4)_3$ yolk/shell nanostructures. RSC Adv. **2015,** 5 (47), 37703-37709.

16. Hosseini, Z. S., *et al*., Room temperature H_2S gas sensor based on rather aligned ZnO nanorods with flower-like structures. Sens. Actuators, B **2015,** 207, 865-871.

17. Gutruf, P., *et al*., Stretchable and tunable microtectonic ZnO-based sensors and photonics. Small **2015,** 11 (35), 4532-9.

18. Zhang, H., *et al*., SnO_2 nanoparticles-reduced graphene oxide nanocomposites for NO_2 sensing at low operating temperature. Sens. Actuators, B **2014,** 190, 472-478.

19. Liu, S., *et al*., High performance room temperature NO_2 sensors based on reduced graphene oxide-multiwalled carbon nanotubes-tin oxide nanoparticles hybrids. Sens. Actuators, B **2015,** 211, 318-324.

20. Andres, C.-G., *et al*., Deterministic transfer of two-dimensional materials by all-dry viscoelastic stamping. 2D Mater. **2014,** 1 (1), 011002.

21. Cui, F., *et al*., Tellurium-assisted epitaxial growth of large-area, highly crystalline ReS_2 atomic layers on mica substrate. Adv. Mater. **2016,** 28 (25), 5019-24.

22. Qin, J.-K., *et al*., van der Waals epitaxy of large-area continuous ReS_2 films on mica substrate. RSC Adv. **2017,** 7 (39), 24188-24194.

23. Wang, Q., *et al*., van der Waals epitaxial ultrathin two-dimensional nonlayered semiconductor for highly efficient flexible optoelectronic devices. Nano Lett. **2015,** 15 (2), 1183-9.

24. Molina-Mendoza, A. J., *et al.*, Centimeter-scale synthesis of ultrathin layered MoO_3 by van der Waals epitaxy. Chem. Mater. **2016,** 28 (11), 4042-4051.

25. Kalantar-zadeh, K., *et al*., Synthesis of nanometre-thick MoO_3 sheets. Nanoscale **2010,** 2 (3), 429-33.

26. Siciliano, T., *et al*., Characteristics of molybdenum trioxide nanobelts prepared by thermal evaporation technique. Mater. Chem. Phys. **2009,** 114 (2-3), 687-691.

27. Lu, X., *et al*., Preparation of quantum dots from MoO_3 nanosheets by UV irradiation and insight into morphology changes. J. Mater. Chem. C **2016,** 4 (48), 11449-11456.

28. Camacho-López, M. A., *et al*., Micro-Raman study of the m-MoO_2 to α-MoO_3 transformation induced by cw-laser irradiation. Opt. Mater. **2011,** 33 (3), 480-484.

29. Xie, F., *et al*., Low-temperature solution-processed hydrogen molybdenum and vanadium bronzes for an efficient hole-transport layer in organic electronics. Adv. Mater. **2013,** 25 (14), 2051-2055.

30. Alsaif, M. M., *et al*., Exfoliation solvent dependent plasmon resonances in two-dimensional sub-stoichiometric molybdenum oxide nanoflakes. ACS Appl. Mater. Interfaces **2016,** 8 (5), 3482-93.

31. Sunu, S. S., *et al*., Electrical conductivity and gas sensing properties of MoO_3 Sens. Actuators, B **2004,** 101 (1-2), 161-174.

32. Wang, C., *et al*., Role of molybdenum oxide for organic electronics: Surface analytical studies. J. Vac. Sci. Technol. B **2014,** 32 (4), 040801.

33. Kim, H.-S., *et al*., Oxygen vacancies enhance pseudocapacitive charge storage properties of MoO_{3-x}. Nat. Mater. **2016,** 16, 454.

34. Bai, H., *et al*., Direct growth of defect-rich MoO_{3-x} ultrathin nanobelts for efficiently catalyzed conversion of isopropyl alcohol to propylene under visible light. J. Mater. Chem. A **2016,** 4 (5), 1566-1571.

35. Rahman, F., *et al*., Reversible resistive switching behaviour in CVD grown, large area MoO_x. Nanoscale **2018,** 10 (42), 19711-19719.

36. Alsaif, M. M. Y. A., *et al*., Tunable plasmon resonances in two-dimensional molybdenum oxide nanoflakes. Adv. Mater. **2014,** 26 (23), 3931-3937.

37. Alsaif, M. M. Y. A., *et al*., High-performance field effect transistors using electronic inks of 2D molybdenum oxide nanoflakes. Adv. Funct. Mater. **2016,** 26 (1), 91-100.

38. Barazzouk, S., *et al*., MoO_3-based sensor for NO, NO_2 and CH_4 detection. Sens. Actuators, B **2006,** 119 (2), 691-694.

39. Yang, S., *et al*., Highly responsive room-temperature hydrogen sensing of alpha-MoO_3 nanoribbon membranes. ACS Appl. Mater. Interfaces **2015,** 7 (17), 9247-53.

40. Bai, S., *et al*., Ultrasonic synthesis of MoO_3 nanorods and their gas sensing properties. Sens. Actuators, B **2012,** 174, 51-58.

41. Rahmani, M. B., *et al*., Gas sensing properties of thermally evaporated lamellar MoO_3. Sens. Actuators, B **2010,** 145 (1), 13-19.

42. Prabakaran Shankar, J. B. B. R., Gas sensing mechanism of metal oxides: The role of ambient atmosphere, type of semiconductor and gases - A review. Sci. Lett. J. **2015,** 4, 126.

43. Zhang, L., *et al*., Self-assembly gridding α-MoO_3 nanobelts for highly toxic H_2S gas sensors. Sens. Actuators, B **2016,** 237, 350-357.

44. Illyaskutty, N., *et al*., Hydrogen and ethanol sensing properties of molybdenum oxide nanorods based thin films: Effect of electrode metallization and humid ambience. Sens. Actuators, B **2013,** 187, 611-621.

45. Pijolat, C., *et al*., Application of membranes and filtering films for gas sensors improvements. Thin Solid Films **2005,** 490 (1), 7-16.

46. Korotcenkov, G.; Cho, B. K., Engineering approaches for the improvement of conductometric gas sensor parameters: Part 1. Improvement of sensor sensitivity and selectivity (short survey). Sens. Actuators, B **2013,** 188, 709-728.

47. Aleixandre, M., *et al*., Analysis of neural networks and analysis of feature selection with genetic algorithm to discriminate among pollutant gas. Sens. Actuators, B: **2004,** 103 (1-2), 122-128.

48. Krivetskiy, V., *et al*., Selective detection of individual gases and CO/H_2 mixture at low concentrations in air by single semiconductor metal oxide sensors working in dynamic temperature mode. Sens. Actuators, B **2018,** 254, 502-513.

Chapter 6 : CONCLUSIONS AND FUTURE WORK

6.1 Conclusions

The research presented in this thesis was carried out to address the gaps in the current body of knowledge, as described in the previous chapters. This research work was carried out through three specific objectives: (a) an investigation to obtain 2D MoO_3 crystals in a controllable and reliable way using a new chemical etching route and to study the electronic properties of the etched crystals in FETs, (b) a study to understand the resistive switching behaviour of large area MoO_3 and assessing their applicability in memory technology and (c) an investigation of the gas-sensing performance of non-stoichiometric 2D α-MoO_3. The aforementioned objectives were completed throughout two published works in journal, and the third one is still under review.

6. 1. 1 Obtaining 2D MoO_3 crystals of desired thicknesses and utilising them as a high performance channel material in FETs

Existing synthesis techniques for obtaining 2D MoO_3 crystals do not produce crystals of a uniform desired thickness efficiently. As such, a novel and easy chemical etching route is developed to obtain crystals of desired thicknesses reliably and controllably. A statistical analysis was performed to study the reliability and repeatability of the etching technique. The post-etching material characterisation confirms the compositional and crystalline integrity of

the etched crystals by retaining the intrinsic properties of the material. Hence, a controllable and easily deployable chemical etching method is established to thin down bulk MoO_3 crystals in order to obtain them in 2D form and in pristine nature. Subsequently, the study of electronic properties of such 2D crystals in FETs, established the viability of this material in electronic applications.

6. 1. 2 Assessing resistive memory characteristics in large area CVD grown MoO_3 crystals

A large number of metal oxides with a high dielectric value have been investigated for resistive memory applications. However, a knowledge gap exists concerning memory behaviour in 2D metal oxides. As such, the reversible resistive memory behaviour in large area 2D MoO_3 was investigated and the switching mechanism of the material was studied. The resistive memory performances of the oxide layer show low power consumption and high cyclic endurance. A thorough material characterisation was performed, which reveals that the deposited material is a combination of multiple oxidation levels of MoO_3, which is partially oxygen deficient. The existing oxygen vacancies play a crucial role in resistive memory behaviour of the material. The data retention of 10^4 s and ~6,000 cyclic endurances establishes the viability of resistive memory applications of MoO_3 layers. Hence, the developed reversible resistive memory cells based on large-area MoO_3 pave a new path in planar memory technology.

6. 1. 3 Gas sensing characteristics of non-stoichiometric 2D α-MoO_3

The gas-sensing performance of non-stoichiometric 2D α-MoO_3 is investigated. Considering the thermal stability, enhanced carrier mobility and excellent electron affinity of MoO_3, a

conductometric gas-sensing system was developed. The experimental characterisation of such devices shows high selectivity towards toxic and health hazard gases, such as H_2S and NO_2. A thorough material characterisation was performed that confirms the material composition. The retention characteristics of the sensors reveal excellent repeatability with a negligible variation in sensitivity. The calculated response and recovery rate suggests that these novel 2D MoO_3-based sensors offer great opportunities for future high-performance gas-sensing devices.

6.2 Future work

The research work carried out in this thesis has yielded a significant amount of insights into the synthesis process of 2D MoO_3 and the characteristics of novel electronic devices based on the 2D MoO_3. Still, several aspects remain for further investigation. A few significant research topics are listed below:

- This research work presented the switching performance of FETs based on 2D MoO_3 crystals. The switching performance of such materials can be improved further through hetero-structuring with other 2D materials of distinct properties, such as a high-mobility charge injection layer and a high dielectric switching layer. There exist a large number of layered materials that can be exfoliated and incorporated into such stacks. The strong interlayer coupling between the films in such hetero-structured layers results in enhanced charge density and energy-band modulation. Future works could attempt to address the fabrication of FETs based on hetero-structured 2D MoO_3 with graphene/MoS_2 and to understand the switching capabilities of such devices.

- Low contact resistance is a prerequisite to realise high performance FETs. Thus, ionic liquids are used as gate electrodes in FETs as they provide high ionic conductivity and large specific capacitance, which results in enhanced carrier mobility and high on/off ratio. Future work could emphasise in addressing the viability of ionic liquid gated FETs based on 2D crystals of MoO_3.

- This research work presented the resistive memory behaviour in large-area MoO_3 crystals. Longer retention and low power consumption enables the viability of the material for integration into a larger scale memory array. Further reducing the thickness of the oxide layer would enhance the performance of such devices in terms of switching voltage, retention and endurance. Future work could highlight on the investigation of oxide layers' thickness dependent memory behaviour of such devices.

- The gas-sensing performance of non-stoichiometric 2D α-MoO_3 crystals is studied and presented in this research. The sensing performances show high selectivity towards H_2S and NO_2 gases with an excellent response and recovery rate. However, to improve the selectivity of the sensor additional passive and catalytically active filters can be incorporated directly into the sensor. Furthermore, artificial neural network based training can be utilized, to selectively differentiate the two types of gas responses. As such, future work could focus on the study of improvement of the selectivity of such devices.

- Humidity monitoring is important for industrial processing and environmental control. MoO_3 adsorbs water molecules to form hydroxyl molecule that helps to change the conductivity of the material. In 2D form, large surface area to volume provides a large number of reaction sites and thus high responsive humidity sensors can be realised.

Hence, future work could emphasise on the investigation of conductometric humidity sensors charaterisation based on 2D MoO_3 crystals.

Chapter 7 Appendices

Appendix A: Supporting information for Chapter 3

A1. Table showing the list of I_{DS} value corresponds to V_{DS} for multiple working devices.

Table A 1 The list of I_{DS} value corresponds to V_{DS} for multiple devices

Sample	I_{DS}**(nA)**	V_{DS}**(v)**	V_{GS}**(v)**
02072016_B03_01	370	0.3	1
02092016_B05_04	150	0.3	1
05122016_B19_02	430	0.3	1
05112017_B10_02	230	0.3	1
12022017_B11_01	190	0.3	1

Appendix B: Supporting information for Chapter 4

B1. CVD growth temperature comparison

Table B 1 A comparison of crystalline MoO_3 growth obtained via CVD, from various reports

Authors	**Growth temperature/°C**	**Pressure/mTorr**	**Phase of MoO_3**	**Reference**
Kalantar-zadeh et al.	400	Ambient	α-MoO_3	B1
Balendhran et al.	350-560	Ambient	α-MoO_3	B2
Kim et al.(Plasma Enhanced CVD)	150	100	α-MoO_3	B3
Our work	530	300	α-MoO_3 /MoO_2	

B2. Pulse width and Energy consumption

To assess the cyclic endurance of the devices, a pulse train of width 2 ms was applied. A read pulse of 500 mV was applied after each SET and RESET pulse to measure the resistance of the device during LRS and HRS. The associated energies for SET and RESET switching were computed to be 6.7 μJ to 18 nJ range during the pulse switching.

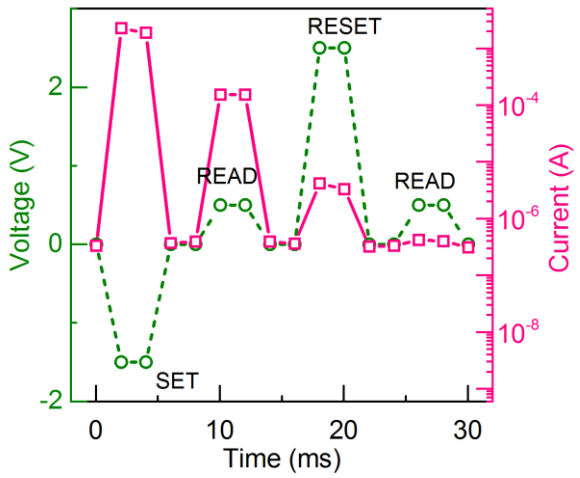

Figure B 1 A train pulse of width 2 ms was applied to measure the endurance of the device. Voltage vs. time and Current vs. time has been plotted to show the input and output curves.

B3. A quantitative performance comparison of various 2D materials

Table B 2 A Performance comparison of various 2D materials as resistive memory

Author	**Material**	**ON/OFF ratio**	**Retention duration/s**	**endurance**	**References**
Cheng et al.	MoS_2	10^3	---	1000	B4
Shin et al.	MoS_2	10^2	10^4	100	B5
Sangwan et al.	MoS_2	10^3	---	------	B6
Our work	MoO_x	10^3	10^4	~6000	

B4. Inverse FFT analysis of the cross-sectional TEM

In order to highlight the percentage of the crystalline area accurately, the TEM images of pristine and electroformed cells are sub-divided into smaller regions of interest (ROIs). Diffraction patterns corresponding to (001) plane of MoO_3 and (002) plane of MoO_2 are used to generate inverse fast Fourier transform (iFFT). The results are presented in Fig. A 2a and b, where the iFFT of pristine and electroformed cells are presented, respectively. The iFFT data is then analysed using ImageJ to determine the percentage crystalline area. The analysis indicates that the pristine film is composed of 72.50% of crystalline MoO_3 and MoO_2 while the remainder was observed to be amorphous in nature. After electroforming, 94.11% of the film was observed to be crystalline sub-stoichiometric MoO_3.

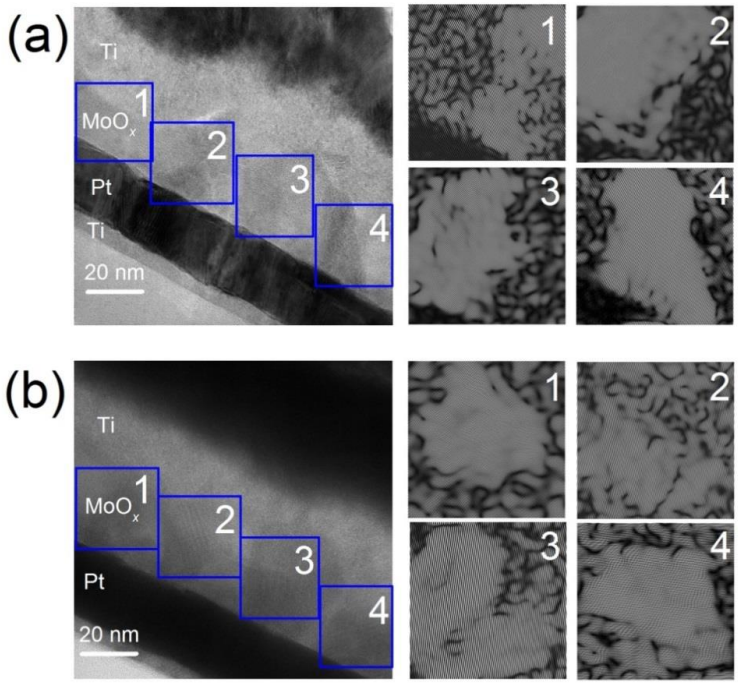

Figure B 2 HRTEM images of (a) a pristine cell and the corresponding iFFT of the ROIs numerically labelled from 1 to 4 and (b) an electroformed cell and the corresponding iFFT of the highlighted areas.

B5. Table including number of working devices with experimental data

Table B 3 The list of switching voltage, ON/OFF ratio and number of repetitive cycles are presented for multiple samples

Sample	SET Voltage (V)	RESET Voltage (V)	ON/OFF ratio	Repetitive cycles
010517_01	-1.16	2.45	1000	~100
020318_07	-1.52	2.50	1000	~500
030318_03	-2.10	1.84	100	~1500
040418_02	-1.80	2.76	1000	~2600
050518_05	-1.19	2.28	1000	~1000
060518_03	-2.80	1.38	1000	~6000

References

B1. K. Kalantar-zadeh *et al*., Synthesis of nanometre-thick MoO_3 sheets. Nanoscale, 2010, **2**, 429-433.

B2. S. Balendhran *et al*., Enhanced charge carrier mobility in two-dimensional high dielectric molybdenum oxide. Adv. Mater., 2013, **25**, 109-114.

B3. U. K. Hyeong *et al*. , Highly uniform wafer-scale synthesis of α-MoO_3 by plasma enhanced chemical vapor deposition. Nanotechnology, 2017, **28**, 175601.

B4. P. Cheng *et al*., Memristive Behavior and Ideal Memristor of 1T Phase MoS_2 Nanosheets. Nano Lett., 2016, **16**, 572-576.

B5. G. H. Shin *et al*., Multilevel resistive switching nonvolatile memory based on MoS_2 nanosheet-embedded graphene oxide. 2D Mater., 2016, **3**, 034002.

B6. V. K. Sangwan *et al*., Gate-tunable memristive phenomena mediated by grain boundaries in single-layer MoS_2. Nat. Nanotechnol., 2015, **10**, 403-406.

Appendix C: Supporting information for Chapter 5

C1. A detail schematic of the transfer process:

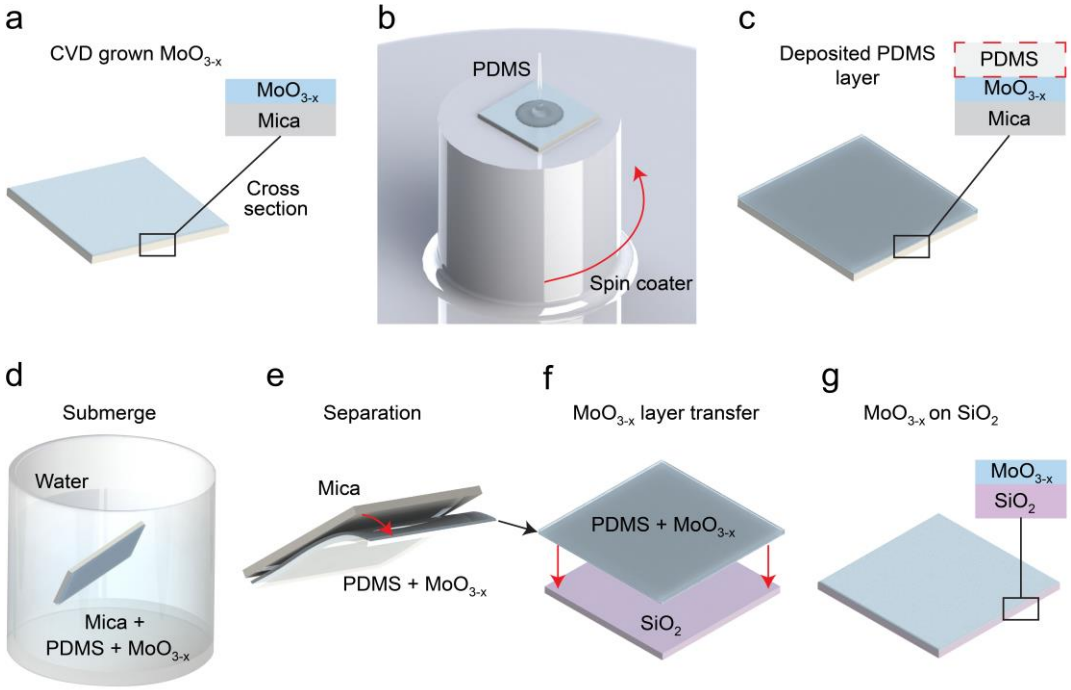

Figure C 1 Schematic drawing of the method used to transfer the as-grown MoO_{3-x} crystals from mica to SiO_2.

C2. Table showing various 2D materials for NO_2 and H_2S sensing

Table C 1 NO_2 and H_2S sensing performance reports on various 2D materials in comparison to our work

Structure	**Synthesis**	**Concentration/ ppm**	**Operating Temperature/ °C**	**% Sensitivity** $S = \frac{\lvert R_a - R_g \rvert}{R_a} \times 100\%$	**Reference**
2D MoS_2	CVD	10 ppm NO_2	100	16	C1
2D WS_2	ALD	25 ppm NO_2	RT	10	C2
2D SnS_2-rGO	Thermal reduction and wet chemical	11.9 ppm NO_2	80	56.8	C3
2D MoO_{3-x}	CVD	10 ppm NO_2	250	56	Our work
quasi-2D Cu_2O/SnO_2	Electrochemical	50 ppm H_2S	RT	45	C4
2D MoO_{3-x}	CVD	50 ppm H_2S	250	81	Our work

C3. Response performance of the sensor towards 50 ppm of H_2S gas:

The response of the oxide layer towards 50 ppm of H_2S was recorded at a range of working temperatures from 160 ^{0}C to 270 ^{0}C. The sensitivity vs. temperature relationship is presented in Figure C2a, shows the device sensitivity towards H_2S gas. The response and recovery rate for 10 repeatable cycles of H_2S gas have been calculated, which shows an average response rate of 223 ± 2.5 kΩ/s and recovery rate of 126 ± 1.7 kΩ/s towards 50 ppm of H_2S.The change in resistance (ΔR) was measured for 10 repetitive cycles, where an average ΔR 81 ± 2.29 MΩ was observed for H_2S gas.

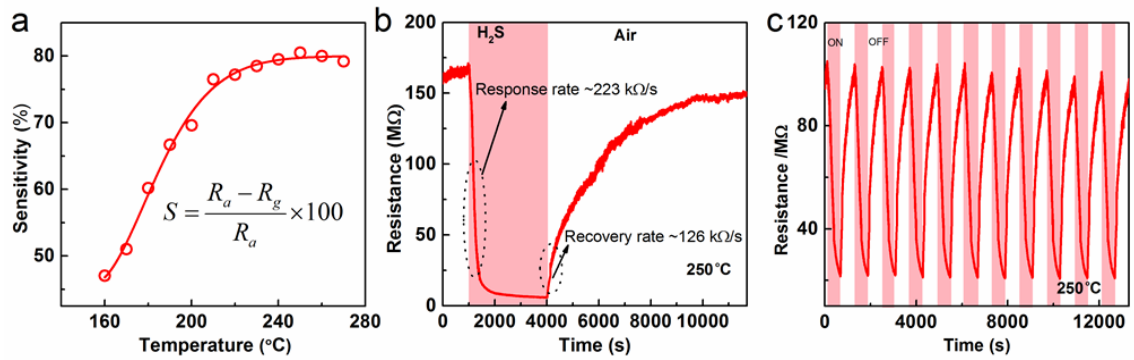

Figure C 2 Gas sensing performance of 50 ppm of H_2S gas. (a) Sensitivity as a function of temperature, (b) response and recovery curve and (c) the cyclic repeatability of the devices.

C4. Response and recovery at various concentrations of NO_2 and H_2S gases:

The gas sensing performance of the MoO_{3-x} sensor was assessed towards NO_2 and H_2S gases with concentrations ranging from 0.5 ppm to 10 ppm and 1 ppm to 50 ppm respectively, at the optimum temperature of 250 ^{0}C.

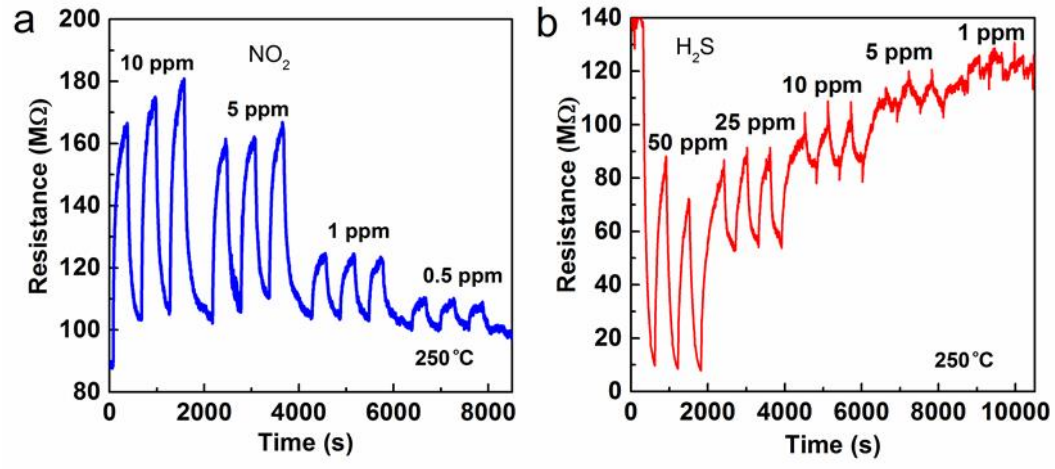

Figure C 3 Gas sensing response with different concentration of (a) NO_2 and (b) H_2S gas.

C5. Table includes multiple working devices response towards NO_2 and H_2S gases.

Table C 2 The list of response rate and recovery rate towards NO_2 and H_2S from multiple samples

Sample	NO_2 gas		H_2S gas	
	Response rate kΩ/s	Recovery rate kΩ/s	Response rate kΩ/s	Recovery rate kΩ/s
010618_02_05	296.00	280.00	36.67	56.67
020718_03_01	293.00	280.00	33.33	49.33
030818_04_02	285.00	273.00	26.67	50.00
041118_05_03	303.00	270.00	30.00	53.33
050119_02_01	297.00	267.00	23.33	50.00

References

C1. B. Cho *et al*., Charge-transfer-based gas sensing using atomic-layer MoS_2.. Sci. Rep., 2015, **5**, 8052.

C2. K. Y. Ko *et al*., Improvement of gas-sensing performance of large-area tungsten disulfide nanosheets by surface functionalization. ACS Nano, 2016, **10**, 9287-9296.

C3. M. Shafiei *et al*., Low-operating temperature NO_2 gas sensors based on hybrid two-dimensional SnS_2-reduced graphene oxide. Appl. Surf. Sci., 2018, **462**, 330-336.

C4. G. Cui *et al*., Resonant tunneling modulation in quasi-2D Cu_2O/SnO_2 p-n horizontal-multi-layer heterostructure for room temperature H_2S sensor application. Sci. Rep., 2013, **3**, 1250.